Université catholique de Louvain

Faculté des Sciences

A New Limit On $\nu_\mu \rightarrow \nu_\tau$ Oscillations

Dissertation présentée par

Gustaaf Brooijmans

en vue de l'obtention du grade de docteur en Sciences

Promoteur: **Professeur D. Favart**

1998

Contents

Chapter 1

Introduction

While confirmations of the validity of the Standard Model at low and high energies (reached by present accelerators) continue to be produced, the high-energy physics community is turning towards the search for physics beyond the Standard Model.

In chapter 2 we review the evidence for the existence of three neutrino flavors. We proceed by quickly summarizing their properties in the Standard Model and examine the present limits set by experiments on each neutrino's mass. We then move on to some theoretical considerations on neutrino masses, mainly based on cosmology and Grand Unified Theories and the chapter closes by illustrating the remarkable possibility of neutrino oscillations.

Interestingly, at the end of 1997 it is in the neutrino physics domain that most inconsistencies with the Standard Model are found. Not in experiments using neutrinos to study the weak and strong interactions, as we see at the start of chapter 3, but definitely when probing the solar and atmospheric neutrino fluxes. This is detailed later in that chapter, without forgetting the only neutrino oscillation appearance evidence found so far (LSND). From the results presented it seems to be clear that neutrinos have opened a window towards new physics. However, solving all the present problems (cosmology, solar, atmospheric, LSND) with our simple neutrino oscillation interpretation seems impossible or difficult and definitely not very elegant. So maybe this window we are opening is really much larger than we think and pushing more could yield some fascinating results. The existing constraints are definitely such that experiments should be built to search for appearance at specific oscillation parameter values.

When Chorus was designed and started datataking, these constraints were quite a bit weaker. However, the parameter space area which is being explored is still very relevant in the light of a model solving the Hot Dark Matter and solar problems while satisfying the very elegant see-saw mechanism.

We briefly describe the experiment in chapter 4, explaining the chosen tau neutrino detection strategy and the proposed sensitivity to $\nu_\mu \rightarrow \nu_\tau$ oscillations.

In chapter 5 we start by describing the trackers: purpose, geometry and readout. This is followed by an explanation of the event reconstruction algorithm and its efficiency. Our main contribution to the reconstruction in the Target Trackers consists in their alignment: after introducing a few concepts we give the details of the alignment procedure, the trackers' degrees of freedom and the accuracy obtained for each of these. Two more paragraphs say a few more words on the problem of separation of variables for minimization and the detector stability over time.

Next, in chapter 6, we discuss our work on the tagging of muons with the Chorus detector. After explaining the various algorithms used we come to the efficiencies, understanding the found results through event kinematics. A study of non-tagged muons shows that the software efficiency is very close to maximal, and physics is the cause of nearly all the losses.

The bulk of our study lies in the determination of the scanning efficiencies. Chapter 7 starts with the description of the interface emulsion sheets and the proof of a method we developed to extract the real scanning efficiency for these sheets from the data itself. We proceed to compare the found results with the results obtained by our simulation and comment on the possible causes for the observed discrepancy. Moving on, we explain how the search for the primary vertex and a possible decay kink is conducted and give the corresponding efficiencies we found using our Monte-Carlo. To close the chapter, we elaborate on the video image simulation, a tool we developed to help improve and determine the efficiency of video image analysis programs. These programs will be used intensively in the future to search for kinks.

Last but not least, chapter 8 combines all these numbers with the present scanning status to put a new limit on $\nu_\mu \rightarrow \nu_\tau$ oscillations. It also includes a few words on backgrounds and the results from a study of systematic uncertainties. We conclude with a new exclusion plot.

Chapter 2

Neutrinos and their (Potential) Properties

2.1 Existence of Neutrinos

In 1930 Wolfgang Pauli proposed the existence of a neutral particle that would hardly interact with matter to explain the continuous electron energy distribution observed in nuclear beta decay. This explanation "saved" energy and momentum conservation.

As early as 1932 Enrico Fermi provided a theoretical framework for beta decay which included the neutrino and was inspired by the structure of the electromagnetic interactions.

It wasn't until 1953 however that a first hint of experimental evidence for the existence of the elusive neutrino was published [Rei53]: F. Reines and C. L. Cowan, Jr. searched for inverse neutron beta decay

$$\nu + p \rightarrow e^+ + n \tag{2.1}$$

by exposing a proton rich target to the (expectedly) intense neutrino flux of a nuclear reactor (in this case at Hanford). Since the same detection technique is still used nowadays a brief description is worthwile:

The detector consisted in hydrogeneous liquid scintillator with some dissolved Cadmium. The reaction is detected by the delayed coincidence of pulse pairs: the first from the positron annihilation and the second from the neutron capture by a Cadmium nucleus (the typical neutron capture time was tuned to about $5\mu sec$). More precisely, the signal selection was based on the energies of the two pulses, their time-delay spectrum, the dependence of the rate on the reactor power and the comparison with the predicted rate (calculations based on beta-decay theory estimated the cross-section of reaction (2.1) to be $\approx 6\ 10^{-20}\ barn$ or $\approx 6\ 10^{-44}\ cm^2$ with an estimated error of about 25%). And although they suffered from a significant cosmic ray background, the increase in event rate when switching on the reactor seemed clear. They excluded reactor neutrons as the source of this increase after measuring their flux with nuclear emulsion plates.

However, the difference in counting rate due to the reactor was only 0.40 ± 0.21 delayed counts per minute, such that confirmatory work was needed to prove they had indeed observed the neutrino.

In 1956, after setting up a similar but more sophisticated experiment near one of the reactors of the Savannah River Plant, Cowan, Reines and coworkers confirmed their result.

They quote [Cow56] a measured cross-section for reaction (2.1) of 6.3 10^{-44} cm^2, in good agreement with the predicted value.

2.2 Three Generations of Light Neutrinos

2.2.1 Discovery of the Muon Neutrino

By the end of the fifties, measurements of positron,electron and neutrino polarization in beta-decays and muon decay seemed to indicate both of these reactions proceeded through a combination of vector and axial-vector couplings. This suggested these interactions could be one and the same. Unfortunately, by then the experimental upper limit on the branching ratio

$$B.R. = \frac{R(\mu \to e + \gamma)}{R(\mu \to e + \nu + \overline{\nu})} \tag{2.2}$$

was already 2 10^{-5} [Lok55], while Feinberg pointed out [Fei58] that universality of the Fermi interaction, if due to the exchange of an intermediate heavy boson, would lead to a value for this branching ratio of $B.R. = 10^{-4}$.This *unless* an explicit selection rule would forbid the $\mu \to e + \gamma$ transition through the graph

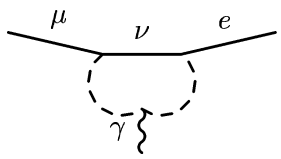

where the dashed line represents the intermediate boson. Now if the neutrinos associated with muons are different from neutrinos associated with electrons, then the branching ratio (2.2) produced by this same graph will be proportional to

$$|V_{\mu\nu_e} + V_{\nu_\mu e}|^2 \tag{2.3}$$

where $V_{\alpha\beta}$ are lepton family mixing coefficients.

In 1962 G. Danby et al [Dan62] publish an article establishing the existence of two kinds of neutrinos. They produced the first "neutrino beam" by inserting a beryllium target in a 15 GeV proton beam. The majority of the particles produced are pions moving in the general direction of the proton beam. In the "beamline" used, there was a 21 m long section of air followed by 13.5 meters of steel shielding (enough to absorb 17 GeV muons) and then the detector. No focussing elements were used. A 10-ton spark chamber detector surrounded by anticoincidence scintillators allowed to identify neutrino-induced events.

Using the first fifth of the detector as an additional veto, and after definition of a reasonable fiducial volume, events were classified in 4 categories: short single tracks of less than 300 MeV/c (not considered later on), single muons of at least 300 MeV/c (momentum was determined by range) with little or no vertex activity, vertex events (more than one track at the vertex) and showers (the remaining events: single track which look like photon or electron showers). Additional tests and logical arguments showed that the events were

not produced by cosmic rays or neutrons, that the "single track" events were indeed muons and that they were induced by the decay products of pions and kaons.

The probable existence of two kinds of neutrinos is then demonstrated by looking at single track events with more than 300 MeV/c track momentum: 34 events were identified as being single muons (category 2) of which 5 were expected to be due to cosmic-ray background, while only 6 of the shower events could be due to electrons. However, all these 6 events came during the first part of the run during which the neutron background was expected to be higher and they did not exhibit the typical spark distribution of electrons of 400 MeV/c. Note that one or two events are expected from electron-associated neutrinos produced in the $K^+ \to e^+ + \nu_e + \pi^0$ decay. The group concludes that the most plausible explanation for the absence of single electron events is that there are at least two types of neutrinos.

2.2.2 Indirect Evidence for the Existence of the Tau Neutrino

There is as yet no direct evidence for the existence of the tau neutrino. This means that a tau neutrino-induced charged-current interaction has never been explicitely observed through the identification of the produced tau lepton. On the other hand, a wealth of indirect evidence exists. Most of it comes from data suggesting the tau has a neutral, spin 1/2, weak isospin partner:

- Tau Existence
  After establishing the existence of a new particle, M. Perl et al. performed a deeper study of the properties of the "anomalous" events they observed [Perl75]. They conclude that if the events "*are to be explained by a single hypothesis, then they must arise from the decays of a pair of new particles each of which decays to a charged lepton and* **two** *neutrinos. This new particle is thus a candidate for being a heavy lepton with a mass in the range 1.6 to 2.0 GeV/c^2.*" This is the tau lepton. We will call one of the two neutrinos the tau neutrino (rather than neutrino x), while the other is associated with the decay lepton. We will assume it is the tau neutrino that is produced in hadronic tau decays.

- Three Types of Light Neutrinos
  From a precise determination of the mass and total width of the Z boson [1], combined with the hadronic pole cross-section and the ratios of the hadronic and leptonic partial decay widths of the Z, the number of light neutrinos ($m_\nu < 45GeV$) with standard coupling to the Z can be derived [Bar89]. Assuming the invisible decay width is purely due to escaping neutrinos, LEP obtains [LEP96]

  $$N_\nu = 2.989 \pm 0.012 \tag{2.4}$$

  N_ν is the number of light neutrino species and the error accounts for measurement errors as well as the uncertainties in the top mass ($m_t = 175 \pm 6GeV$) and the Higgs mass ($60\ GeV \leq m_H \leq 1000\ GeV$)

[1] These are obtained by extracting them from the so-called Z lineshape – i.e. the cross-section as a function of center-of-mass energy in the resonance region. The definition of the mass and width is based on the propagator in the lowest order Breit-Wigner approximation which leads to a denominator $(s - m_Z^2 + is\Gamma_Z/m_Z)$ in the matrix element. See reference [Bar89].

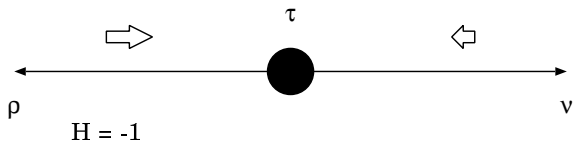

Figure 2.1: Spin alignments in $\tau^- \to \rho^- \nu_\tau$ decay in the tau restframe: if the tau neutrino has spin 3/2, the rho spin has to be aligned opposite to its direction of motion.

- The Tau Neutrino is not the Muon (or Electron) Neutrino
  If the tau neutrino were the muon (electron) neutrino, then we should observe that 50% of muon (electron) neutrino-induced charged current reactions produce a tau (if we are far above tau production threshold). The E531 collaboration [Ush86] searched for taus in charged current reactions induced by muon and electron neutrinos and did not find any candidates. Their result (after corrections for the tau threshold and acceptance effects) implies the following limits:

$$\Gamma(\tau^- \to l^- \overline{\nu_l} \nu_\mu) < 8.3 \times 10^{-13} MeV \quad (2.5)$$
$$\Gamma(\tau^- \to l^- \overline{\nu_l} \nu_e) < 3.0 \times 10^{-11} MeV \quad (2.6)$$
$$(2.7)$$

  which, compared to [PDG96]

$$\Gamma(\tau^- \to l^- \overline{\nu_l} \nu_\tau) = 4.18 \times 10^{-10} MeV \quad (2.8)$$

  clearly demonstrates that the tau neutrino is not the muon or the electron neutrino. Note however that this does not demonstrate that the neutrino produced in hadronic tau decays is not the muon or electron neutrino. This is an assumption we make based on our understanding of the weak interaction.

- Tau Neutrino Spin
  Fairly recently, the ARGUS collaboration demonstrated that the tau neutrino spin is 1/2 [Alb92] (under the assumption that the tau neutrino is massless) by measuring the spin alignment of the ρ in $\tau^- \to \rho^- \nu_\tau$ decays. Since the tau spin is 1/2 (see for example [Bac78]) and the ρ spin is 1, the spin of the tau neutrino can only be 1/2 or 3/2. But the latter would require that in the tau restframe the ρ spin projection always be aligned opposite to its direction of motion (never perpendicular), as illustrated in figure 2.1. The ARGUS analysis shows that the rho is also found with its spin perpendicular to its direction of motion, excluding the spin 3/2 possibility for the tau neutrino.

- Structure of the $\tau - \nu_\tau$ Interaction Vertex
  A few years after the tau dicovery, DELCO (Direct ELectron COunter) [Bac79] claimed it had confirmed the V-A structure[2] of the $\tau - \nu_\tau$ vertex to within 20 % by measuring the electron energy spectrum in the $\tau^- \to \nu_\tau e^- \overline{\nu_e}$ (and charge conjugate) decay, which is equivalent to measuring the Michel [Mic50] parameter ρ. They measured $\rho = 0.72 \pm 0.15$ and V-A theory predicts $\rho = 0.75$. Thus, the $\tau - \nu_\tau$ vertex

[2] Pure V-A interaction implies that only the left-handed components participate in the interaction. See for example [Okun82].

would be similar to the $e - \nu_e$ or $\mu - \nu_\mu$ vertices. However, this claim is not quite accurate:
Since the energy scale of the tau decay is small w.r.t. the W boson mass, we can describe the tau decay as an effective "contact" interaction. A convenient, clear way of representing this is in the so-called "helicity projection" form [Mur85], where each field's handedness is defined. The matrix element is then given by [Fet90]:

$$M = 4\frac{G_F}{\sqrt{2}} \sum_{\gamma=S,V,T} \sum_{\alpha,\beta=R,L} g^{\gamma}_{\alpha\beta} < \overline{l_\alpha}|\Gamma^\gamma|(\nu_l)_n >< (\overline{\nu_\tau})_m|\Gamma_\gamma|\tau_\beta > \tag{2.9}$$

where l represents either muon or electron, γ labels the type of interaction (scalar, vector, tensor), α and β represent the charged lepton helicities and the g's are the (complex) coupling constants. With γ, α and β given, the neutrino helicities are uniquely determined. In the Standard Model, $g^V_{LL} = 1$ and all the other coupling constants are zero. In experiments, we measure the energy spectrum of the final state charged lepton [PDG96]:

$$\begin{aligned}\frac{d^2\Gamma_{\tau\to l\nu\overline{\nu}}}{d\Omega dx} &\propto x^2 \\ &\times \left\{ 12(1-x) + \rho_\tau \left(\frac{32}{3}x - 8\right) + 24\eta_\tau \frac{m_l}{m_\tau}\frac{(1-x)}{x} \right. \\ &\left. -P_\tau \xi_\tau cos\theta \left[4(1-x) + \delta_\tau \left(\frac{32}{3}x - 8\right)\right]\right\}\end{aligned} \tag{2.10}$$

and this equation is valid in the tau restframe (this is for τ^-; for τ^+ the term with the tau polarization P_τ changes sign). $x = 2E_l/m_\tau$ is the scaled lepton energy and θ is the angle between the tau spin and the lepton momentum. ρ_τ , η_τ , ξ_τ and δ_τ are the Michel decay parameters, and they can be written in terms of six positive quantities $a^\pm, b^\pm$ and $c^\pm$ (see for example reference [Loh95]):

$$\begin{aligned} a^+ &= |g^V_{RL}|^2 + \frac{1}{16}|g^S_{RL} + 6g^T_{RL}|^2 \\ a^- &= |g^V_{LR}|^2 + \frac{1}{16}|g^S_{LR} + 6g^T_{LR}|^2 \\ b^+ &= |g^V_{RR}|^2 + \frac{1}{4}|g^S_{RR}|^2 \\ b^- &= |g^V_{LL}|^2 + \frac{1}{4}|g^S_{LL}|^2 \\ c^+ &= \frac{3}{16}|g^S_{RL} - 2g^T_{RL}|^2 \\ c^- &= \frac{3}{16}|g^S_{LR} - 2g^T_{LR}|^2 \end{aligned}$$

	g^S_{RR}	g^S_{RL}	g^S_{LR}	g^S_{LL}	g^V_{RR}	g^V_{RL}	g^V_{LR}	g^V_{LL}	g^T_{RL}	g^T_{LR}
a	0.27	1.	0.36	1.	0.28	0.52	0.28	1.	0.90	0.36
b	0.	1.	0.	1.	0.	0.5	0.	1.	0.86	0.

Table 2.1: Limits on the moduli of the various reduced coupling constants $g^\gamma_{\alpha\beta}/max|g^\gamma_{\alpha\beta}|$: a) using the present data and b) with infinitely precise Michel parameter values in agreement with Standard Model predictions. The values are taken from reference [Loh95].

such that we get

$$\rho = \frac{3}{4}\left(b^+ + b^-\right) + \left(c^+ + c^-\right) \tag{2.11}$$

$$\eta = \frac{1}{2}Re\left[g^V_{RL}(g^{S*}_{LR} + g^{T*}_{LR}) + g^V_{LR}(g^{S*}_{RL} + g^{T*}_{RL}) + g^V_{RR}g^{S*}_{LL} + g^V_{LL}g^{S*}_{RR}\right] \tag{2.12}$$

$$\xi = 3\left(a^- - a^+\right) + \left(b^- - b^+\right) + \frac{7}{3}\left(c^+ - c^-\right) \tag{2.13}$$

$$\xi\delta = \frac{3}{4}\left(b^- - b^+\right) + \left(c^+ - c^-\right) \tag{2.14}$$

We see that the measurement $\rho = 0.75$ in itself does not allow to exclude a V+A structure for example. From the equations (2.11) to (2.14) and using the experimental values of the Michel parameters[3], model independent limits can be set on the moduli of the various couplings. The present and potential limits are given in table (2.1). There is still quite some room for non-standard couplings and we see that the Michel parameters alone are not sufficient to fully exclude these even with perfect measurements. One solution would be to measure the cross-section for the reaction $\nu_\tau + e \to \tau + \nu_e$ since this will put a lower limit on g^V_{LL}. Combined with the tau lifetime this then allows to put an upper limit on the other coupling constants.

- The Tau Has a Weak Isospin Partner

  The weak neutral current, unlike the charged current, is not purely left-handed. It contains a right-handed component such that we can write it in the form (see for example [Okun82]):

$$j^{WNC}_\alpha = \sum_i \left(g^i_L\overline{\psi_i}\gamma_\alpha\left(1-\gamma_5\right)\psi_i + g^i_R\overline{\psi_i}\gamma_\alpha\left(1+\gamma_5\right)\psi_i\right) \tag{2.15}$$

  where the sum is over the twelve fermions (6 quarks and 6 leptons), ψ represents a Dirac spinor such that $(\not{p} - m)\,\psi = 0$, $\overline{\psi} = \psi^+\gamma^0$ and g^i_L and g^i_R are numerical coefficients[4]. In the Standard Model they are related to the electric charge and the weak isospin of the particle:

$$g_L = T_3 - Qsin^2\theta_W \tag{2.16}$$

$$g_R = -Qsin^2\theta_W \tag{2.17}$$

[3]These values are measured by studying the kinematics of tau decay [Bus95a]. The value of η_τ, which appears in the term related to the mass of the charged lepton to which the tau decays, is determined with better precision from the ratio $\frac{BR(\tau\to\mu\nu\overline{\nu})}{BR(\tau\to e\nu\overline{\nu})}$ see [Sta94].

[4]Here we have taken $\gamma_5 = \begin{pmatrix} 0 & 1 \\ 1 & 0 \end{pmatrix}$. L. Okun takes $\gamma_5^{Okun} = -\gamma_5$, but this is a matter of convention only. With our convention, we will obtain $(g_V - g_A\gamma_5)$ rather than $(g_V + g_A\gamma_5)$.

Here Q is the particle's electric charge, T_3 is the third component of its weak isospin and θ_W is the Weinberg angle. We see that weak neutral current interactions can help us determine a particle's weak isospin. Usually the current of equation (2.15) is rewritten as

$$j_\alpha^{WNC} = \sum_i \left(\overline{\psi_i}\gamma_\alpha \left(g_{Vi} - g_{Ai}\gamma_5\right)\psi_i\right) \tag{2.18}$$

with

$$g_V = g_L + g_R = T_3 - 2Qsin^2\theta_W \tag{2.19}$$

$$g_A = g_L - g_R = T_3 \tag{2.20}$$

Experiments at the Z-pole at LEP and SLC have recorded an impressive number of neutral current interactions with charged leptons from the

$$Z \to l^- l^+ \tag{2.21}$$

events (here l is any charged lepton). Let us define θ as being the angle of the l^- direction with respect to the electron beam direction. The parity violation manifests itself through the asymmetry of the cross-section of process (2.21) as a function of θ, as can be seen in figure 2.2.

It is quantified by extracting

$$\mathcal{A}_l = \frac{2g_{Vl}g_{Al}}{g_{Vl}^2 + g_{Al}^2} \tag{2.22}$$

from the data (here we did not assume that the coupling constants are identical for all charged leptons, so-called lepton universality). The asymmetry yields the ratio g_{Vl}/g_{Al} and the leptonic partial widths yield the sum of the squares of the couplings:

$$\Gamma_{ll} = \frac{G_F m_Z^3}{6\pi\sqrt{2}}\left(g_{Vl}^2 + g_{Al}^2\right)\left(1 + \delta_l^{QED}\right) \tag{2.23}$$

where δ_l^{QED} accounts for final state photonic corrections. For high-precision results corrections due to the lepton masses (which are neglected in equation 2.23) are mandatory. Note that using this input one sign ambiguity remains. We follow the convention $g_{Ae} < 0$.

Values of the coupling constants obtained by LEP, as well as the combination of these results with the SLD results on A_{LR} are shown in table 2.2.

We see that the tau, just like the electron and the muon, has weak isospin -1/2, indicating it has a weak isospin partner. Furthermore, the tau, muon and electron couplings to the weak neutral current are identical to within 1 %, strongly suggesting lepton universality.

In conclusion, although the tau neutrino has not been directly observed[5], there is a lot of indirect evidence for its existence and similarity to the electron and muon neutrinos. It therefore seems reasonable to accept its existence: we shall assume it is the third generation neutral lepton, weak isospin partner of the tau.

[5] At the time of this writing, an experiment [Lun94] has started datataking at Fermilab hoping to directly confirm the existence of the tau neutrino. The detection technique is similar to Chorus but the tau neutrino content of the beam is proportionally much higher: the Fermilab 800 GeV proton beam is used to produce D_s mesons in a beam dump (there is no decay tunnel), thus providing a large flux of tau neutrinos.

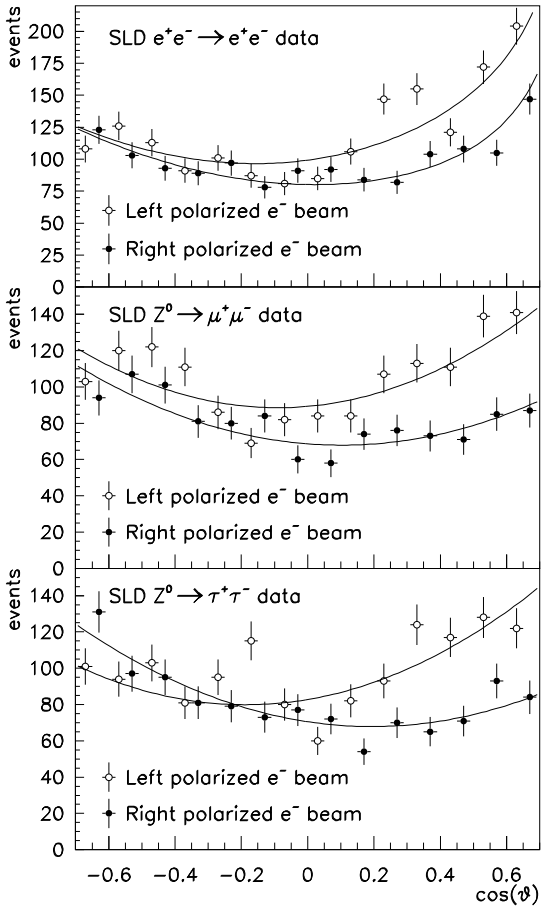

Figure 2.2: Polar angle distribution for Z decays to e, μ and τ pairs for the SLD 94-95 run [Abe97]. The asymmetry is clearly visible, even in the electron sample where there is a contribution from the electromagnetic interaction. Note that SLC has a polarized electron beam, which allows them to control the direction of the spin projection of the Z.

	LEP	LEP+SLD
g_{Ve}	-0.0368 ± 0.0015	-0.03828 ± 0.00079
$g_{V\mu}$	-0.0372 ± 0.0034	-0.0358 ± 0.0030
$g_{V\tau}$	-0.0369 ± 0.0016	-0.0367 ± 0.0016
g_{Ae}	-0.50130 ± 0.00046	-0.50119 ± 0.00045
$g_{A\mu}$	-0.50076 ± 0.00069	-0.50086 ± 0.00068
$g_{A\tau}$	-0.50116 ± 0.00079	-0.50117 ± 0.00079
$g_{V\mu}/g_{Ve}$	1.01 ± 0.11	0.935 ± 0.085
$g_{V\tau}/g_{Ve}$	1.001 ± 0.062	0.959 ± 0.046
$g_{A\mu}/g_{Ae}$	0.9989 ± 0.0018	0.9993 ± 0.0017
$g_{A\tau}/g_{Ae}$	0.9997 ± 0.0019	1.0000 ± 0.0019

Table 2.2: Values for the effective vector and axial-vector couplings obtained by LEP and combination of these values with the values of $g_{Vl} - g_{Al}$ from the A_{LR} measurements performed at SLD. The individual values obtained by the experiments have been combined by the LEP Electroweak Working Group [LEP96].

2.3 Neutrinos in the Standard Model

What follows is a very short summary of the properties of neutrinos in the Standard Model; for more details consult the very extensive literature, for example reference [Okun82].

In the Standard Model neutrinos are massless neutral leptons. They are the weak isospin partners of the charged leptons: the electron neutrino forms a weak isospin doublet with the electron, the muon neutrino with the muon and the tau neutrino with the tau. We say there are three neutrino flavors. Only left-handed neutrinos (and right-handed anti-neutrinos) exist. The weak charged current can be written in a form analog to that of the weak neutral current of equation (2.18):

$$j_\alpha^{WCC} = \sum_i \left(\overline{\psi_f} \gamma_\alpha \left(1 - \gamma_5\right) \psi_i \right) \tag{2.24}$$

Here $f = e, \mu, \tau, d', s', b'$ [6] and i is the corresponding weak isospin partner $\nu_e, \nu_\mu, \nu_\tau, u, c$ and t. We see that the weak charged current is exclusively lefthanded as opposed to the weak neutral current which contains a right-handed component. This is why the right-handed quarks and charged leptons are in weak isospin singlets.

We can assign an additive "lepton family number" to each of the leptons: electron number is equal to 1 for the electron and electron neutrino, -1 for the positron and electron anti-neutrino, etc. As can be seen from the form of the weak charged and neutral currents (equations (2.24) and (2.18) respectively), the weak interactions conserve this lepton family number, which means a muon-neutrino induced interaction always has a muon or muon neutrino in the final state for example. An important consequence of this is that in the Standard Model neutrinos cannot change flavour by any means.

2.4 Neutrino Masses

2.4.1 Neutrino Mass Eigenstates

Before talking about the experimental limits on neutrino masses and the reasons why we believe neutrinos are probably massive, it is important to define the neutrino mass eigenstate lest the whole discussion make very little sense.

Now if neutrinos have masses, then the left-handed flavor eigenstate neutrinos

$$\nu_{fL} = \left(\frac{1 - \gamma_5}{2} \right) \psi_{\nu_f} \tag{2.25}$$

(f represents e, μ or τ) are linear combinations of the left-handed projections of the neutrino mass eigenstates ν_m:

$$\nu_{fL} = \sum_{m=1}^{n} U_{fm} \nu_{mL} \tag{2.26}$$

[6] d', s' and b' are orthonormalized linear combinations of the d, s and b quarks. Their introduction makes a unified description of the weak charged current interactions of leptons and hadrons possible. They were introduced for the four quark case by Cabibbo in 1963 [Cab63] and the idea was generalized to the six quark case by Kobayashi and Maskawa in 1973 [Kob73]. A good description is given in reference [Hal84].

where n is the number of mass eigenstates and U is an orthonormal mixing matrix. This means the (leptonic) weak charged current of equation (2.24) becomes:

$$j_\alpha^{WCClept} = \sum_{f=e,\mu,\tau} \left(\overline{l_{fL}} \gamma_\alpha \left(\sum_{m=1}^{n} U_{fm} \nu_{mL} \right) \right) \tag{2.27}$$

The weak charged current couples each charged lepton to every neutrino mass eigenstate with an amplitude proportional to the appropriate U_{fm} matrix element.

Assuming the mixing terms are relatively small (U nearly diagonal) as in the quark sector, then each of the flavor eigenstates nearly overlaps with one of the mass eigenstates and only involves minor quantities of the others. We can associate ν_e predominantly with ν_1, ν_μ with ν_2 and ν_τ with ν_3. So when we speak about the "mass" of the electron neutrino, we're really speaking about the mass of ν_1 and the same applies to the muon and tau neutrino "masses".

2.4.2 Direct Neutrino Mass Measurements

- ν_1 Mass
  The bound on the mass of ν_1 is obtained by measuring the shape of the electron spectrum in tritium β-decays. A non-zero ν_1 mass would lower the maximum electron energy so that it should be measurable at the upper end of the spectrum (the so-called endpoint). Unfortunately, in nuclear β-decay a finite neutrino mass only visibly affects an interval of about $\Delta(E) \approx 3m_\nu$ just below the endpoint (see for example reference [Ott95]), which corresponds to a fraction

  $$\Gamma_{\Delta(E)}/\Gamma_{tot} \approx 2\left(\Delta(E)/E_0\right)^3 \tag{2.28}$$

  of the total decay rate (E_0 is the endpoint energy). This implies that the experiments do not only need a very good resolution, but also have to deal with a huge background from the lower end of the spectrum: some part of these events (10 orders of magnitude more than the interesting ones) could sneak through in some very small tail of a distribution. By fitting the measured curve the experiments obtain a value for the square of the ν_1 mass.

  All of these experiments (a list is readily available in reference [PDG96]) obtain a (for some significantly) negative value for $m_{\nu_1}^2$, which is unphysical. The origin of this value generally seems to depend on the experiment: in the Troitsk experiment [Bel95] there is a very small monoenergetic component in the spectrum just 7 eV below the endpoint, while in the Mainz experiment [Ott95] the problem lies in an excess of events further away from the endpoint. This causes their fit to underestimate the position of the endpoint such that it sees an artificial excess of events *beyond* the endpoint, leading to a negative value for $m_{\nu_1}^2$. Note that the obtained value for $m_{\nu_1}^2$ is strongly correlated with the size of the interval on which the fit is performed.

  To conclude, the tritium β-decay experiments appear to suffer from not fully understood systematics, and it seems safer at this moment to take a rather conservative approach. The Particle Data Group chose to take $m_{\nu_1} < 15\ eV/c^2$.

- ν_2 Mass
  The ν_2 mass is constrained by measuring the muon momentum in $\pi^+ \rightarrow \mu^+ + \nu_\mu$

decays. Combined with the best knowledge of the muon and pion masses as well as four-momentum conservation, this yields the square of the ν_2 mass with high accuracy. The present best limit is $m_{\nu_2} < 170\ keV/c^2$ [Ass96].

- ν_3 Mass
  The best limit on the ν_3 mass is obtained from the kinematics of hadronic tau decays. The OPAL Collaboration [Ake95] has slightly improved the method by fitting not only the invariant mass spectrum of the hadrons produced but also the energy of the hadronic system. The best result using this method has been obtained by the ALEPH Collaboration [Bus95b]. From a fit using 25 $\tau \rightarrow 5\pi(\pi^0)\nu_\tau$ events they derived $m_{\nu_3} < 24\ MeV/c^2$ at 95 % CL [7].

  Note that they have been rather lucky in the sense that 5 events are in the "sensitive" region : this is the region where, given a distribution of events limiting the neutrino mass to $28 MeV/c^2$ at 95 % CL, any additional event in the region (with typical errors on its kinematics) will improve the limit by more than $1 MeV/c^2$. This is clearly visible in figure 2.3. In their case, the probability of observing 5 events in this region is only about 5% (this is model dependent and 5 % is the highest value; other models lead to 1%).

  The Chorus experiment will attempt to constrain the ν_3 mass using the kinematics of $D_s \rightarrow \tau^+\nu_\tau$ decays. It is however extremely unlikely that the result will be competitive with the existing limit.

2.4.3 Theoretical Considerations on Neutrino Masses

In the Standard Model particle masses cannot be computed: they are parameters measured by experiment. But in a more complete high-energy theory we would like to minimize the number of free parameters and be able to predict particle masses from fundamental principles of the theory. In the following, we give a short introduction to the subject. For more complete treatment see for example reference [Alt94].

Dirac and Majorana Particles

Neutrinos do not only stand out among leptons and quarks because of their extremely small masses, but also because they are neutral. Let us start by considering any of the charged fermions: it is distinct from its antiparticle (since it has opposite charge) and Lorentz invariance imposes the existence of both helicities (since we can "overtake" the particle, putting ourselves in a reference frame where the direction of motion is reversed while the spin component is the same). These particles are Dirac particles consisting of four states (particle with spin up, particle with spin down, antiparticle with spin up and antiparticle with spin down) with identical mass. In the case of neutrinos however, the possibility exists that the neutrino is its own antiparticle since it is neutral. Such particles are called Majorana particles (Majorana proposed in 1937 [Maj37] that a neutral fermion could have this property). It is clear that Majorana particles only have 2 distinct states and if neutrinos are Majorana particles then lepton number is violated.

[7] On October 20th, 1997, ALEPH has submitted a new paper to *Z. Phys.* C in which they combine the three- and five-prong tau decays to constrain the tau neutrino mass. They obtain a new upper limit $m_{\nu_3} < 18.2\ MeV/c^2$ at 95 % CL [Bar97].

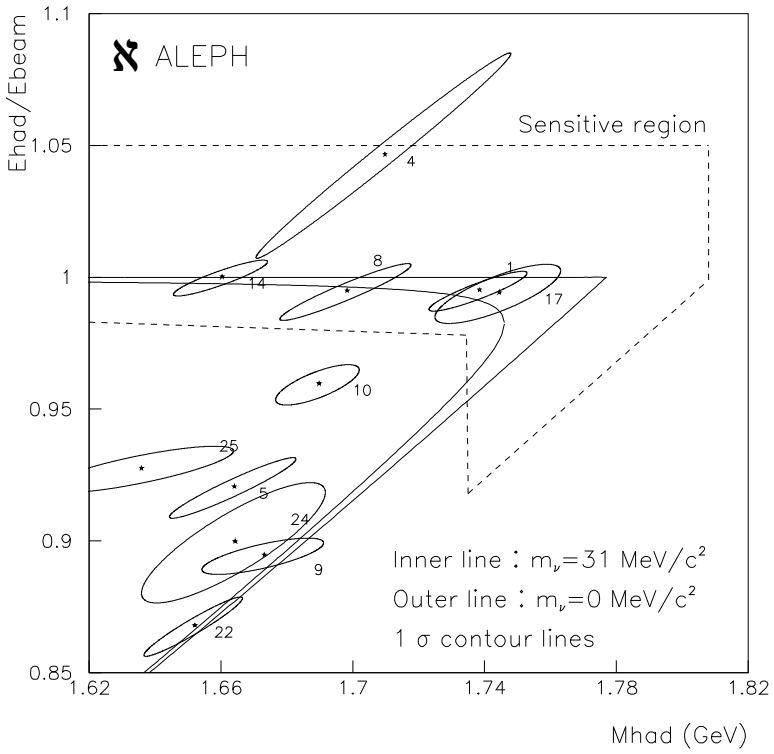

Figure 2.3: Distribution of E_{had}/E_{beam} (fraction of the tau energy carried by the hadronic decay products) versus hadronic invariant mass of data events in the range $m_{had} > 1.62 GeV/c^2$ and $E_{had}/E_{beam} > 0.85$ [Bus95b]. The ellipses indicate the errors on the measured values for each event and the full lines delimit the kinematically allowed region for two different values of the neutrino mass. The dashed line delimits the sensitive region defined in the text. Event 1 improves the limit on the ν_3 mass by $5.3 MeV/c^2$.

The Seesaw Mechanism

In a gauge field theory of electroweak interactions, two distinct types of neutrino mass terms can appear: **Dirac** mass terms of the form

$$-m_D\,(\overline{\nu_L}\nu_R + \overline{\nu_R}\nu_L) \tag{2.29}$$

and **Majorana** mass terms of the form

$$-\frac{1}{2}m_M^L\left(\overline{\nu_L}(\nu_L)^c + \overline{(\nu_L)^c}(\nu_L)\right) - \frac{1}{2}m_M^R\left(\overline{\nu_R}(\nu_R)^c + \overline{(\nu_R)^c}(\nu_R)\right) \tag{2.30}$$

Here ν represents a neutrino field, the subscript L or R denotes the helicity and

$$\nu^c = C\overline{\nu}^T = C\gamma_0\nu^* \tag{2.31}$$

is the charge-conjugated field[8] (C is a charge-conjugation matrix).

A Dirac mass term like (2.29) corresponds to "overtaking" the neutrino and a Majorana mass term like (2.30) changes a neutrino into the corresponding antineutrino, violating lepton number. We will see that in most Grand Unified Theories (GUTs) the ν_R exists and lepton number is not conserved, such that Dirac and Majorana mass terms are naturally present in the Lagrangian. Gell-mann, Ramond and Slansky [Gel79] and independently Yanagida [Yan80] pointed out that the smallness of neutrino masses could be caused by the extremely large value of the Grand Unification Scale M_{GUT}: if both terms are present in the Lagrangian, then these terms can be combined in a matrix notation such that we get:

$$\mathcal{L}_{mass} = -\frac{1}{2}\left(\overline{\nu_L}\,\overline{(\nu_R)^c}\right)\mathcal{M}\begin{pmatrix}(\nu_L)^c\\ \nu_R\end{pmatrix} + h.c. \tag{2.32}$$

where $\mathcal{M}$ is the "seesaw" matrix

$$\mathcal{M} = \begin{pmatrix} m_M^L & m_D \\ m_D & m_M^R \end{pmatrix} \tag{2.33}$$

Assuming a hierarchy in the values of the elements of $\mathcal{M}$

$$m_M^R = M \gg m_D \gg m_M^L = \mu \tag{2.34}$$

with μ negligible or zero, then one (set of) particle(s) becomes light while another becomes heavy (a "seesaw" effect).

Let us illustrate this in the case of one generation. The mass matrix (2.33) has one heavy eigenvector $N \approx [\nu_R + (\nu_R)^c] + (m_D/M)\,[\nu_L + (\nu_L)^c]$ which consists mainly of the sterile ν_R, and one light eigenvector $\nu \approx [\nu_L - (\nu_L)^c] + (m_D/M)\,[\nu_R - (\nu_R)^c]$, which consists mainly of the active ν_L. Their masses are the eigenvalues of the matrix:

$$m_N \approx M, \quad m_\nu \approx \left|\mu - \frac{m_D^2}{M}\right| \tag{2.35}$$

[8] By applying the operation (2.31) to for example ν_L, we get $(\nu_L)^c = (\nu^c)_R$, while under charge conjugation we should have $\nu_L \to (\nu)_L^c = (\nu_R)^c$. The reason for this is that the charge-conjugation operation (2.31) and helicity projection do not commute. This also implies that an interaction containing only lefthanded fields must violate charge-conjugation maximally.

Note here that we can take the absolute value without any problems: we can absorb a negative sign in a redefinition of the field. We see that $m_\nu M \approx m_D^2$, such that if m_D is of the order of the charged lepton and quark masses, the hierarchy assumption (2.34) is satisfied and the smallness of neutrino masses is naturally explained. Furthermore, the four states involved in the mass term (2.32) reduce to two neutrinos with different masses after diagonalization, such that each of these can only have two states and has to be a Majorana neutrino.

In the more general, three generations case, the neutrinos in (2.32) become vectors and M, m_D and μ are matrices. The heavy and light eigenvectors are found diagonalizing the matrices

$$m_N = M, \quad m_\nu = \mu - m_D M^{-1} m_D^T \tag{2.36}$$

In the simple seesaw model, there are as many right- as left-handed neutrinos such that we have three light and three heavy neutrinos with masses

$$\frac{m_{D1}^2}{M_1},\ \frac{m_{D2}^2}{M_2},\ \frac{m_{D3}^2}{M_3},\ M_1,\ M_2,\ M_3 \tag{2.37}$$

where M_i and m_{Di} are the eigenvalues of matrix M and m_D respectively. The Dirac masses m_{Di} could be similar to the up-quark masses or to the charged lepton masses, and the heavy masses M_i could just be similar $M_i \approx M$ (quadratic seesaw) or follow the same hierarchy as the m_{Di} (linear seesaw).

We see that although the seesaw model is extremely appealing in the sense that it gives a natural qualitative explanation of the smallness of neutrino masses, it still leaves too many possible reasonable combinations to use it for quantitative goals.

Neutrinos in Cosmology

Present cosmological knowledge [Ell96] favors a combination of Hot and Cold Dark Matter, (HDM and CDM respectively) with $\Omega_{Cold} \approx 0.7$ and $\Omega_{Hot} \approx 0.2$. [9] Should this be correct, then the most likely candidate (and in fact the only one known to exist) for HDM would be a massive neutrino with $m_\nu \approx 5eV$. We will see later in section 3.3.3 that such a mass for the tau neutrino is consistent with $m_{\nu_\mu} = 2\ 10^{-3} eV$ expected in the MSW interpretation of the solar neutrino deficit and with the ratio $(m_t/m_c)^2$ expected in the simple seesaw model.

Grand Unification Theories

We would like to develop a model which is much more *predictive* than the Standard Model, eliminating the flurry of phenomenological parameters necessary to fit the data (quark masses, coupling constants etc.). The natural way to do this is to identify more *symmetries* of nature. Since the data fits the Standard Model so well, these symmetries probably only become really apparent at higher energies, but we can nevertheless exclude symmetries whose small effects we should have observed in high-precision experiments (powerful constraints can be derived on lepton flavor changing neutral currents for example from the non-observation of the decay $\mu \to e + \gamma$ at the $B.R. = 10^{-11}$ level).

[9] $\Omega = \rho/\rho_c$, where ρ is the energy density of the universe and ρ_c is the critical density. If $\Omega < 1$, the universe will expand forever, if $\Omega > 1$ the universe will collapse at some stage and if $\Omega = 1$ the universe is flat, i.e. its expansion slows asymptotically to a stop. Inflationary cosmology (the current prefered scenario) implies $\Omega = 1$.

The general idea is to group quarks and leptons into irreducible representations of a larger group: we suppose that when we use the renormalization group equations to run the electromagnetic, weak and strong coupling constants to their values at very high energies, they unify and the particles become indistinguishable. It is interesting to observe that thanks to the precision reached by the experiments this coupling constant unification "constraint" (it is of course only a constraint if we admit that the forces *have* to unify) can already serve to select or reject certain models. The running of the constants is indeed model dependent. A good example of this is given in figure (2.4): Standard Model unification is inconsistent with the present experimental values while the Minimal Supersymmetric Standard Model (MSSM) does rather well.

In these models we can let particles acquire mass in the standard way: through Yukawa couplings to the Higgs particles (see for example reference [Che84]). The gain comes from the fact that at the unification scale (M_{GUT}) a quark+lepton multiplet couples to a Higgs multiplet with just **one** Yukawa coupling (instead of having one Yukawa coupling per particle). For example in an $SU(5)$ model 3 down quarks can match up with a lepton doublet (the first 3 indices then correspond to the $SU(3)_c$ color and the last 2 to the $SU(2)_L$ weak isospin). We obtain $\lambda_e = \lambda_d$, $\lambda_\mu = \lambda_s$ and $\lambda_\tau = \lambda_b$ at M_{GUT}, where λ_i is the relevant Yukawa coupling. We then have to use the renormalization group equations to run these relations down to the weak scale to be able to compare with experiment. Of course this is just an example to give a rough idea of the principle, but the situation is highly more complex and there are many reasons to go to larger groups (the group choice determines the situation at M_{GUT}) and include supersymmetry (the model affects the renormalization group equations needed to relate what happens at M_{GUT} with experiment). A more complete discussion is given for example in reference [Raby94].

Where it becomes very interesting concerning neutrinos is that in one of the more attractive options [Ross84], namely SUSY $SO(10)$ GUT ,the ν_R exists *and* B-L is a gauge symmetry. But B-L must be broken at some level since we do not observe a long-range force associated with it, so this could naturally generate Majorana masses for neutrinos (in a way analog to the Higgs mechanism) near the B-L breaking scale.

Conclusion

We have seen that SUSY GUTs are very attractive for many reasons. They provide a framework to reduce the number of free parameters and some models fit the low energy data admirably well. In addition to that, they can potentially offer a natural explanation for the presence of Dirac and Majorana mass terms through the existence of right-handed neutrinos and lepton number violation. These terms in their turn offer an elegant solution to the mystery of the smallness of neutrino masses though the seesaw mechanism. We see that the observation and measurement of neutrino masses could potentially open a window to physics at very large energy scales.

2.5 Neutrino Oscillations

Already in 1957, i.e. before much more was known about neutrinos than the fact that they exist (see section 2.1), B. Pontecorvo realized [Pon57] that "*if the conservation law of neutrino charge would not apply, then in principle neutrino $\rightarrow$ antineutrino transitions could take place in vacuo*". Although he was not aware of the existence of multiple neutrino flavours, Pontecorvo identified the essential principle of what we today call neutrino

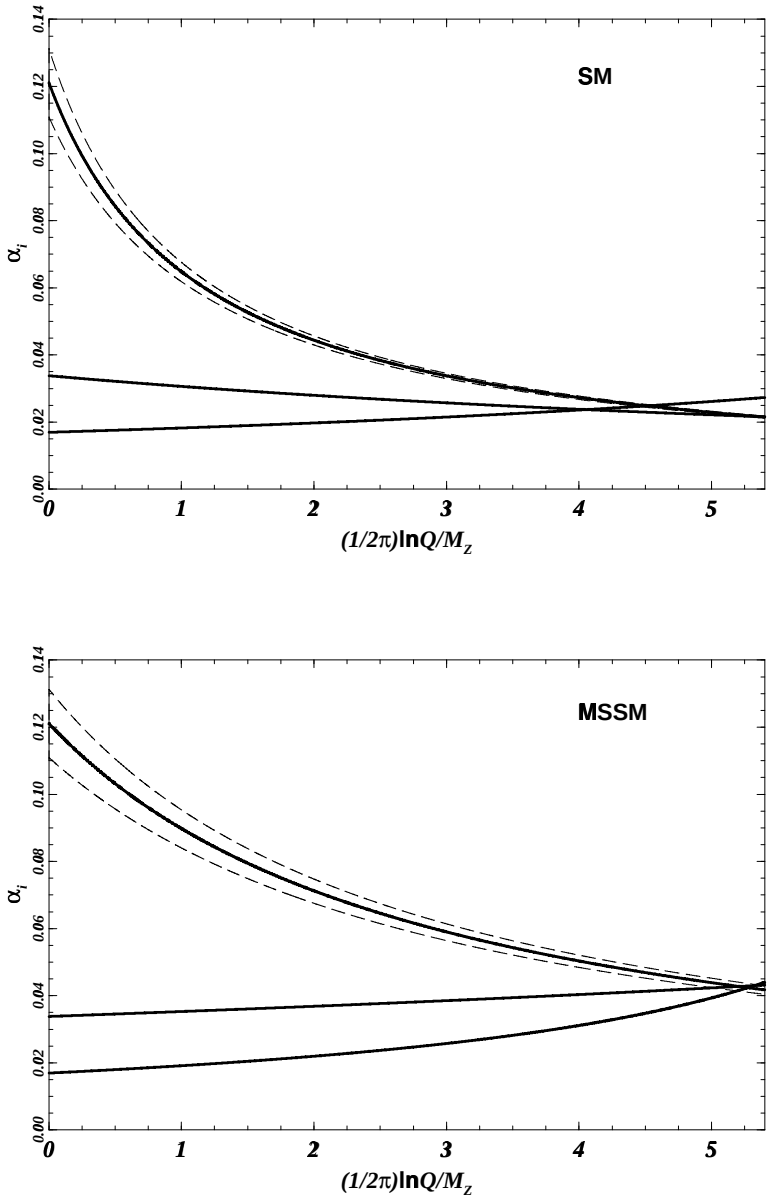

Figure 2.4: Running of the coupling constants α_1 (lower curve), α_2 (middle curve) and α_3 (upper curve) as a function of the scale parameter $t' = \frac{1}{2\pi} ln \frac{Q}{M_Z}$ for 2 models: the Standard Model (top) and the Minimal Supersymmetric Standard Model (bottom) [Pol94]. α_1 is the $U(1)_Y$ coupling constant: $\alpha_1(M_Z) = \frac{5}{3} \frac{\alpha(M_Z)}{1 - sin^2\theta_W(M_Z)}$, α_2 is the $SU(2)_L$ coupling constant: $\alpha_2(M_Z) = \frac{\alpha(M_Z)}{sin^2\theta_W(M_Z)}$, and α_3 is the $SU(3)_c$ coupling constant: $\frac{\alpha_3(M_Z)}{1 + \frac{\alpha_3(M_Z)}{4\pi}} = \alpha_s(M_Z)$. Here α is the usual fine structure constant, α_s is the strong coupling and $sin^2\theta_W$ is the weak mixing angle. The dashed lines show the uncertainty on α_3.

oscillations.

We have seen in section 2.4 that the neutrino mass and weak (or flavor) eigenstates are not necessarily identical. Let us recall equation (2.26) here (albeit with the small modification that we do not require left-handedness anymore):

$$|\nu_f\rangle = \sum_m U_{fm} |\nu_m\rangle \tag{2.38}$$

with U an orthonormal mixing matrix. So, suppose at a time $t = 0$ we have a neutrino of momentum p produced in association with a lepton of flavor f (for example in the decay $\pi^+ \to \mu^+ + \nu_\mu$). According to (2.38), at $t = 0$, the state $|\nu_f\rangle$ of this neutrino is a superposition of states $|\nu_m\rangle$ of energy

$$E_m = \sqrt{p^2 + M_m^2} \approx p + \frac{M_m^2}{2p} \tag{2.39}$$

where M_m is the mass of the ν_m and on the right we have assumed that $M_m \ll p$ (the neutrino is relativistic). Therefore, after a time t we have

$$|\nu_f(t)\rangle = \sum_m U_{fm} |\nu_m\rangle e^{-iE_m t} \tag{2.40}$$

$$\approx e^{-ipt} \sum_m U_{fm} |\nu_m\rangle e^{-i(M_m^2/2p)t} \tag{2.41}$$

Using unitarity[10] of the matrix U we also have

$$|\nu_m\rangle = \sum_{f'} U^*_{f'm} |\nu_{f'}\rangle \tag{2.42}$$

Inserting (2.42) in (2.41) we find

$$|\nu_f(t)\rangle \approx e^{-ipt} \sum_{f'} \left[\sum_{m=1}^{3} U_{fm} e^{-i(M_m^2/2p)t} U^*_{f'm} \right] |\nu_{f'}\rangle \tag{2.43}$$

Pontecorvo's argument is now clear: after a time t, if the quantum number which distinguishes neutrinos from each other (i.e. lepton flavour) is not conserved, our neutrino which started out as a pure ν_f has now evolved into a superposition of all the flavours. We can now easily evaluate the probability that the neutrino born with flavor f will be found with flavor f' at a distance x (which is equivalent to the time t since the neutrino has been supposed to be relativistic):

$$P\left(\nu_f \to \nu_{f'}; x\right) \approx \left| \sum_m U_{fm} e^{-i(M_m^2/2E_\nu)x} U^*_{f'm} \right|^2 \tag{2.44}$$

While our approximation of relativistic neutrinos is well justified in the light of the energies of neutrinos detected by experiments ($\mathcal{O}(MeV)$ or higher) combined with the present limits on neutrino masses (see section 2.4.2), it's obvious that taking an elementary particle

[10]Strictly speaking, if neutrinos are Majorana particles, the unitarity constraint $\sum_f U^*_{fm} U_{fm'} = \delta_{mm'}$ does not necessarily hold. But we can reasonably suppose that the heavy Majorana neutrinos are heavier than 45 GeV and are only negligible admixtures of the three usual flavor eigenstates.

at a fixed point and with a fixed momentum cannot be correct. However, more rigourous quantum mechanical wavepacket treatments of neutrino oscillations have been performed [Kay81] and they yield the same result as obtained in our simplified treatment. It should be noted that in experiments with non-relativistic neutrinos results can be significantly different though [Giu91].

Usually experiments only consider oscillations between two neutrino flavors for simplicity[11], so we will quickly review the scheme for the $\nu_\mu \leftrightarrow \nu_\tau$ case.

There are two flavor eigenstates ν_μ and ν_τ, and two mass eigenstates ν_1 and ν_2. At $t = 0$ they are related by:

$$|\nu_\mu\rangle = cos\theta\,|\nu_1\rangle + sin\theta\,|\nu_2\rangle \tag{2.45}$$
$$|\nu_\tau\rangle = -sin\theta\,|\nu_1\rangle + cos\theta\,|\nu_2\rangle \tag{2.46}$$

After a time t they have evolved to:

$$|\nu_\mu(t)\rangle = cos\theta e^{-iE_1 t}\,|\nu_1\rangle + sin\theta e^{-iE_2 t}\,|\nu_2\rangle \tag{2.47}$$
$$|\nu_\tau(t)\rangle = -sin\theta e^{-iE_1 t}\,|\nu_1\rangle + cos\theta e^{-iE_2 t}\,|\nu_2\rangle \tag{2.48}$$

such that we find

$$P\left(\nu_\mu \rightarrow \nu_\tau\right) = sin^2 2\theta sin^2\left(\frac{1}{4}\Delta m^2 \frac{L}{E}\right) \tag{2.49}$$

$\Delta m^2 = \left|m_2^2 - m_1^2\right|$ is the difference between the squares of the masses of the two mass eigenstates, L is the length between the neutrino production point and the detection point (the "baseline") and E is its energy. We can make a few interesting comments based on equation (2.49):

- We can define the "oscillation length" $L_{osc} = 4\pi\frac{E}{\Delta m^2}$, which is the length needed to go from ν_μ to ν_τ and back to ν_μ.[12]

- The Δm^2 sensitivity of an experiment is determined by its $\frac{L}{E}$ value: low energy, long baseline experiments are sensitive to lower values of Δm^2.

- At large Δm^2, the oscillation probability becomes

$$P\left(\nu_\mu \rightarrow \nu_\tau\right) = \frac{1}{2} sin^2 2\theta \tag{2.50}$$

- Oscillations are a very powerful way to search for neutrino masses: although they require the existence of a mixing angle, a typical high-energy neutrino experiment with 1 GeV average neutrino energy and a 1 km baseline is sensitive to Δm^2 of the order of 1 eV^2. And this is the "worst" experimental situation (for Δm^2 sensitivity).

[11] This approach assumes mixing with the third family is negligible w.r.t. the mixing between the two considered families. There is no solid argument to back up this hypothesis, but it allows to show results of experiments in so-called "exclusion plots" which give a clear idea of the sensitivity.

[12] Note that $P(\nu_\alpha \rightarrow \nu_\beta) = P(\nu_\beta \rightarrow \nu_\alpha)$ is always true for two-flavor mixing, but only holds for three-flavor mixing if CP is conserved [Cab78].

2.6 Conclusions

The existence of three flavors of "light", Standard Model neutrinos, even if there has not yet been any "direct" observation of the tau neutrino, is fairly well established. While in the Standard Model neutrinos are massless, we have seen that in the light of cosmology and higher-energy theories, neutrinos are likely to be massive. In this case, there is the distinct possibility that neutrinos could oscillate from one flavor to another as they propagate, thus providing a powerful way to prove the existence of their masses. We will see in the next chapter that many experimental results are compatible with massive, oscillating neutrinos.

Chapter 3

Recent Results from Neutrino Experiments

3.1 Weak interactions

After the firm establishment of the existence of neutrinos (see sections 2.1 and 2.2) and the development of the first "neutrino beam" [Dan62], neutrino experiments became the best means to probe the weak interactions. It is only with with the advent of high-energy particle accelerators, the $Sp\bar{p}S$ and later the $Tevatron$, SLC and LEP, capable of producing the weak vector bosons on shell, that this situation changed (although, as we will see, neutrino experiments still contribute). A rather complete overview of the achievements of this "period" is given in reference [Win91]. We will only discuss some of the latest results.

3.1.1 Neutral Current Couplings

The CHARM II Collaboration has studied neutrino-electron interactions [Vil94] in order to determine the vector and axial-vector electron-Z couplings. The cross sections are given by

$$\frac{d\sigma_{\overline{\nu}}^{\nu}}{dy} = \frac{G_F^2 s}{4\pi}\left[(g_V \pm g_A)^2 + (g_V \mp g_A)^2 (1-y)^2 + (2 + g_V + g_A)^2\right] \tag{3.1}$$

where $s = 2m_e E_\nu, y = E_e/E_\nu$ and g_V and g_A are the vector and axial vector couplings described in equations (2.19) and (2.20). The last term $(2 + g_V + g_A)^2$ arises from charged current-neutral current interference and is only present for ν_e-induced events. From the simultaneous measurement of $d\sigma/dy$ for $\nu_\mu e$ and $\overline{\nu_\mu} e$ and for $\nu_e e$ and $\overline{\nu_e} e$ the CHARM II Collaboration derived g_V and g_A with a two-fold sign ambiguity (because of the quadratic dependence). When combining this measurement with forward-backward asymmetry results from LEP (which also suffer from a two-fold ambiguity), a unique solution is found as can be seen in figure 3.1. Only the combination of **all** the data allows to determine that the electron is the down component of the $SU(2)_L$ doublet.

3.1.2 $sin^2\theta_W$ and the W mass

The ratio of neutral current and charged current deep inelastic neutrino-nucleon scattering can be used to measure the electroweak mixing parameter $sin^2\theta_W$. The results are not as precise as the LEP results [LEP96], but they are extracted from a completely different dataset. Furthermore, in a very recent publication [McF97], the CCFR Collaboration

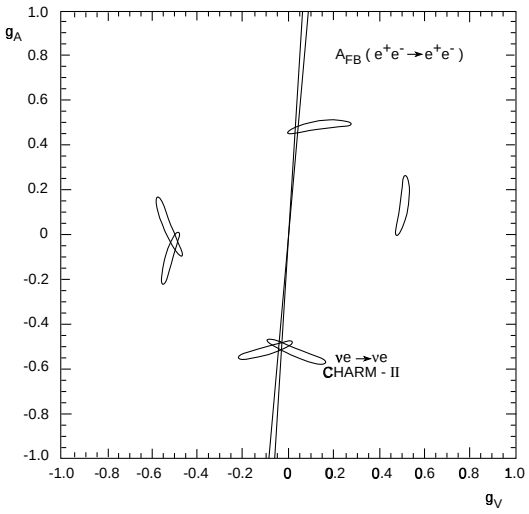

Figure 3.1: g_A^e and g_V^e determined from $\nu_\mu e$,$\overline{\nu_\mu} e$, $\nu_e e$ and $\overline{\nu_e} e$ scattering and from e^+e^- forward-backward asymmetry at LEP. Combining the results all the ambiguities are resolved and only one solution, compatible with the Standard Model, remains.

extracts $sin^2\theta_W$ from the data in a way which is nearly independent of m_{top} and m_{Higgs}. They find

$$sin^2\theta_W^{(on-shell)} = 0.2236 \pm 0.0028(expt) \pm 0.0030(model) \tag{3.2}$$

where (on-shell) indicates the extraction method used. The experimental systematics are dominated by the uncertainty on the ν_e contamination of the beam and the model-dependent systematics are dominated by heavy quark (charm and strange) corrections. The result implies $M_W = 80.35 \pm 0.21\ GeV$, which agrees and is competitive with direct mass measurements. With their 96-98 run using an improved beam line they expect to be able to reduce the error on M_W to about 100 MeV.

3.2 Strong Interactions: a Measurement of α_S

The differential cross-sections for neutrino-nucleon deep inelastic charged-current scattering can be written in term of the structure functions F_1, F_2 and F_3 as follows [Okun82]:

$$\begin{aligned}\frac{d\sigma^{\nu,\overline{\nu}}}{dx\ dy} &= \frac{G_F^2 M E_\nu}{\pi}\left[\frac{y^2}{2} 2xF_1\left(x,Q^2\right)\right. \\ &\left. + \left(1 - y - \frac{Mxy}{2E_\nu}\right) F_2\left(x,Q^2\right) \pm y\left(1-\frac{y}{2}\right) xF_3\left(x,Q^2\right)\right]\end{aligned} \tag{3.3}$$

where G_F is the Fermi coupling constant, M is the nucleon mass, E_ν is the incoming neutrino energy, x and y are the usual scaling variables and Q^2 is the transfered four-momentum squared. F_1 can be expressed in terms of F_2 using the Callan-Gross relation but taking into

	Solar	Atmospheric	Reactor	Accelerator
$E(MeV)$	≤ 14	10^3	≤ 10	$30 - 10^5$
$L(m)$	10^{11}	$10^4 - 10^7$	$10 - 300$	$10^2 - 10^5$
$\Delta m^2\ (eV^2)$	10^{-11}	10^{-4}	10^{-2}	$10^{-2} - 10^{-1}$

Table 3.1: Values of E (typical neutrino energy), L (baseline) and Δm^2 maximal sensitivity for the 4 types of neutrino oscillation experiments. The accelerator experiments include the proposed long baseline projects.

account scaling violation:

$$2xF_1\left(x,Q^2\right) = F_2\left(x,Q^2\right)\ \frac{1+4M^2x^2/Q^2}{1+R(x,Q^2)} \tag{3.4}$$

Here $R = \frac{\sigma_L}{\sigma_T}$ is the ratio of the cross-section of longitudinally to transversely polarized W-bosons.

Neutrino experiments can measure these cross-sections and extract the values of F_2 and xF_3 for various values of x and Q^2. The dependence of the structure functions on these variables (the so-called scaling violation) can then be compared with the QCD prediction to determine α_S (see for example [Hal84]).

The CCFR Collaboration has recently published [Sel97] the results of their latest analysis which yields

$$\alpha_S\left(M_Z^2\right) = 0.119 \pm 0.002(exp.) \pm 0.004(theory) \tag{3.5}$$

Note that the precision of this result is comparable with the results obtained by LEP [LEP96].

3.3 Neutrino Oscillations

Today, neutrino physicists, as they are sometimes called, have shifted their main focus to the question of neutrino masses. We have seen in section 2.4 that there is a lot of activity on direct mass measurements from kinematics, so we will not repeat this here, but many experiments probe neutrino masses by searching for oscillations. Solar, atmospheric, reactor and accelerator neutrinos have completely different values of L/E (see section 2.5) and thus allow to probe largely different values of Δm^2. Table 3.1 lists the typical E and L values and Δm^2 sensitivities reached (or in reach). Note that experiments study different neutrino flavors and use different oscillation detection techniques: disappearance, which consists of observing a reduction in flux of a certain neutrino flavor in a "beam", or appearance, which consists of searching for a specific neutrino flavor in a neutrino beam of a different flavor.

3.3.1 Solar Neutrinos

We believe the sun is a gravitationally stabilized thermonuclear fusion reactor. Of all the reactions occurring, eight contribute significantly to produce an intense neutrino flux [Bah89]. The measurement of solar neutrinos yields valuable information about the solar interior since neutrinos should be able to escape the sun relatively easy.

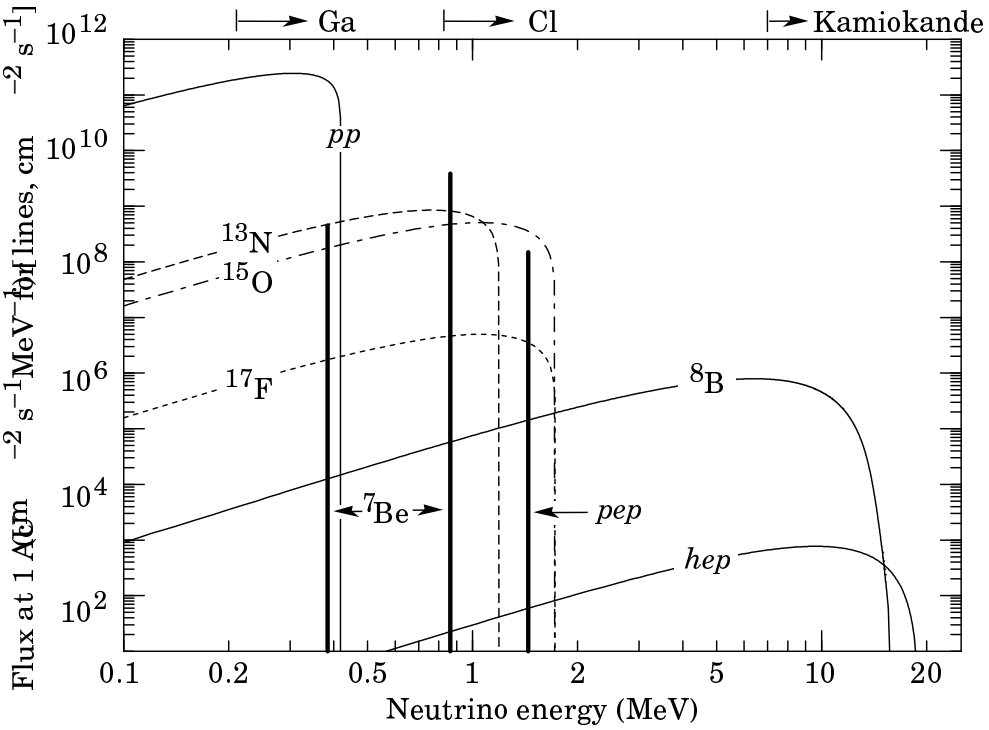

Figure 3.2: Solar neutrino spectra according to Bahcall and Pinsonneault [Bah95] (the plot is from [PDG96]). The neutrino fluxes from continuum sources are given in units of number per cm^2 per second per MeV at one astronomical unit. The neutrino lines are given in number per cm^2 per second. The arrows at the top indicate the energy thresholds for the various types of running experiments. The higher-energy ^7Be line is just above threshold for the chlorine experiment. Spectra from the pp chain are shown in solid lines while spectra from the CNO chain are displayed in dashed lines.

The main neutrino-producing reactions in the proton-proton chain are

$$p + p \rightarrow {}^2H + e^+ + \nu_e \qquad (E_\nu \leq 0.420\ MeV) \tag{3.6}$$
$$p + e^- + p \rightarrow {}^2H + \nu_e \qquad (E_\nu = 1.442\ MeV) \tag{3.7}$$
$$^3He + p \rightarrow {}^4He + \nu_e \qquad (E_\nu \leq 18.773\ MeV) \tag{3.8}$$
$$^7Be + e^- \rightarrow {}^7Li + \nu_e \qquad (E_\nu = 0.862\ MeV, 89.7\%; E_\nu = 0.384\ MeV, 10.3\%) \tag{3.9}$$
$$^8B \rightarrow {}^7Be^* + e^+ + \nu_e \qquad (E_\nu \leq 15\ MeV) \tag{3.10}$$

The neutrinos from the *pp* (3.6), *hep* (3.8) and ^8B (3.10) reactions have a continuous energy spectrum (the maximum energy is shown in parentheses), while the *pep* (3.7) and ^7Be (3.9) neutrinos have well-defined energies. They are known as neutrino lines. The spectra and fluxes of neutrinos from reactions (3.6) to (3.10) are shown in figure 3.2. The *pp* neutrinos are by far the most abundant, but they have low energies and are difficult to detect. The ^8B and *hep* neutrinos have much higher energy, but they are scarce and the *hep* neutrino flux is orders of magnitude lower than the already small ^8B flux.

Three reactions in the CNO cycle produce relatively abundant neutrinos:

$$^{13}N \rightarrow \ ^{13}C + e^+ + \nu_e \qquad (E_\nu \leq 1.199\ MeV) \tag{3.11}$$
$$^{15}O \rightarrow \ ^{15}N + e^+ + \nu_e \qquad (E_\nu \leq 1.732\ MeV) \tag{3.12}$$
$$^{17}F \rightarrow \ ^{17}O + e^+ + \nu_e \qquad (E_\nu \leq 1.740\ MeV) \tag{3.13}$$

Although these reactions are of great interest since they provide information about the CNO cycle, the fluxes and energies are low, making them very hard to detect (see figure 3.2).

The predicted fluxes are obtained by integrating the production rates over the volume (or rather mass) of the sun. These rates are sensitive functions of temperature, density and chemical composition. We give some uncertainties from reference [Bah89] here, but these should be interpreted as a rough indication rather than exact values.

- The *pp* flux is produced in essentially the same region as the photon luminosity flux, it is not too sensitive to temperature and is estimated to be known to about 2 %. Furthermore, the calculated flux is approximatively model-independent because it is so closely linked to the solar luminosity.

- The ^8B flux on the other hand is extremely temperature dependent ($\phi(^8B) \propto T^\alpha$ with $\alpha \approx 18$). Because of this, 75 % of the flux is produced in the inner 2 % of the sun. The uncertainty is large (37 %) due to limited knowledge of the low-energy nuclear production cross-section and the influence of heavy element abundance in the solar interior.

- The ^7Be flux is also strongly temperature dependent, although less than the ^8B flux: $\phi(^7Be) \propto T^8$. The uncertainty on the flux is of the order of 15 %.

- The uncertainty on the *pep* flux is supposed to be of the order of 5%, while the CNO neutrino fluxes suffer from uncertainties of the order of 50 %.

3.3.2 Solar Neutrino Experiments

All the solar neutrino experiments are located deep underground to reduce the charged-particle background. A short description of each of them is given now:

- Homestake

  The first observation and measurement of the solar neutrino flux started in 1970 using a chlorine detector in the Homestake Gold Mine. The detector is a single tank containing 615 tons of tetrachloroethylene, in which electron neutrinos of at least 814 keV can produce ^{37}Ar atoms through the reaction

  $$^{37}Cl(\nu_e, e^-)^{37}Ar \tag{3.14}$$

  After each datataking run the produced argon is extracted and counted in a very small proportional counter. Since the extraction procedure is slow (of the order of a day), no short term effects like day-night variations can be observed. The signal in the proportional counter is generated by the 2.82 keV Auger electrons emitted by the ^{37}Ar (the half life is 35.04 days).

From 1970 to 1995, 108 datataking runs were performed with the Homestake detector, yielding [Cle96] a combined result (after subtracting the background) of

$$\phi_{SNU}^{Homestake} = 2.54 \pm 0.14(stat) \pm 0.14(syst)\ SNU \tag{3.15}$$

One Solar Neutrino Unit $(SNU) = 10^{-36}$ captures per atom per second. From figure 3.2 we see that the chlorine experiment is sensitive to more than one source of neutrinos, which makes it impossible to translate the flux in SNUs to a flux in neutrinos without making assumptions. Supposing the entire Homestake signal is due to the ^8B neutrinos, then by dividing the flux in SNUs by the total cross-section expected from the ^8B neutrino spectrum, we get

$$\phi_{\nu_e}^{Homestake} = 2.23 \pm 0.22\ 10^6 \nu_e/cm^2 \tag{3.16}$$

Note that the precision limit for the chlorine detector is set by the uncertainty on the cross-section (3.14), which is 4 %.

- Sage

In the early nineties, two experiments sensitive to the *pp* reaction (3.6) started data taking. The reaction

$$^{71}Ga(\nu_e, e^-)^{71}Ge \tag{3.17}$$

has a Q-value of only 233 keV, providing at present the only feasible means to measure low-energy solar neutrinos. The first of the two experiments is the Soviet(now Russian)-American Gallium solar neutrino Experiment (SAGE). In SAGE, the gallium target is kept liquid (the melting point is at 29.8^oC) and each measurement is started by mixing 700 μg of natural Ge carrier in each 7 t module. After about 4 weeks, the Ge carrier and any Ge atoms produced by solar neutrinos are chemically extracted from the gallium using a complicated procedure [Abd94]. The counting procedure uses a small proportional counter. The difficulty of the experiment is striking from the numbers: the Standard Solar Model (SSM) predicts a production rate of 1.2 ^{71}Ge atoms per day in 30 t of Ga! Therefore, taking into account the one-day delay between the end of the exposure and the start of counting (the ^{71}Ge half-life is 11.4 days), as well as the chemical extraction and counting efficiencies, only about 4 atoms are expected to be detected after a 4-week exposure of 30 t of gallium.

From January 1990 on, monthly extractions were made to measure the solar flux with the 30 t of purified gallium produced. In September 1991 the total target mass was increased to 57 t. A new analysis method with pulse-shape discrimination has also been developed, approximatively doubling the counting efficiency.

Just like GALLEX did (see below for a more extensive description), SAGE exposed the detector to an extremely active ^{51}Cr source which radiates neutrinos at energies similar to *pp* neutrinos. The ratio of measured over predicted signal was [Abd96a] $R = 0.95 \pm 0.11(stat)^{+0.05}_{-0.08}(syst)$.

For the combined 1990-1993 data, the best fit value using the new analysis [Abd96b] yields a capture rate of:

$$\phi_{SNU}^{SAGE} = 72\ ^{+12}_{-10}(stat)\ ^{+5}_{-7}(syst)\ SNU \tag{3.18}$$

- GALLEX

The GALLEX detector is located at the Gran Sasso Underground Laboratories, detecting solar neutrinos through reaction (3.17) in a 100-ton gallium chloride target solution. Counting of the produced ^{71}Ge atoms is performed after extraction, following every 3-4 week exposure.

As an additional check, the GALLEX Collaboration has exposed the detector to a (highly active) ^{51}Cr source of low-energy neutrinos. The neutrino spectrum emitted in ^{51}Cr decay consists of four mono-energetic lines between 426 and 746 keV, compatible with the solar spectrum. After a first exposure to such a source [Ans95] from June 23rd to October 10th 1994, the collaboration obtained a ratio of measured over expected counts of

$$R_{Summer\ 94} = 1.04 \pm 0.12 \tag{3.19}$$

Preliminary results from a second exposure performed between October 5th 1995 and February 13th 1996 indicate a ratio of

$$R_{Fall\ 95} = 0.83 \pm 0.10 \tag{3.20}$$

The results are statistically compatible with 1.

The GALLEX results for the solar neutrino flux from the data collected between May 1991 and October 1995 are the following [Ham96]:

$$\phi_{SNU}^{GALLEX}(14.05.91 - 29.04.92) = 83.4\ ^{+18.5}_{-19.5}\ SNU \tag{3.21}$$

$$\phi_{SNU}^{GALLEX}(19.08.92 - 22.06.94) = 75.9\ ^{+10.5}_{-10.7}\ SNU \tag{3.22}$$

$$\phi_{SNU}^{GALLEX}(12.10.94 - 04.10.95) = 53.9 \pm 11.0\ SNU \tag{3.23}$$

$$\phi_{SNU}^{GALLEX}(Combined) = 69.7\ ^{+7.8}_{-8.1}\ SNU \tag{3.24}$$

Statistical tests of the various datasets indicate they are all consistent with one distribution, with a mean value that has not significantly varied over the 5 years of operation. Note that no correction seems to have been applied to account for the result of the ^{51}Cr exposures.

- (Super-)Kamiokande

The new Super-Kamiokande (Super Kamioka Nucleon Decay Experiment) detector has started datataking in April 1996. It is the follow-up of Kamiokande which has stopped datataking in February 1995. We will describe the Super-Kamiokande detector rather than Kamiokande, but only preliminary results are available such that we will include the results from Kamiokande. Since Super-Kamiokande is essentially just a bigger, more efficient version of Kamiokande this approach is well justified.

Super-Kamiokande is a 50 kton imaging water Čerenkov detector (Kamiokande was just 4500 t) which detects solar neutrinos through the reactions (charged current and neutral current):

$$\nu + e^- \rightarrow \nu + e^- \tag{3.25}$$

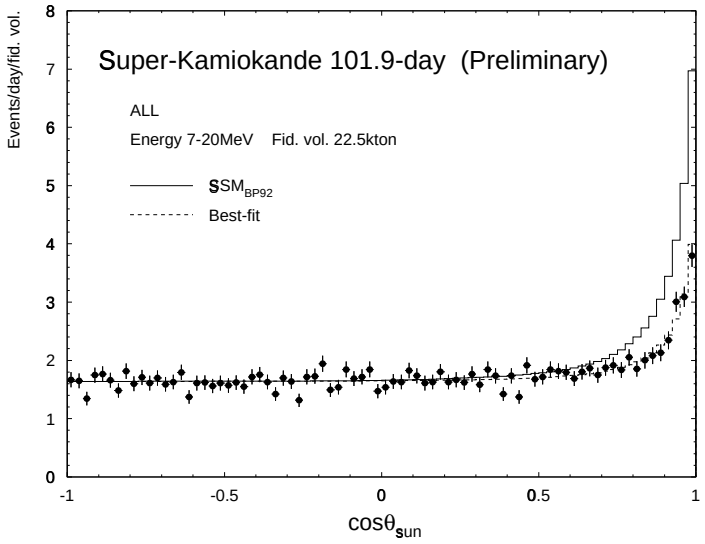

Figure 3.3: Distribution of $cos\theta_{sun}$ (preliminary) for the Super-Kamiokande May to October 1996 dataset. θ_{sun} is the angle between the direction of the sun and that of the scattered electron. The solid line corresponds to the Bahcall-Pinsonneault 92 Standard Solar Model [Bah92], while the dashed line is the best fit ($BP92 \times 0.441$). The sun can clearly be identified as the main neutrino source.

The detector identifies the Čerenkov light radiated by the recoiling electron in the water. The offline energy threshold for detection of solar neutrinos has gradually evolved from 9.3 MeV in January 1987 to 7.0 MeV from November 1991 on for Kamiokande. In Super-Kamiokande the threshold has been at 7.0 MeV since the start of datataking. This implies Super-Kamiokande can only detect ^8B neutrinos (see figure 3.2). We should note here that the triggering threshold is generally lower (5 MeV in the last phase of Kamiokande), but that for background reasons this threshold is raised at the analysis level. One major background source stems from radon contamination of the water, making water purification an essential component of detector operation.

For solar neutrinos, the fiducial volume used is 22.5 kton (680 tons in Kamiokande) to isolate from gamma rays and neutrons produced in the rock surrounding the detector. One big advantage of the (Super-)Kamiokande detection technique is that they are able to determine the direction of the electron with a reasonable degree of accuracy (26^o for 10 MeV electrons in Kamiokande). This is clearly visible in figure 3.3. Kamiokande is the first "neutrino telescope".

The observed flux [Fuk96a, Tak97] can be directly expressed in a neutrino flux since only ^8B neutrinos contribute:

$$\phi_{\nu_e}^{Kamiokande} = 2.80 \pm 0.19(stat) \pm 0.33(syst)\ 10^6 \nu_e/cm^2 \quad (3.26)$$

$$\phi_{\nu_e}^{Super-Kamiokande,pre.} = 2.51^{+0.14}_{-0.13}(stat) \pm 0.18(syst)\ 10^6 \nu_e/cm^2 \quad (3.27)$$

Experiment	Observed Flux	BP SSM Prediction	Ratio
Homestake	$2.54 \pm 0.14 \pm 0.14$ SNU	$9.3\ ^{+1.2}_{-1.4}$ SNU	0.273 ± 0.021
SAGE	$72\ ^{+12}_{-10}\ ^{+5}_{-7}$ SNU	$137\ ^{+8}_{-7}$ SNU	0.526 ± 0.089
GALLEX	$69.7 \pm 6.7\ ^{+3.9}_{-4.5}$ SNU	$137\ ^{+8}_{-7}$ SNU	0.509 ± 0.089
Kamiokande	$2.80 \pm 0.19 \pm 0.33$	$6.62\ ^{+0.93}_{-1.12}$	0.423 ± 0.058
Super-Kamiokande	$2.51\ ^{+0.14}_{-0.13} \pm 0.18$	$6.62\ ^{+0.93}_{-1.12}$	0.379 ± 0.034
Combined	2.586 ± 0.195	$6.62\ ^{+0.93}_{-1.12}$	0.391 ± 0.029

Table 3.2: Observed fluxes from the solar neutrino experiments along with the predictions from the Bahcall-Pinsonneault Standard Solar Model 95 [Bah95] and the ratio observed/predicted. The (Super-)Kamiokande data is expressed in units of $10^6 cm^{-2} sec^{-1}$.

Super-Kamiokande provides us with two more important results. First of all, they do not observe a significant day-night variation of the neutrino flux:

$$\phi^{Super-Kamiokande,pre.}_{\nu_e,day} = 2.30^{+0.18}_{-0.17}(stat) \pm 0.17(syst)\ 10^6 \nu_e/cm^2 \quad (3.28)$$

$$\phi^{Super-Kamiokande,pre.}_{\nu_e,night} = 2.75^{+0.21}_{-0.20}(stat) \pm 0.20(syst)\ 10^6 \nu_e/cm^2 \quad (3.29)$$

and second, the electron spectrum they observe corresponds to the expected one [Tak97].

Last but not least, the full Kamiokande [Fuk96a] data nearly covers a full solar cycle, such that they searched for a possible correlation between sunspot activity and neutrino flux. No correlation could be found.

3.3.3 Discussion on the Solar Neutrino Results

Table 3.2 summarizes the results from the various experiments and compares with the rates predicted by the Bahcall-Pinsonneault 95 Standard Solar Model [Bah95]. We observe that there seems to be a significant discrepancy between the observed and expected rates. The fact that four different experiments based on three different techniques all disagree with predictions appears to exclude an experimental source to the discrepancy. Now if we suppose that all experiments are about right and the predictions are correct, some simple conclusions can be derived:

- The Kamiokande experiments are only sensitive to the ^8B flux, which seems to be low by approximatively a factor two.
- The flux observed in Homestake, if interpreted as coming exclusively from ^8B neutrinos, is compatible with the Kamiokande results. This would mean that the ^7Be neutrinos are essentially not there.
- In the predictions for the gallium experiments, about 73 SNUs are expected from *pp* and *pep* neutrinos. But using the rate observed in Kamiokande, we can say 7 SNUs come from the ^8B neutrinos. This again doesn't leave any room for ^7Be neutrinos.

Let us discuss some possible solutions.

Standard Solar Models

The sun is an extremely complex system and it should be clear that solar models, as complex as they have become, are still a much simplified image of the real thing. Could it be that alternative solar models would predict neutrino fluxes compatible with experiment while respecting the boundary constraints imposed by the sun's luminosity, age, surface temperature, ... ?

In 1994 for example, A. Dar and G. Shaviv [Dar94] argued that they had developed an improved model which is consistent within theoretical and experimental uncertainties with observations after 1986. They decided to exclude the pre-1987 Homestake data because after the installation of new pumps in 1986 the Homestake data is in better agreement with the Kamiokande data. Their model was published in detail in 1996 [Dar96].

We will see below that the data, if correct, cannot be compatible with any solar model without the introduction of new neutrino physics. But in the meantime it is nevertheless important to note that the solar models neglect potentially important factors [Dar97] like differential rotation, magnetic field, angular momentum effects,... and do not explain among others solar activity and the surface depletion of lithium, beryllium and boron relative to their meteoritic values. We do not know if these effects are related to the solar neutrino problem though.

N. Hata and P. Langacker have been investigating the compatibility of solar models with observation (and observations with each other) for a few years now [Hat93, Hat94, Hat95] and could already show that this compatibility was only at the few % level. In their latest analysis [Hat97], they use the most recent available data, including the new Super-Kamiokande result and the significant increase in statistics obtained by the gallium experiments. The constraints on the ^7Be and ^8B fluxes that can be extracted from the data are clearly visible in figure 3.4, where fluxes have been normalized to the BP 95 SSM values ($\phi(Be)_{SSM} = 5.15\ 10^9 cm^{-2}s^{-1}, \phi(B)_{SSM} = 6.62\ 10^6 cm^{-2}s^{-1}$). They proceed by performing a model independent best fit to the data using *pp*, ^7Be, ^8B and CNO fluxes as free parameters but keeping some minimal assumptions on the solar luminosity, the beta spectrum shape and the detector cross sections. As can be seen in figure 3.5, the best fit combining all observations is in the non-physical region $\phi(Be)/\phi(Be)_{SSM} = -0.6 \pm 0.4$ and $\phi(B)/\phi(B)_{SSM} = 0.4 \pm 0.05$. Imposing that the fluxes be in physical parameter space, i.e. larger than 0, the result is

$$\phi(Be)/\phi(Be)_{SSM} < 0.1 \textit{ and } \phi(B)/\phi(B)_{SSM} = 0.38 \pm 0.05 \tag{3.30}$$

with $\chi^2_{min} = 9.2$. χ^2_{min} is the χ^2 of the fit for the best fit values, but the number of degrees of freedom (DOF) is zero. To try to determine what this actually means in terms of quality of the fit, N. Hata and P. Langacker decided to do the following: 1) take the central value of the (physical) fit, 2) calculate the solar neutrino rates for each of the experiments, 3) generate Monte Carlo distributions for each of the experiments using the experimental uncertainties and 4) for each Monte Carlo dataset obtained, apply the model-independent analysis and find the χ^2_{min}. The fraction of these Monte Carlo "experiments" that have $\chi^2_{min} > 9.2$ corresponds to the probability that the original best fit values (3.30) are really the solar neutrino fluxes. Only 0.6 % of the Monte Carlo experiments have $\chi^2_{min} > 9.2$, which means that their model-independent analysis excludes the best fit astrophysical solution at 99.4 % C.L.. Dropping one of the constraints (Homestake data, water Čerenkov data, gallium data or solar luminosity) does not help much: the best result still excludes the astrophysical solution at 98.3 % C.L..

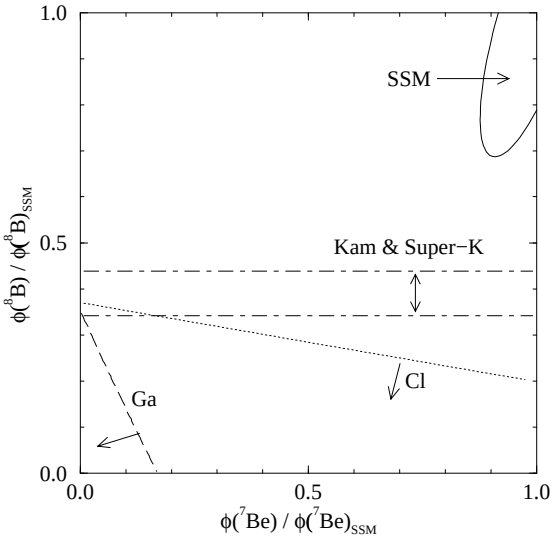

Figure 3.4: Constraints on the ^7Be and ^8B fluxes at 90 % C.L. from the Homestake result (below the dotted line), the combined Kamiokande and Super-Kamiokande results (between the dash-dotted lines) and the combined GALLEX and SAGE results (below the dashed line). The fluxes have been normalized to the BP 95 SSM as given in the text and the 90 % C.L. SSM range is contained in the solid line.

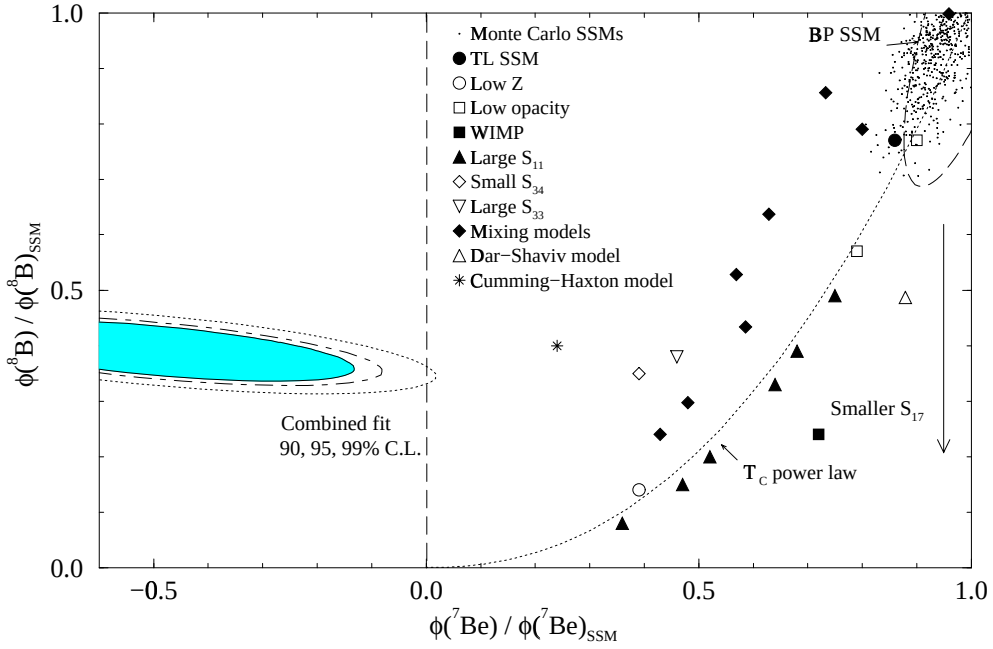

Figure 3.5: Best fit to the observed neutrino fluxes keeping only a minimal set of assumptions (see text) as performed by N. Hata and P. Langacker [Hat97]. A number of solar models are shown: the BP 95 SSM [Bah95] at 90 % C.L., the core temperature power law, a set of non-standard models of which the Dar and Shaviv model and the recent Cummings and Haxton ^3He diffusion model [Cu96].

Summarizing, N. Hata and P. Langacker's **model-independent** analysis shows that it is highly unlikely that the results from the 3, or even 2 out of 3 types of solar neutrino experiments are compatible with each other without adding at least one additional parameter to the mix. However, from their analysis it could be due to any of the following three factors:

- underestimation of the experimental errors by at least two types of experiments,
- wrong results from the chlorine and gallium experiments due to wrong neutrino absorption cross-section estimates (the second ^{51}Cr test performed by GALLEX revives this a possibility). This would make observations compatible with for example the Dar and Shaviv solar model [Dar96],
- non-Standard (Electroweak) Model properties of neutrinos.

Let us explore the last possibility.

Neutrino Oscillations in Vacuum

We have elaborated on the theoretical aspects of neutrino oscillations in vacuum in section 2.5 where equation (2.49) clearly demonstrates that neutrino oscillations are energy-dependent. Oscillations of the solar electron neutrinos between the sun and the detection point on earth would lead to a suppression of the observed neutrino flux since they are mostly detected through charged-current interactions. From the flux suppressions observed and using the compatibility between the spectrum observed by Kamiokande and the predicted spectrum, allowed regions in the $\Delta m^2 - sin^2 2\theta$ plane can be computed for any solar model. For the BP 95 SSM only a few regions remain possible in the simple two-flavor model [Hat97]. As can be seen in figure 3.6, they are all contained in the narrow range $\Delta m^2 = (5-8)\ 10^{-11} eV^2$ and $sin^2 2\theta = 0.65 - 1$ (the parameters apply to oscillations of electron neutrinos to any other neutrino). The large values required for the mixing angle make this solution rather unattractive, but there is no solid reason to reject it.

Neutrino Oscillations in Matter: the MSW Effect

L. Wolfenstein observed in 1978 [Wol78] that *"the effect of coherent forward scattering must be taken into account when considering the oscillations of neutrinos travelling through matter"*. In fact, he discovered that in general if there exists an interaction through which neutrinos can change flavor (this could be neutrino oscillations, but also a flavor changing neutral current component for example), this flavor change can be enhanced or even only possible if the neutrinos travel through matter. The latter is clear in the case of massless neutrinos but with off-diagonal neutral current interactions (connecting different neutrino flavors): there are no "oscillations" in vacuum but in matter neutrinos can change flavor.

In 1984, S.P. Mikheev and A. Yu. Smirnov [Mik85] noticed that for specific oscillation and matter density parameters, this enhancement could develop a resonance behavior.

We will treat here the two-neutrino case for clarity. T.K. Kuo and J. Pantaleone have shown [Kuo87] that in most cases the three-neutrino formalism can be reduced to a two-neutrino-like situation with two resonances instead of one.

Neutrino propagation through matter differentiates neutrino flavors because matter is nearly exclusively composed of first generation leptons and quarks. This singles out the

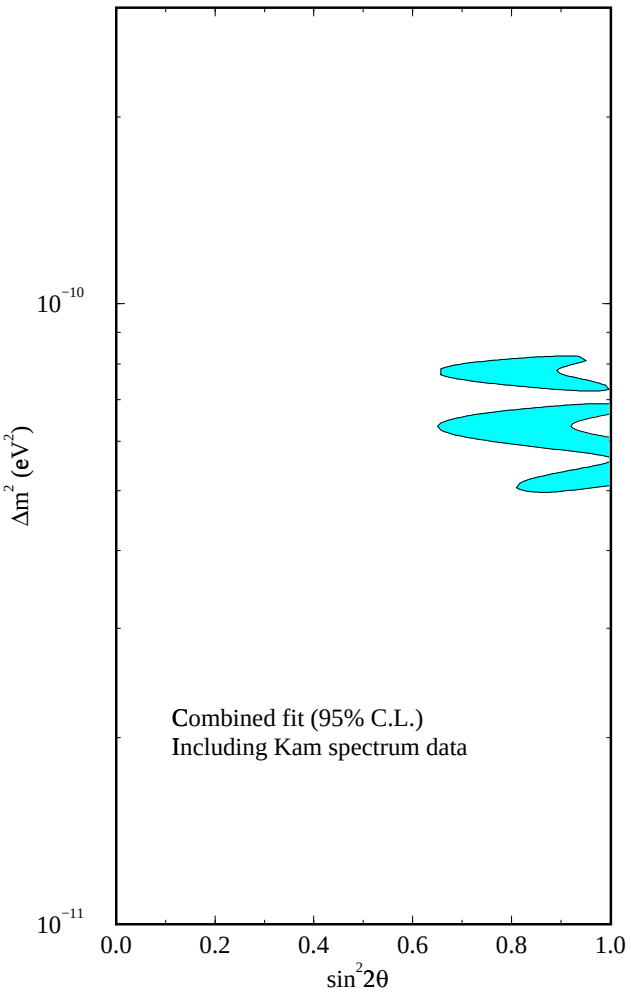

Figure 3.6: Allowed regions for two-flavor neutrino oscillations in vacuum compatible with all solar neutrino observations [Hat97]. The constraint generated by the compatibility between the spectrum observed by Kamiokande and the predicted spectrum is included. The plot applies to $\nu_e \leftrightarrow \nu_x$ oscillations with $x =$ anything.

electron neutrino, which can propagate while having charged-current interactions with electrons in addition to the neutral-current interactions. Let us consider the potential energy the electron neutrino acquires due to these charged-current interactions. For the energies we are considering, and supposing the sun is unpolarized and at rest, it can be written as

$$V_{\nu_e} = \sqrt{2} G_F N_e \tag{3.31}$$

with N_e the electron density. In the two-neutrino mixing case[1]

$$\begin{pmatrix} \nu_e \\ \nu_\alpha \end{pmatrix} = R_\theta \begin{pmatrix} \nu_1 \\ \nu_2 \end{pmatrix} \ , \ with R_\theta = \begin{pmatrix} cos\theta & sin\theta \\ -sin\theta & cos\theta \end{pmatrix} \tag{3.32}$$

($\alpha = \mu$ or τ), the evolution of flavor content as a function of propagation can be described by [Gel95]

$$i\frac{d}{dx}\begin{pmatrix} \nu_e \\ \nu_\alpha \end{pmatrix} = \frac{1}{2E}\mathbf{M}^2 \begin{pmatrix} \nu_e \\ \nu_\alpha \end{pmatrix} \tag{3.33}$$

The matrix $\mathbf{M}^2$ can be written

$$\mathbf{M}^2 = \frac{1}{2}\left[R_\theta \begin{pmatrix} -\Delta m^2 & 0 \\ 0 & \Delta m^2 \end{pmatrix} R_\theta^T + 2E \begin{pmatrix} \sqrt{2} G_F N_e & 0 \\ 0 & -\sqrt{2} G_F N_e \end{pmatrix} \right] \tag{3.34}$$

where the first term on the right-hand side is the usual vacuum oscillations term (see equation (2.44)) while the second term is the one due to $\nu_e - e$ charged-current scattering. Note that we have subtracted a piece proportional to the identity matrix so that $\mathbf{M}^2$ appears in a more symmetric form.

We are now ready to define the matter eigenstates

$$\begin{pmatrix} \nu_{1m} \\ \nu_{2m} \end{pmatrix} = R_{\theta_m}^T \begin{pmatrix} \nu_e \\ \nu_\alpha \end{pmatrix} \tag{3.35}$$

which we obtain by diagonalizing $\mathbf{M}^2$:

$$R_{\theta_m}^T \mathbf{M}^2 R_{\theta_m} = \frac{1}{2}\begin{pmatrix} -\Delta_m & 0 \\ 0 & \Delta_m \end{pmatrix} \tag{3.36}$$

In this equation $\Delta_m = \Delta m^2 \sqrt{(a - cos2\theta)^2 + sin^2 2\theta}$ with $a = 2\sqrt{2} E G_F N_e / \Delta m^2$. The newly defined matter mixing angle θ_m appearing in R_{θ_m} is such that

$$sin^2 2\theta_m = \frac{sin^2 2\theta}{(cos2\theta - a)^2 + sin^2 2\theta} \tag{3.37}$$

and we see immediately that even if the vacuum mixing angle is very small, we will have maximal mixing in matter if the condition $a = cos2\theta$ is satisfied. Figure 3.7 shows the value of $sin^2 2\theta_m$ as a function of a for three different vacuum mixing angles. The resonance is the so-called MSW effect.

Combining the solar neutrino data with one of the solar models (for the predicted neutrino flux *and* the evolution of the electron density in the sun), oscillation parameters can be computed taking into account the MSW effect[2]. Such a calculation has been made for the most recent results and the latest Bahcall-Pinsonneault solar model [Bah95] by N. Hata and P. Langacker [Hat97]. The allowed regions are shown in figure 3.8.

[1] Here the neutrino with which the electron neutrino mixes is supposed to be active (i.e. ν_μ or ν_τ). If it is a sterile neutrino, we have to take into account the difference in neutral-current interactions as well.

[2] We have not discussed the difference between adiabatic and non-adiabatic regimes. These depend on the width of the resonance and the rate of change of the electron density, see for example [Mik85].

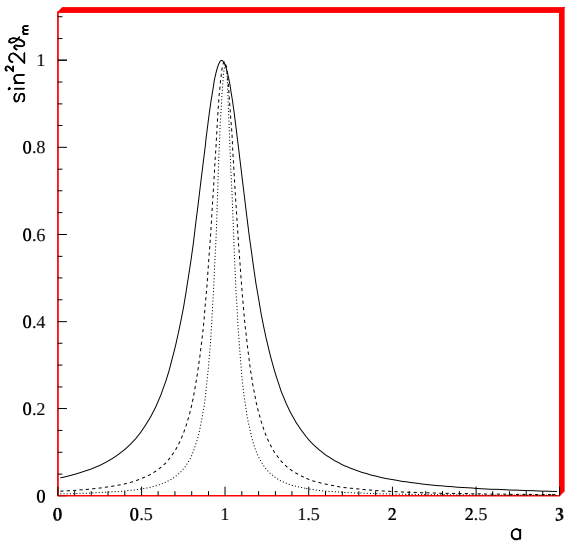

Figure 3.7: $sin^2 2\theta_m$ as a function of $a = 2\sqrt{2}EG_F N_e/\Delta m^2$ for three different values of the vacuum mixing angle: $sin^2 2\theta = 4\ 10^{-2}$ (solid line), $sin^2 2\theta = 1\ 10^{-2}$ (dashed line) and $sin^2 2\theta = 4\ 10^{-3}$ (dotted line).

Conclusions

We have seen that three different types of experiments with sensitivities in different energy regions all observe a solar neutrino deficit. Furthermore, even though solar models are evolving very fast and an exact quantification of the deficit is probably hazardous, the solar data does not seem to be compatible unless we invoke some non-Standard (Electroweak) Model physics, or at least two experiments are wrong.

On the other hand, the vacuum neutrino oscillation solutions all require a large mixing angle, a rather unattractive feature. The very elegant MSW mechanism does not require this though. As John Bahcall said, *"it would be a disgrace if Nature failed to make use of this marvellous possibility"* [Bah97]. This solution, which seems to prefer a Δm^2 value around $10^{-5} eV^2$, leads to a rather striking agreement with cosmological mixed dark matter and the seesaw mechanism if interpreted as due to $\nu_e \leftrightarrow \nu_\mu$ oscillations.

But we should not get carried away based on models only, beautiful as they may be. Future experiments, like SNO [Him96] which will be able to detect neutrinos through neutral-current interactions, and BOREXINO [Gia96] which will provide more information on the intermediate energy ^7Be neutrinos, will probably allow us to make another solid step forward in solving the solar neutrino crisis.

3.3.4 Atmospheric Neutrinos

Cosmic rays interact in the atmosphere to produce mainly pions and kaons. As these decay, a relative large flux of neutrinos between $< 100\ MeV$ and $10^4\ GeV$ is produced. Around $1\ GeV$, where the product of flux and neutrino charged-current interaction cross-section reaches a maximum, the neutrino flux is about $1\ cm^{-2}s^{-1}$ [Gai90].

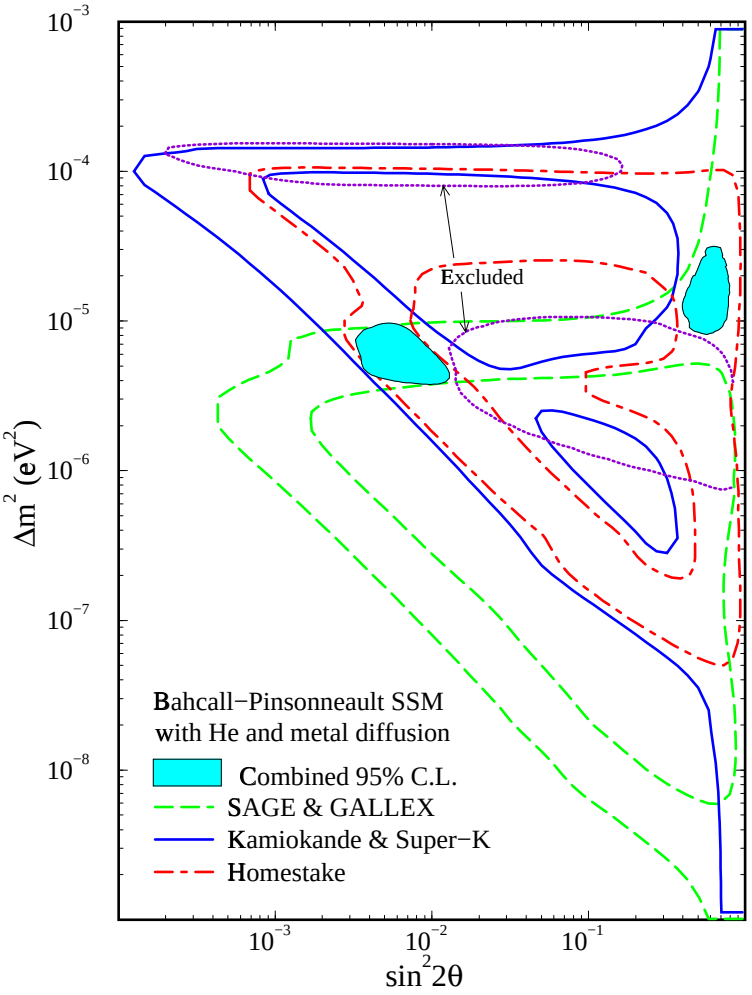

Figure 3.8: Oscillation [Hat97] parameter space (shaded areas) allowed by the solar neutrino observations at 95 % C.L. assuming the Bahcall-Pinsonneault 95 Standard Solar Model [Bah95] and taking into account matter effects (MSW). The allowed regions are also shown for the individual experiments: Homestake (dot-dashed line), Kamiokande and Super-Kamiokande combined (solid line), SAGE and GALLEX combined (dashed line), as well as regions excluded by the Kamiokande ^8B spectrum and day-night observations (dotted lines).

The decay sequence from pions is

$$\begin{array}{rcl} \pi^{\pm} & \rightarrow & \mu^{\pm} + \nu_{\mu}\,(\overline{\nu_{\mu}}) \\ & & \searrow \\ & & \quad e^{\pm} + \nu_e\,(\overline{\nu_e}) + \overline{\nu_{\mu}}\,(\nu_{\mu}) \end{array} \tag{3.38}$$

This is also the dominant decay sequence from kaons with most of the other kaon decays producing charged pions anyway. Supposing all the pions and muons decay we then expect to observe about two muon-like (muon or anti-muon) neutrinos for each electron-like neutrino and the ratio $\nu_e/\overline{\nu_e}$ should be close to the ratio μ^+/μ^-.

However, the full picture is a bit more complicated (see for example [Gai90]):

- above 2.5 GeV the muon decay length is longer than the typical production height,
- muon energy loss in the atmosphere implies that a 1 GeV muon had about 3 GeV at production. But most ν_e's originate from muon decays high in the atmosphere, which implies an offset in the spectrum of the $\nu_e/\overline{\nu_e}$ ratio with respect to the μ^+/μ^- ratio,
- the decay kinematics influence the energy spectra of the decay products and have to be taken into account,
- the geomagnetic field tends to prevent low energy cosmic rays from entering the atmosphere (this is the so-called geomagnetic cutoff), but this effect depends on the location on the Earth and the direction of the nuclei,
- the cosmic ray flux varies with the solar cycle.

We see that the only practical way of taking into account all these effects is to make a detailed Monte-Carlo simulation.

Still, uncertainties in the pion yield from interactions of cosmic rays with the atmosphere[3], assumptions about the primary cosmic ray spectrum and the treatment of the geomagnetic field lead to significant differences in the absolute rates and the neutrino energy spectra between various simulations [Gai96a]. But luckily, all of these difficulties do not affect the ratio of muon-like to electron-like neutrinos which is controlled by relatively well-known branching ratios and kinematics. And indeed the neutrino flavor ratio is the same within 2 % for all the simulations considered in [Gai96b]. A theoretical error of 5 % is usually assumed for the ratio.

In this context, the most powerful tool to search for anomalies in the atmospheric neutrino fluxes is to study the angular dependence of the ratio of muon-like to electron-like neutrinos.

3.3.5 Atmospheric Neutrino Experiments

To be able to compare between the various experiments while taking into account the different detection efficiencies, the experimental results are expressed as a "ratio of ratios":

$$R_{atm} = \frac{(\nu_{\mu} + \overline{\nu_{\mu}}/\nu_e + \overline{\nu_e})_{Data}}{(\nu_{\mu} + \overline{\nu_{\mu}}/\nu_e + \overline{\nu_e})_{MC}} \tag{3.39}$$

[3]Results from the SPY experiment [Amb96] may enhance the knowledge of these numbers.

- Fréjus

  The Fréjus detector, located near the center of the Fréjus tunnel in South-East France, was a high-resolution iron calorimeter of 900 ton mass. Datataking started in February 1984 with a mass of 240 ton and ended in September 1988. The detector mass had been gradually upgraded to reach 900 ton in June 1985. The total exposure corresponds to 2.0 kton-year.

  The trigger requirements imposed a threshold of about 200 MeV in electromagnetic energy. This led to an average trigger rate of about 45 events per hour, of which half were due to atmospheric muons while the rest was induced by local radioactivity and electronic noise. Atmospheric neutrinos produced about one event per week.

  The total data sample consists of 216 events. The events are fully compatible with neutrino interactions and do not resemble for example neutrons coming from the surrounding rock. After classification into electron-like, muon-like and neutral-current like events [Ber89], the result obtained is [Dau95]:

$$R_{atm}^{Fréjus} = 1.00 \pm 0.15(stat.) \pm 0.08(syst) \tag{3.40}$$

  which is in excellent agreement with the theoretical prediction.

  Note that the Fréjus experiment does not restrict its analysis to quasi-elastic events like the other experiments do.

- Soudan 2

  Soudan 2 is also a tracking calorimeter. Its total mass is 963 tons, mainly provided by corrugated steel. The data considered in the most recent published analysis [All97] have been collected between April 1989 and December 1993, corresponding to an exposure of 1.52 kton-year.

  The analysis method has been chosen to emulate the analysis used for the water Čerenkov detectors (see below), such that only single track (muon) and single shower (electron) events are used. A future analysis using the track reconstruction and separation properties of the detector is foreseen.

  After correcting for the background produced by photons and neutrons originating in the rock around the detector, 86.4 events are kept, yielding the result

$$R_{atm}^{Soudan2} = 0.72 \pm 0.19(stat.)\ ^{+0.05}_{-0.07}(syst) \tag{3.41}$$

  A new result has been presented at the 1997 EPS conference [Nak97] for a total exposure of 2.83 kton-year:

$$R_{atm}^{Soudan2} = 0.61 \pm 0.14(stat.)\ ^{+0.05}_{-0.07}(syst) \tag{3.42}$$

- IMB

  The IMB detector is an 8 kton water Čerenkov detector located in the Morton Salt Mine near Cleveland, Ohio. For the atmospheric neutrino study, data collected from

May 1986 to March 1991 was considered, using a fiducial volume of 3.3 kton for a total exposure of 7.7 kton-year.

The event selection threshold is about 50 MeV (70 photomultiplier tubes to be precise). Analysis of the geometry and intensity of the Čerenkov hit pattern provides a fairly reliable means of particle identification, but since the aim is to determine the neutrino flavor, only single-ring events (quasi-elastics) are used to achieve maximal purity. Electron-like events produce a diffuse showering pattern associated with the electron (or positron), while muon-like events result in a much sharper, non-showering pattern. The correlation between $\nu_e(\nu_\mu)$-induced events and single-ring (non)-showering events is found to be $87 \pm 1(stat)\%$ $(92 \pm 1(stat)\%)$.

The result for the ratio is [Bec92]:

$$R_{atm}^{IMB} = 0.54 \pm 0.05(stat.) \pm 0.11(syst) \tag{3.43}$$

But this significantly low ratio seems to be **independent** of the zenith angle, suggesting it is not related to the distance from the neutrino production point.

- (Super-)Kamiokande

We have already described the (Super-)Kamiokande detector in section 3.3.2.

For the atmospheric neutrino analysis, the Kamiokande group has divided the data in two samples: the sub-GeV sample contains events with a visible energy $< 1.33\ GeV$, while the multi-GeV sample contains the events with visible energy $> 1.33\ GeV$. They have also considered two different types of events: fully contained and partially contained. To improve the purity of the partially contained sample, only muon-like events are considered. The total exposure time is 8.2 kton-year for the fully contained sample and 6.0 kton-year for the partially contained sample (the fiducial volume is slightly smaller for the latter).

As opposed to IMB, the Kamiokande group has used about 30 % of the multiple ring events for the study of the muon-like to electron-like ratio. They require that 80 % of the total visible energy be seen in one ring to be able to identify the neutrino flavor. Note that this is only done for fully contained events.

These are the results obtained by Kamiokande [Fuk94]:

$$R_{atm}^{Kamiokande}(sub-GeV) = 0.60\ ^{+0.06}_{-0.05}(stat.) \pm 0.05(syst) \tag{3.44}$$

$$R_{atm}^{Kamiokande}(multi-GeV) = 0.57\ ^{+0.08}_{-0.07}(stat.) \pm 0.07(syst) \tag{3.45}$$

We see that like IMB this result is significantly lower than expectation. But we'd like to draw the attention of the reader to table (3.3) where the distribution of fully contained, Multi-GeV events between the various categories is given. Compared to the simulation, there is an excess of electron-like events, but this excess is only significant in the single ring events. For the multiple ring events, the excess seems to be about 10 %, well within the statistical error.

The Kamiokande group has also studied the angular dependence of the ratio [Fuk94]. Whereas the sub-GeV sample looks perfectly flat, the multi-GeV sample seems to exhibit a clear angular dependence, with a strong suppression for upward-going events and no suppression for downward-going neutrinos. The Kamiokande Collaboration

	Data SR	Data MR	MC SR	MC MR
e-like	73	25	45.9 (49.1)	20.7 (21.6)
μ-like	21	10	25.8 (27.3)	12 (13.2)
Total	195		181.0 (189.1)	

Table 3.3: Distribution of fully contained, multi-GeV Kamiokande events between single ring (SR) and multiple ring (MR) for data and two Monte Carlo simulations (the numbers between brackets come from the second simulation). The difference between the two Monte Carlo simulations is the predicted neutrino flux.

claimed that their data excluded independence of angle at the 99 % C.L., but a reanalysis of the errors by D. Saltzberg [Sal95] showed that this is really only 95 %.

At the 1997 summer conferences, preliminary data from a 20.1 kt-year exposure of Super-Kamiokande were shown for the first time [Nak97, Tot97]. Although a paper is not yet available, we can cite the results assuming the analysis is very similar to the Kamiokande analysis:

$$R_{atm}^{Super-K}(sub-GeV) = 0.64 \pm 0.04(stat.) \pm 0.05(syst) \quad (3.46)$$

$$R_{atm}^{Super-K}(multi-GeV) = 0.60 \pm 0.05(stat.) \pm 0.07(syst) \quad (3.47)$$

These numbers are fully compatible with the earlier results of Kamiokande.

Angular dependence plots were also shown and now the multi-GeV data does not exhibit a clear angular dependence anymore while the sub-GeV data on the other hand appears to follow a slight slope. But the data is presented in a histogram ranging from $cos\theta = -1$ to $cos\theta = 1$[4] divided in 5 bins. Since the angular correlation between the neutrino direction and the charged lepton has an r.m.s. $\approx 60^o$ for the sub-GeV data [Fuk94], neighboring bins cannot have very different values and much care has to be taken before drawing any conclusions.

O. Ryazhskaya suggested [Rya94] that electron neutrino interactions could be faked by the reaction $n + A \rightarrow \pi^0 + X$, where the neutron is produced in a muon interaction in the rock surrounding the detector. A study from the Kamiokande Collaboration has since then showed [Fuk96b] that this contamination is lower than 1.2 %.

3.3.6 Discussion on the Atmospheric Neutrino Results

Is There a Problem?

As we have shown in the previous section, the situation is far more ambiguous in the case of atmospheric neutrinos than it is for solar neutrinos. Only one type of experiment, the water Čerenkov detector, sees a significant deficit of muon-like events or excess of electron-like events. It even looks like this deficit is only present in the single ring (quasi-elastic) events and not in the multiple ring events. In addition to this, the experimental knowledge on the neutrino-nucleon cross-section at these low energies is rather limited and deviations of up to 20 % from the generally accepted values are well possible [Lip95].

The new Soudan-2 result apparently agrees with the water Čerenkov detectors when applying a similar analysis, but an analysis including the deep inelastic events may shed

[4] θ is the measured angle with respect to the zenith direction, with $cos\theta = 1$ corresponding to downward-going neutrinos.

more light on the cause of the observed deficit. Such an analysis has been performed by the Fréjus group and they do not observe any effect.

Summarizing, the atmospheric neutrino anomaly is far from being as compelling as the solar neutrino deficit. Further analysis from Soudan-2 and new experiments ought to help clarify the situation, but for the moment experimental difficulties have as good a chance at explaining the numbers as neutrino oscillations do.

Neutrino Oscillation Interpretation

The Kamiokande group has performed a two-flavor neutrino oscillations analysis of the data for both $\nu_\mu \leftrightarrow \nu_e$ and $\nu_\mu \leftrightarrow \nu_\tau$ oscillations [Fuk94]. They have taken into account matter effects for $\nu_\mu \leftrightarrow \nu_e$ oscillations and have used the angular dependence found in the multi-GeV sample in their fit. Downward-going neutrinos in the sub-GeV sample impose a lower limit $\Delta m^2 \geq 5\ 10^{-3} eV^2$ while the up/down difference in the multi-GeV sample imposes a lower limit on the oscillation length (and therefore an upper limit on Δm^2). All the data require $sin^2 2\theta > 0.5$, which means $\theta > 22.5^o$. The best fit values are $(\Delta m^2, sin^2 2\theta) = (1.8\ 10^{-2} eV^2, 1.0)$ for $\nu_\mu \leftrightarrow \nu_e$ oscillations and $(\Delta m^2, sin^2 2\theta) = (1.6\ 10^{-2} eV^2, 1.0)$ for $\nu_\mu \leftrightarrow \nu_\tau$ oscillations. The allowed region in parameter space for $\nu_\mu \leftrightarrow \nu_e$ oscillations is visible in figure 3.9.

Quite a few people have performed a three flavor neutrino oscillation analysis of the data [Giu97]. Most authors require an MSW solution to the solar neutrino problem to fix one of the mass differences to $\Delta m^2_{12} \approx 10^{-5} eV^2$, which means this term cannot contribute significantly to atmospheric neutrino flavor change. Assuming CP conservation, only one mass term and 2 angles remain free, since neglecting one of the mass terms makes the oscillation probability independent of the corresponding angle. The results obtained then are essentially the same as those for the two-flavor analysis: $\Delta m^2_{23\ or\ 13} \approx 2\ 10^{-2} eV^2$ and at least one of the mixing angles has to be large.

3.3.7 Reactor Neutrino Experiments

The tremendous anti-neutrino flux produced by nuclear reactors ($5\ 10^{20}\ \overline{\nu_e}$ per second for a 2800 MW reactor) already led to the experimental discovery of the neutrino (see section 2.1). As these neutrinos have relatively low energy (a few MeV), neutrino oscillation experiments are sensitive to rather low values of Δm^2 (at present $10^{-2} eV^2$). But the low energy also implies that only disappearance experiments can be performed, which limits the sensitivity to the mixing angle to large values.

The detection technique is generally very similar to that pioneered by Reines and Cowan: a large tank of liquid scintillator doped with an element adequate for neutron capture is exposed to the neutrino flux. The neutrinos interact with protons in the target in the inverse beta decay reaction

$$\overline{\nu_e} + p \rightarrow e^+ + n \tag{3.48}$$

leaving as signature a prompt light pulse corresponding to the positron annihilation followed by a delayed light pulse from the desexcitation after neutron capture. Modern detectors also analyze the pulse shape of the signals for further background rejection.

Searches for neutrino oscillations measure the neutrino flux at at least two different distances and compare the observed spectra. This is done by either moving the detector after some time or by having several identical modules and taking the data simultaneously.

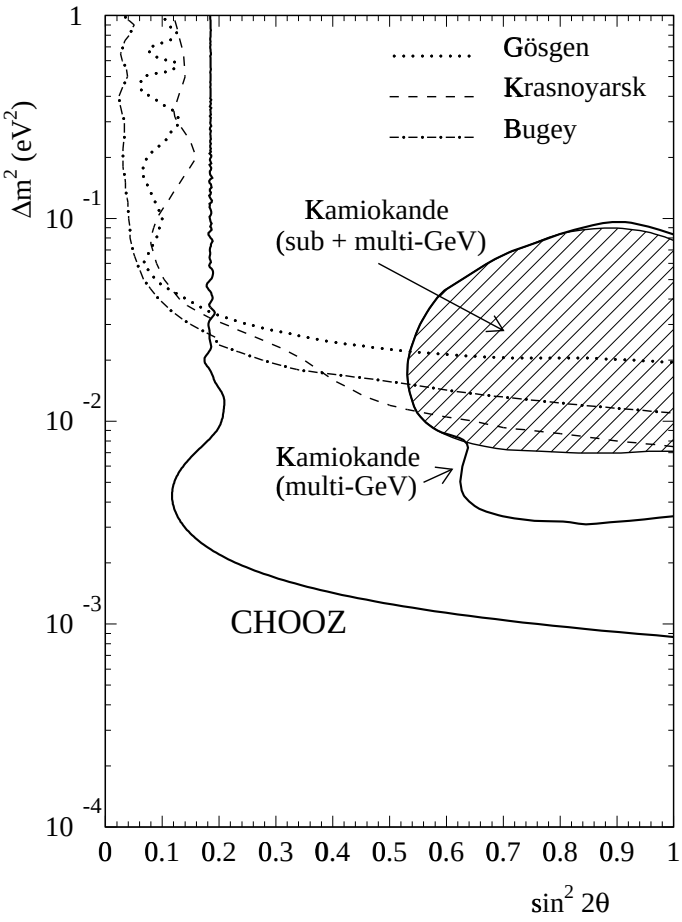

Figure 3.9: The 90 % C.L. exclusion contour for neutrino oscillations from the Chooz experiment [Apo97]. Earlier limits from the Bugey, Gösgen and Krasnoyarsk reactor experiments are shown, as well as the region allowed for $\nu_\mu \leftrightarrow \nu_e$ oscillations by the Kamiokande atmospheric neutrino observations.

Experimental difficulties include cosmic background, background from reactor neutrons and neighbouring reactors, evolution of the reactor with time, etc.

In 1984, the Bugey 1 group [Cav84] reported a difference between the expected and observed spectrum at the furthest of the two detectors they used. They considered it as an indication for neutrino oscillation. They found out in 1986 that a lack of efficiency of the veto was at the origin of the discrepancy [Tal87].

The present best result has been obtained by the Bugey 3 Collaboration, using three identical detectors at 15, 40 and 95 m from the reactor. To test the oscillation hypothesis they used two methods:

- compare the experimentally observed ratios of positron spectra at different distances to the ratios predicted by Monte Carlo,
- compare the normalized positron energy spectra measured at different distances with Monte Carlo expectation.

Since they did not observe any deviation from expectations, they calculated an exclusion region in the $(sin^2 2\theta, \Delta m^2)$ plane by allowing for neutrino oscillations but requiring compatibility with the data. The 90 % C.L. contour they have found is shown in figure 3.9 along with earlier results from the Gösgen and Krasnoyarsk reactor experiments. The Kamiokande $\nu_\mu \leftrightarrow \nu_e$ allowed region is also shown.

Two new reactor experiments should start datataking in 1997. With a 1 km baseline, the Chooz experiment [Ste93] expects to be sensitive to $\Delta m^2 = 1\ 10^{-3} eV^2$ while the Palo Verde experiment [Gra96] has a 750 m baseline and should reach $\Delta m^2 = 1.5\ 10^{-3} eV^2$.

As we write, first results from Chooz have just been made public [Apo97]. They did not observe any evidence for $\overline{\nu_e}$ disappearance and have significantly improved the limits on $\overline{\nu_e} \rightarrow \overline{\nu_x}$ oscillations, excluding the $\nu_e \rightarrow \nu_\mu$ region favored by the (Super)-Kamiokande atmospheric results (see figure 3.9).

The next generation is even already foreseen: the Perry experiment [Ste93] will be located in the Morton Salt Mine (see section 3.3.5) and its 13 km baseline should allow it to reach $\Delta m^2 \leq 8\ 10^{-5} eV^2$.

3.3.8 Accelerator Neutrino Experiments

We will extensively describe the LSND analysis here since it is the only experiment that claims a positive oscillation signal for the moment. We then give a brief overview of the other running experiments (except Chorus).

LSND

LSND (Liquid Scintillator Neutrino Detector) detects neutrinos produced in a proton target and a beam stop at the Los Alamos Meson Physics Facility LAMPF. Both the $\overline{\nu_\mu} \rightarrow \overline{\nu_e}$ and $\nu_\mu \rightarrow \nu_e$ channels are accessible in the search for oscillations.

An intense flux of 800 MeV protons produces pions in a water target with a ratio $\pi^+/\pi^- = 8$. Most of the positive pions decay at rest through the chain

$$\begin{aligned} \pi^+ &\rightarrow \mu^+ + \nu_\mu \\ &\quad\ \searrow \qquad (3.49) \\ &\qquad e^+ + \nu_e + \overline{\nu_\mu} \qquad (3.50) \end{aligned}$$

generating a flux of muon anti-neutrinos with a maximum energy of 52.8 MeV. Electron anti-neutrinos are produced in the π^- decay sequence, but most of the produced negative pions are captured before they can decay with only 5 % decaying in flight. Furthermore, nearly all the produced muons come to rest and are subsequently captured before they decay. The relative yield of $\overline{\nu_e}$ is estimated at 7.8 10^{-4} [Ath97].

The main detector volume consists of 167 tons of diluted liquid scintillator which allows the detection of both Čerenkov and scintillation light. It is surrounded by a 15-cm layer of liquid scintillator and 15 cm of lead that serve as a veto shield. The veto shield does not enclose the bottom of the detector where scintillation counters have been placed.

Electron anti-neutrinos are detected through

$$\overline{\nu_e} + p \rightarrow e^+ + n \tag{3.51}$$

which is followed by

$$n + p \rightarrow d + \gamma\ (2.2MeV) \tag{3.52}$$

so that the experimental signature is an electron signal (the detector cannot distinguish electrons from positrons) followed by a 2.2 MeV photon which is correlated with the electron in time and space. Using the combination of the Čerenkov and scintillation light, efficient electron identification is achieved together with reasonable event vertex position and electron direction reconstruction. The probability that a photon detected just after an electron is correlated with said electron is quantified by means of a likelihood ratio R. $R = \mathcal{L}_c/\mathcal{L}_a$ where $\mathcal{L}_c$ and $\mathcal{L}_a$ are the likelihoods that the photon is correlated or accidental, respectively. The likelihood function is derived from the time of detection of the photon after the electron, the number of photomultiplier hits and the distance between the reconstructed photon and primary vertex positions.

After imposing 36 $MeV < E_e < 60\ MeV$ to suppress the background from $\nu_e\ ^{12}C \rightarrow e^-\ ^{12}N$ with an accidental photon, and with the requirement $R > 30$, the LSND Collaboration observes [Ath96] a net excess of 17.4 ± 4.7 events after subtracting all the backgrounds they considered. The probability that this excess is due to a statistical fluctuation of the expected total background of 4.6 ± 0.6 events is 4.1 10^{-8}.

Interpreting the excess of events as due to neutrino oscillations, they compute the oscillation probability by fitting to the R distribution of all beam on minus beam off events satisfying 20 $MeV < E_e < 60\ MeV$. They find an oscillation probability of $0.31\ ^{+0.11}_{-0.10} \pm 0.05\%$.

The LSND Collaboration has also performed a search for $\nu_\mu \rightarrow \nu_e$ oscillation [Ath98] where the muon neutrino is produced in the pion decay in flight. Here the electron neutrino is detected through the reaction

$$\nu_e + C \rightarrow e^- + X \tag{3.53}$$

Since the experimental signature is limited to the detection of an electron, the analysis is radically different. First of all, they require that there be no activity in the detector in the 51.2 μs before and 30 μs after the event. The electron energy has to satisfy 60 $MeV < E_e <$ 200 MeV, thus eliminating all electron neutrinos from muon decay except the tails due to resolution. Two very sophisticated electron-identification algorithms have been developed based on likelihood methods, significantly improving the position, direction and energy resolution (the latter being limited by the response of the photomultiplier tubes).

As expected, the two independent electron identification algorithms lead to two slightly different, but compatible results: analysis "A" selects 23 events for an expected background

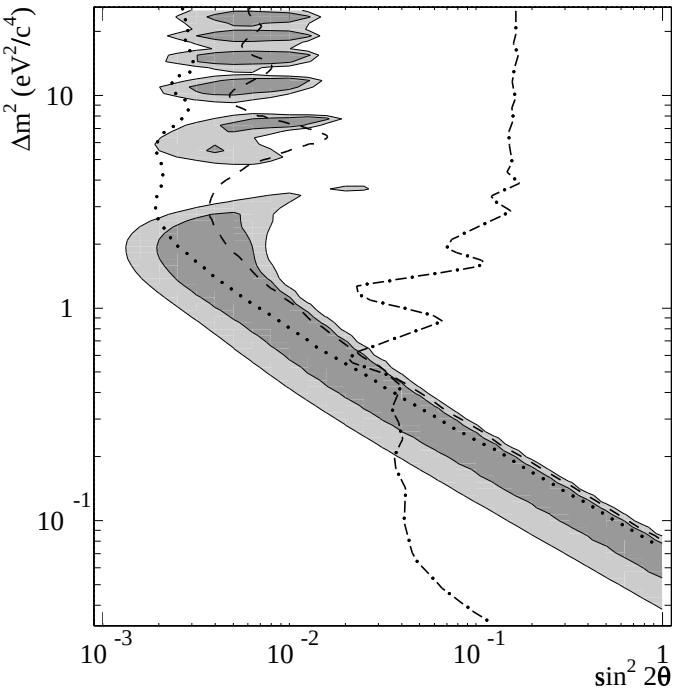

Figure 3.10: LSND allowed region in two-neutrino oscillation parameter space from the $\overline{\nu_\mu} \to \overline{\nu_e}$ analysis [Ath96]. The dark and light areas correspond to 90% and 99 % likelihood regions respectively. The 90 % C.L. excluded areas from Karmen (dashed), E776 (dotted) and the Bugey-3 reactor experiment (dot-dashed) are also shown.

of 12.5 ± 1.1 events (the probability this background fluctuates to 23 events is 7.0 10^{-3}), while analysis "B" selects 25 events for an expected background of 14.9 ± 1.8 events (here the probability of fluctuation is 1.6 10^{-2}). The corresponding oscillation probability is $(0.26 \pm 0.10 \pm 0.05)\%$

This is compatible with what has been found in the $\overline{\nu_\mu} \to \overline{\nu_e}$ channel for which the allowed region is shown in figure 3.10.

Karmen

Karmen is a 56 ton liquid scintillator calorimeter operating at Isis, a facility which produces a beam virtually identical to the LAMPF beam used by LSND. The detection of electron neutrinos and anti-neutrinos is nearly the same as the one used in LSND except that Čerenkov light is not detected. Although originally the experiment was designed to be slightly less sensitive than LSND (see figure 3.10), the signal seen has prompted the Karmen group to perform an upgrade of their experiment. With this improvement they should be able to cover the full LSND allowed region by the year 2000 [Eit97].

Note that since Isis produces a 100 ns beampulse, Karmen is able to measure the muon lifetime by detecting the neutrinos produced in its decay. They have reported [Arm95] an anomaly in the distribution of the time of arrival of these neutrinos. They will continue the investigation of this signal.

Nomad

Chorus and Nomad are two complementary experiments detecting neutrinos from the same high-energy beam. As Chorus will be extensively described in the next chapter, let us just describe Nomad [Ast90] and its approach to the search for $\nu_\mu \leftrightarrow \nu_\tau$ oscillations.

Nomad's target consists of high-precision driftchambers located inside a dipole magnetic field. This allows precise determination of the track parameters, including charge and momentum. To select ν_τ charged-current interaction candidates, Nomad then uses the kinematic correlations between the missing transverse[5] momentum (carried away by the ν_τ produced in the tau decay) and the transverse momenta of the charged tau daughter(s) and the hadronic shower. The main limit to the sensitivity of the experiment stems from transverse momentum resolution and the production of low energy particles at the primary vertex which cannot be reconstructed. The expected Nomad sensitivity is nearly the same as Chorus'.

Prospects

In the $\nu_\mu \leftrightarrow \nu_e$ "sector", the LSND group plans to perform a confirmatory experiment at the Fermilab booster, called Boone [Chu97], while as we write this another group proposes an experiment at the CERN PS [Arm97]. A nice feature of these experiments is that they will also be able to measure the electron neutrino cross-section in the atmospheric neutrino range. Both will search for oscillations with probabilities down to 10^{-3} for $\Delta m^2_{e\mu} \approx 1eV^2$.

The $\nu_\mu \leftrightarrow \nu_\tau$ search will likely be continued with the construction of Cosmos [Cos95] at Fermilab and/or Tosca [Aya97] at CERN. These experiments should be able to explore the very small mixing angle region down to $sin^2 2\theta_{\mu\tau} \leq 10^{-5}$.

Furthermore, plans to send neutrino beams over long baselines from KEK to Super-Kamiokande, from CERN to Gran Sasso and from Fermilab to the Soudan Mine are well advanced. Although the low statistics will certainly hinder the experiments, the long baseline will make them sensitive to lower values of Δm^2 than the "short baseline" accelerator experiments.

3.4 Double Beta Decay

The neutrinoless double beta decay reaction

$$(A, Z) \rightarrow (A, Z+2) + 2e^- \tag{3.54}$$

can be described by the diagram in figure 3.11. We see that this requires the transition $(\overline{\nu_e})_R \rightarrow \nu_{eL}$, which in terms of fields can be written $\overline{\nu_{eL}}(\nu_{eL})^c$. This is nothing but the Majorana mass term we have written in section 2.4.3 (equation 2.30). So we have a second-order weak process with a suppression factor m_M/E due to the change of spin and an amplitude proportional to the mass m_M.

One might argue that the existence of right-handed weak charged-currents would allow the Majorana neutrinos to be massless since it can for example be absorbed while right-handed at the vertex on the right. However this is not true as long as the weak interactions are described by a gauge theory [Kay89].

Since in the case of neutrinoless double beta decay all outgoing particles can be measured, the experiments look for a peak in the combined electron spectrum at the Q-value

[5] Here transverse denotes perpendicular to the beam direction.

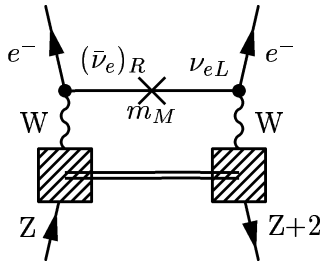

Figure 3.11: Neutrinoless double beta decay diagram for Majorana neutrinos. The cross represents the neutrino mass term.

of the reaction. The measurement is translated into a lifetime limit (the reaction has not been observed so far) which in its turn can be converted into an upper limit on the neutrino mass under some assumptions (neglect contributions from right-handed currents, ...).

The best present limit is obtained by the Heidelberg-Moscow experiment [Gun97], which uses germanium as the decay candidate *and* as detector. They have put a limit on the half life of $T^{0\nu}_{1/2} > 7.4\ 10^{24} yr$ at 90 % C.L. Neglecting right-handed currents they can put an upper limit on the effective mass (see [Kay89]) of the heaviest neutrino of 0.6 eV (90 % C.L.).

3.5 Summary

Neutrino experiments have provided and still provide valuable results for our better understanding of the weak and strong interactions. But the main focus is now on neutrino oscillations. The combination of all the experimental results may make the situation appear to be a little confused, but it should be clarified by figure 3.12, which summarizes the results in terms of two-flavor oscillation.

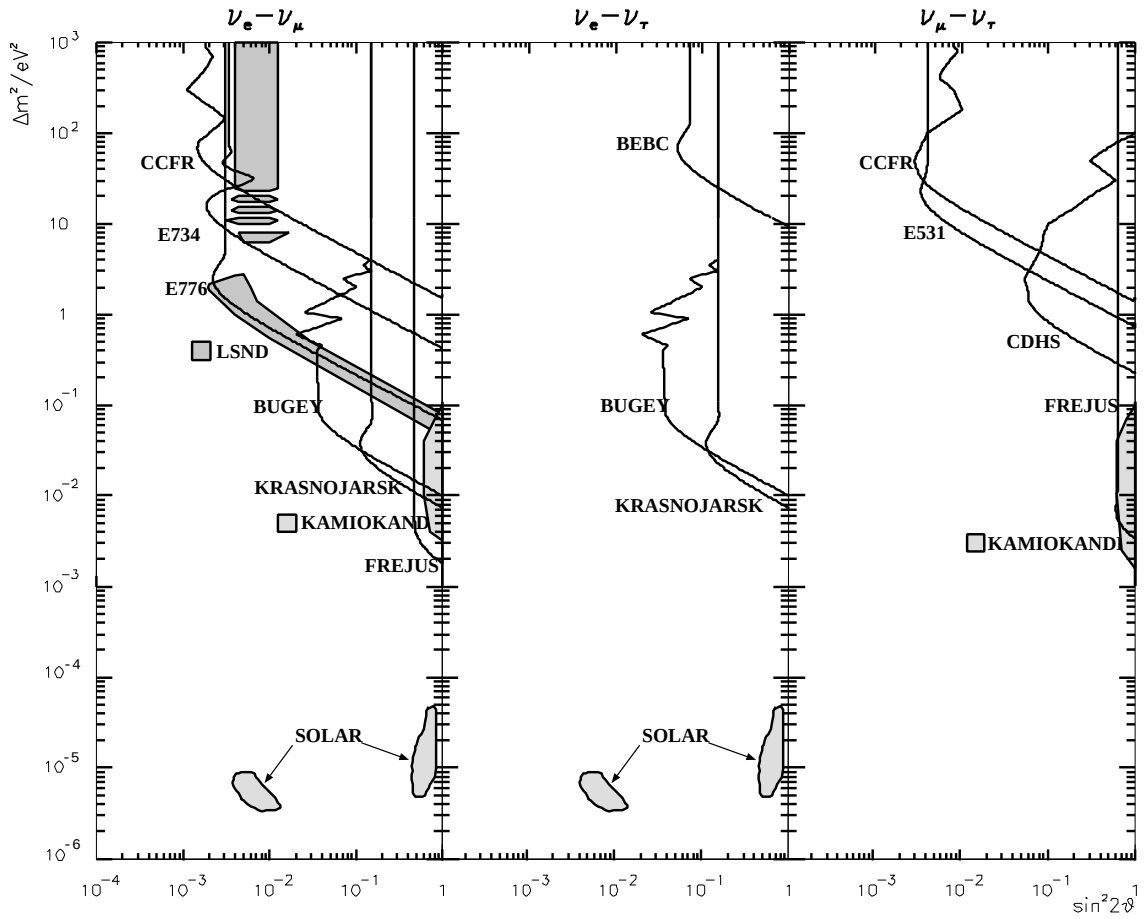

Figure 3.12: Summary of the present experimental results in terms of two-flavor neutrino oscillations [Bru97a]. Shaded areas represent allowed regions.

Chapter 4

The Chorus Experiment

The Chorus Collaboration has built a new, sophisticated detector to search for $\nu_\mu \to \nu_\tau$ oscillations in the CERN Wide Band Neutrino Beam. Since the design, construction and performance of the detector have been extensively described in reference [Esk97], we will only give a brief description here. In-depth treatments of the detector elements essential to the understanding of this work will be given at the appropriate places.

4.1 The Neutrino Beam

The CERN Wide Band Neutrino Beam is produced by shooting 450 GeV protons on a beryllium target. The charged pions and kaons created in the interactions are focused or defocused with a set of specially designed magnets (the horn and the reflector) and decay in flight, thus producing a neutrino beam. Of course other particles are also produced; some of them contribute in smaller quantities to the neutrino flux. The relative abundances of the different neutrino flavors in the beam is given in table 4.1, while the spectra are shown in figure 4.1.

The "prompt" tau neutrino contamination of the beam caused by the production of D_s mesons in the target and the decay sequence

$$D_s \to \tau + \nu_\tau \ , \quad \tau \to \nu_\tau + X \tag{4.1}$$

has been estimated using two different methods [Van97a]. It is such that for Chorus

$$\frac{N^{CC}_{\nu_\tau}}{N^{CC}_{\nu_\mu}} < 4\ 10^{-6} \tag{4.2}$$

Neutrino Flavor	Relative Abundance	Mean Energy (GeV)
ν_μ	100 %	26.9
$\overline{\nu_\mu}$	5.6 %	21.7
ν_e	0.7 %	47.9
$\overline{\nu_e}$	0.17 %	35.3

Table 4.1: Relative composition of the CERN Wide Band Neutrino Beam for the Chorus experiment as obtained from the beam simulation. The results agree with the observed relative fluxes.

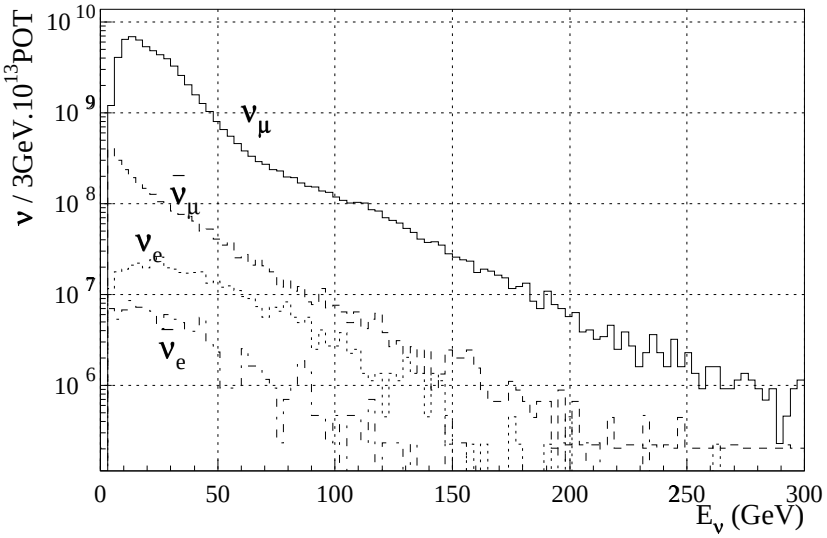

Figure 4.1: Energy spectra of the different components of the CERN Wide Band Neutrino Beam for the Chorus experiment as obtained from the beam simulation.

where $N_{\nu_\alpha}^{CC}$ is the number of charged-current events induced by neutrino flavor α. Taking into account the Chorus tau detection efficiency this leads to an upper limit on the number of background events of approximatively 0.1 detected event per 800 000 recorded ν_μ-induced charged-current events.

4.2 The Chorus Detector

4.2.1 Tau Detection Strategy

Chorus is searching for $\nu_\mu \rightarrow \nu_\tau$ oscillations through appearance of tau neutrinos in the beam. These, if present, are detected through their charged-current interactions in the target and the subsequent decay of the tau lepton into $\mu^- + \overline{\nu_\mu} + \nu_\tau$, $h^- + n\pi^0 + \nu_\tau$ or $h^- + h^+ + h^- + n\pi^0 + \nu_\tau$, where h denotes a pion or a kaon.

To be able to identify ν_τ-induced charged-current interactions unambiguously, the Chorus Collaboration has chosen to use an emulsion target. Thanks to the fantastic three-dimensional spatial resolution of nuclear emulsion (of the order of 1 μm), the tau production and decay topology can be explicitely reconstructed since the typical tau flightlength at these energies is O 1 mm). An electronic detector is used to predict event positions in the emulsion, reconstruct charge and momentum of individual particles and measure global event kinematics.

4.2.2 The Electronic Detector

Figure 4.2 is a schematic drawing of the Chorus detector. Along the path of the neutrino beam, the veto plane (V) and a set of streamer tubes (ST) are followed by the emulsion targets (4 stacks of approximatively 200 kg each) which are interspersed with scintillating fiber tracker planes. A hexagonal air-core magnet [Ber95] with scintillating fiber and emulsion trackers (since 1996) as well as streamer tubes (until 1995) or honeycomb chambers (HC)

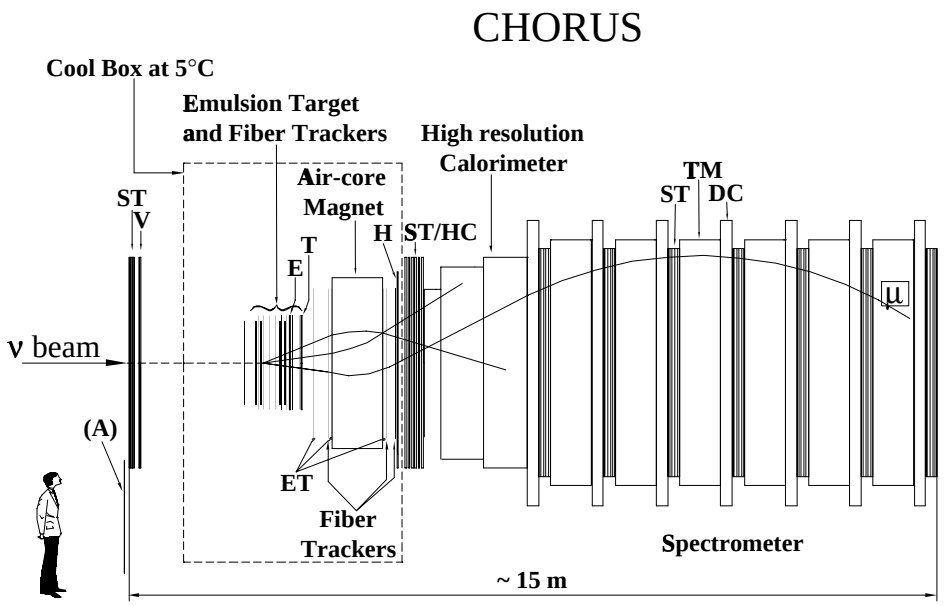

Figure 4.2: Schematic view of the Chorus detector. V,A, T,E and H are trigger hodoscopes, ST, ET, HC, TM and DC are streamer tubes, emulsion trackers, honeycomb chambers, toroidal magnets and drift chambers respectively.

(since 1996) measures particle charge and momenta up to about 15 GeV. This is followed by a high resolution calorimeter and a muon spectrometer.

The target area will be described in much detail later on, but let us write a short summary of the performances of the other "subdetectors".

The "Hadron" Spectrometer

The hexagonal air-core magnet is pulsed simultaneously with each accelerator extraction and develops a field of 0.12 Tesla. On both sides, scintillating fiber trackers record particle trajectories to determine their charge and momentum. These trackers are identical in all points except geometry to the target trackers that will be described further on. In 1996, "emulsion trackers" (emulsion sheets placed on both sides of the magnet) and honeycomb chambers were added to increase the spectrometer resolution and efficiency.

By reconstructing beam-associated muons that have been recorded by both the hadron and the muon spectrometers, the resolution of the hadron spectrometer (with scintillating fiber trackers only) has been evaluated at

$$\left(\frac{\Delta p}{p}\right)_{data} = \sqrt{(0.22)^2 + (0.035\ p)^2} \tag{4.3}$$

where p is expressed in units of GeV/c. The first term on the right-hand side is due to multiple scattering (mainly in the magnet faces) and the second to the intrinsic tracker resolution. The sign of particles with a momentum of 5 GeV/c can thus be determined with better than three standard deviations.

The Calorimeter

One electromagnetic and two hadronic parts compose the Chorus calorimeter. The electromagnetic and the upstream hadronic sections both use the so-called "spaghetti technique", in which scintillating optical fibers are embedded in lead. For the downstream hadronic section, the classical sampling approach was chosen, where lead layers alternate with scintillator layers. The transverse dimensions of each layers' modules have been chosen to optimize the shower direction determination and therefore total transverse momentum measurement. Depending on the event topology, individual particles can be identified and their energy measured.

The resolutions obtained in testbeams are:

$$\frac{\sigma(E_{had})}{(E_{had})} = \frac{(32.3 \pm 2.4)\%}{\sqrt{E(GeV)}} + (1.4 \pm 0.7)\% \quad (4.4)$$

$$\frac{\sigma(E_{em})}{(E_{em})} = \frac{(13.8 \pm 0.9)\%}{\sqrt{E(GeV)}} + (-0.2 \pm 0.4)\% \quad (4.5)$$

where E_{had} and E_{em} refer to hadronic and electromagnetic energy respectively.

Twenty-two streamer tubes have been inserted at regular intervals in the calorimeter to reconstruct trajectories of particles that are not drowned in a shower. The main aim is to link muons identified in the spectrometer with a reconstructed track in the trackers.

A detailed description of the calorimeter can be found in Reference [DiC96].

The Muon Spectrometer

Last but not least, the muon spectrometer consists of 6 iron magnets interleaved with wirechambers. The muon charge and momentum are determined by reconstructing the curvature of the muon path. The resolution is given by the following expression:

$$\frac{\Delta p}{p} = \sqrt{(0.165)^2 + (0.0018\ p)^2} \quad (4.6)$$

For low energy muons (below 5 GeV) the momentum measurement is improved by using the range of the muons in the magnets.

4.2.3 The Emulsions

The total emulsion target mass is approximatively 800 kg, split in four stacks of 200 kg each. Each of these stacks consists of 8 modules with an effective (i.e. useable) size of 35.0 $(horizontal) \times 70.0$ $(vertical) \times 2.9$ $(beam\ direction)$ cm^3 distributed over a total surface of 144×144 cm^2 (2×4 modules). The modules themselves are formed by a superposition of thirty-six 800 μm thick emulsion sheets (100 μm base plus two 350 μm emulsion layers). Just behind the last sheet of each module we have the first "interface emulsion sheet" (the Special Sheet) which has a much thicker base (800 μm) and two thin layers of emulsion (70 to 100 μm each). This different base/emulsion configuration allows better angular accuracy needed to unambiguously identify among the background the track found in the interface emulsion sheets located close to the trackers (Changeable Sheets). Finally, the Changeable Sheets are mounted 5 cm downstream from the targets and are used to significantly increase the tracker prediction accuracy before scanning the Special Sheets. They have the same base/emulsion configuration as the Special Sheets and can be replaced regularly to reduce the accumulated background.

4.2.4 Emulsion Scanning

Fully automatic emulsion scanning allows Chorus to scan all events with at least one negative particle reconstructed at the vertex. A detailed description of automatic microscopes is given in reference [Aok90], although the hardware has evolved since then and the scanning has now become orders of magnitude faster. Efforts are made to further improve this stage of the experiment.

4.2.5 Background Sources

Since we require to see a decay topology from a negative mother particle, background can only be produced by the decays of short-lived negative particles (mainly charmed mesons) or large angle elastic scattering. A list of backgrounds and their relative contributions to the total number of expected background events can be found in [deJ93].

There is however some uncertainty concerning the so-called "white kink" background, where large angle scattering of a pion without recoil of the nucleus fakes the decay topology. Fortunately, we have developed kinematic criteria that use the emulsion information together with the calorimeter data to reduce this potential background. It should also be noted that we have excellent means of evaluating this contribution by scanning negative pions in well identified charged-current events.

The total number of expected background events is below 2.

4.2.6 Proposed Sensitivity

The proposed Chorus sensitivity interpreted in a simplified two-family model is displayed in the exclusion plot in figure 4.3. At large $\Delta m^2_{\mu\tau}$ the limit is $sin^2 2\theta_{\mu\tau} < 2 \times 10^{-4}$.

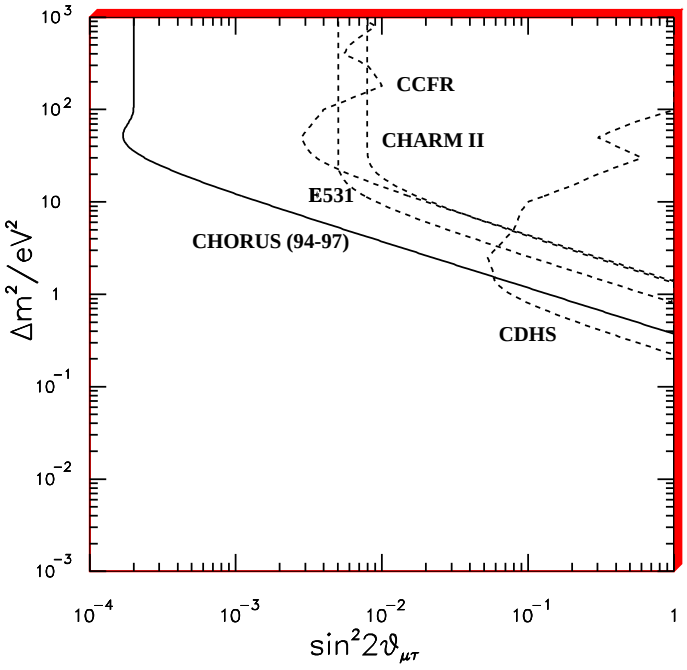

Figure 4.3: Proposed Chorus sensitivity after complete analysis. Areas excluded by some other recent experiments are also shown.

Chapter 5

The Target Trackers: Event Reconstruction and Alignment

5.1 Rôle of the Target Trackers

The Target Trackers' purpose is to predict the position of at least one of the tracks of the event in an intermediate emulsion sheet (figure 5.1). Once the track is located in this sheet, it can be followed upstream until the primary vertex is found. The interface emulsion sheet near the target emulsion is called the Special Sheet (SS), while the ones near the trackers are called Changeable Sheets (CS).

The large space (52 mm) between the emulsion targets and the closest tracker hyperplane has been chosen to allow particles to separate sufficiently for good reconstruction. Since even at that distance particles can still be very close to each other, the tracker planes are composed of arrays of 500 μm diameter scintillating fibers, which offer superior two-track separation capabilities.

5.2 Description of the Target Trackers

5.2.1 Geometry

The target area is composed of two identical modules of which one is shown schematically in figure 5.2. Each of the modules consists of 2 target emulsion stacks and 4 tracker hyperplanes in the sequence emulsion target – tracker hyperplane – emulsion target – 3 tracker hyperplanes. The modules are located behind one another for a total of 4 target emulsion stacks and eight hyperplanes.

A tracker hyperplane is an assembly of four tracker planes glued on both sides of a 1 cm thick "honeycomb" module. Each of these tracker planes corresponds to one projection: the two planes on the upstream face of the honeycomb are "non-inclined" and orthogonal to each other (Y: vertical fibers, and Z: horizontal fibers) while the two downstream layers are "inclined" by 8^o with respect to the upstream layers ($Y^{\pm}$ and $Z^{\pm}$). The direction of this rotation is alternated from one hyperplane to the next. For all the hyperplanes the sequence of projections is Z – Y – Y' – Z' [1] except for the third where it is Z – Y – Z' – Y' (due to a construction error).

The geometry of non-inclined and inclined planes is shown in figure 5.3. They are

[1] Here the superscript ' is used to indicate an "inclined" plane

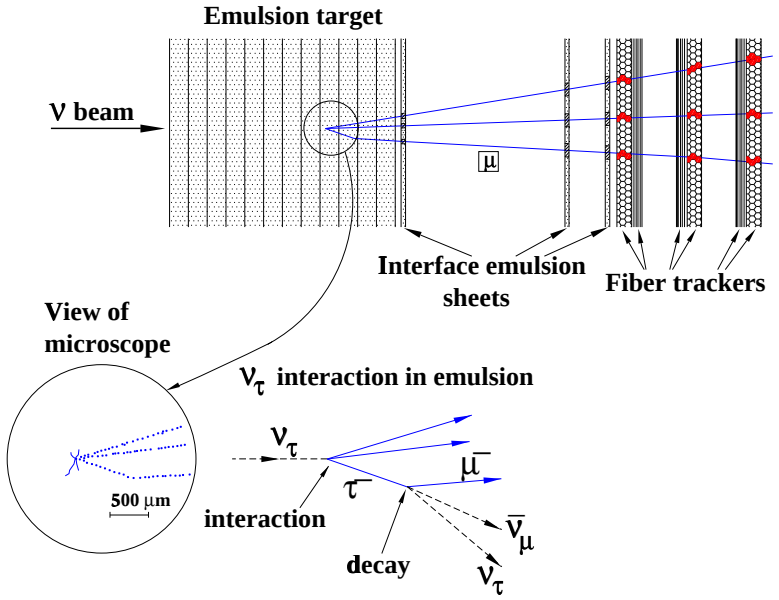

Figure 5.1: Schematic diagram of the Target Tracker philosophy: tracks are reconstructed in the trackers and the impact point in the interface emulsion sheet closest to the trackers is predicted. When the corresponding track is found in this sheet, called the Changeable Sheet (CS), a new prediction is made in the sheet closest to the emulsion target, the Special Sheet (SS). The track is then located in the SS and followed upstream to the vertex. The signature of a ν_τ charged-current interaction is displayed in the inset.

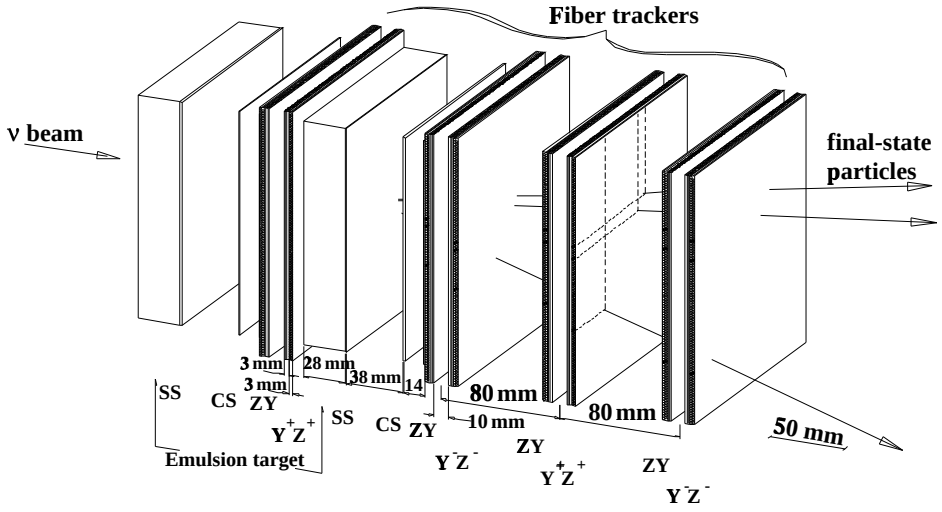

Figure 5.2: One of two modules composing the target area. Two target emulsion stacks are separated by one tracker hyperplane and followed by another three.

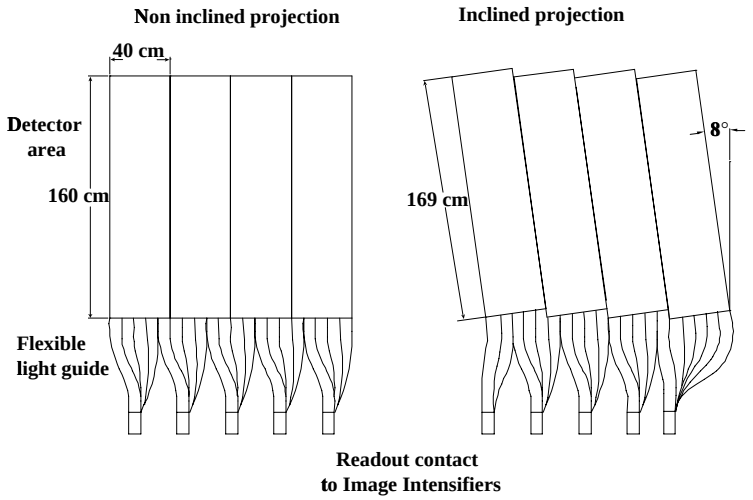

Figure 5.3: Geometry of non-inclined (left) and inclined (right) target tracker planes. The four 40 cm wide ribbons are split into 8 cm wide strips which are brought together for readout.

assemblies of four 40 cm wide "ribbons" which are split into 8 cm wide strips at one end. These are then grouped together in an optical window for readout. The 40 cm wide ribbons are composed of 5600 500 μm diameter scintillating fibers glued in 7 staggered layers (figure 5.4) for a total thickness of approximatively 3.1 mm. Detailed descriptions of the fiber-winding machine [Nak91] and the mass production of multi-layer fiber ribbons [Nak93] have been made elsewhere.

Each of the about 700 000 fibers is 2.3 m long, with a 1.6 m rigid part (1.7 m for the inclined projections) and an 0.7 m flexible section. The far ends of the fibers have been polished and sputtered with aluminium yielding a reflectivity of about 80 %.

We should also point out that the manufacturing procedure of the fiber ribbons is at the origin of a slight curvature of the rigid part of the fibers. This has been called the "banana

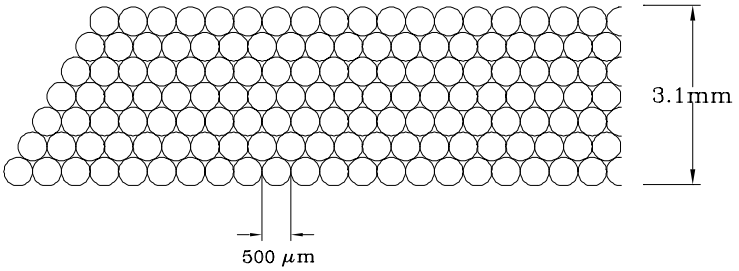

Figure 5.4: Cross section of a scintillating fiber ribbon, clearly illustrating the staggered geometry.

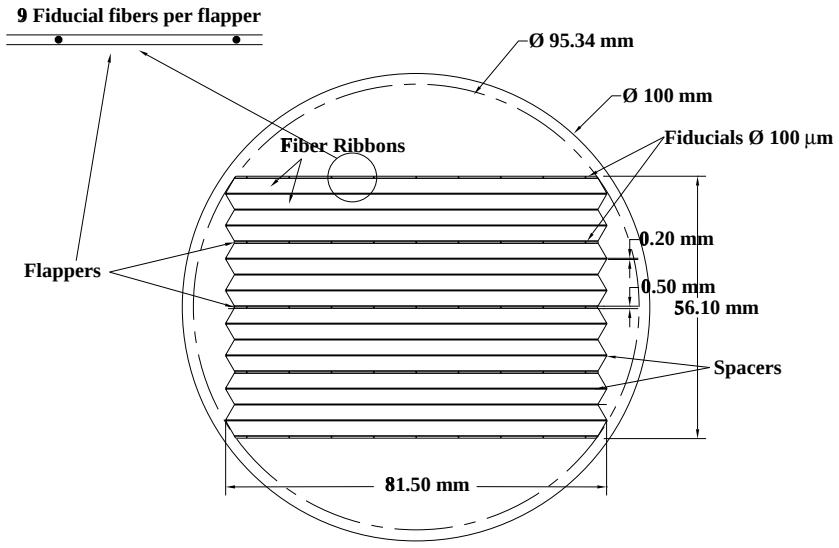

Figure 5.5: Optical window in which the fiber strips are brought together. Every 4 trips a 500 μm thick flapper with 9 fiducial fibers is inserted, while 200 μm spacers separate the strips at the remaining contact lines. The beam direction is vertical.

effect" and its maximal amplitude is less than 1 mm over 160 cm. We correct for this effect by parametrizing this curvature by a ribbon-dependent third degree polynomial fitted on 55 measured points per ribbon. The distribution of the deviations between the measured points and the fitted curves is gaussian with $\sigma = 40\mu m$.

5.2.2 Readout

Opto-electronic image intensifier chains provide a cost-effective way of reading out the fantastic number of fibers in the trackers. To link the fibers to the input of the opto-electronic chains, the 8 cm wide and approximatively 3.1 mm thick strips are assembled in groups of 16 in 40 optical windows. Such a window is illustrated in figure 5.5. The 16 fiber strips are separated by flappers which contain fiducial fibers (every 4 strips) or by spacers (at the remaining contact lines). On each of the 40 optical windows a 4-stage opto-electronic chain is mounted which amplifies and demagnifies the image. The output signal is then read by a CCD camera and sent to the DAQ. It is important to realize that strips located next to each other in real space (the tracker plane) usually end up on top of each other in the optical window. Therefore, a particle traversing the detector will appear as small, 3.1 mm high clusters of signal on the optical windows.

To monitor the image image quality at the output of the opto-electronic chains, so-called "fiducial events" are recorded in which LED's are flashed at the far ends of the fiducial fibers. As can be seen in figure 5.6, the image is markedly distorted by the chain. The distortion is parametrized with the function

$$R_{CCD} = AR_{in}\left(1 + B\left(R_{in}/R_0\right)^{\alpha}\right) \tag{5.1}$$

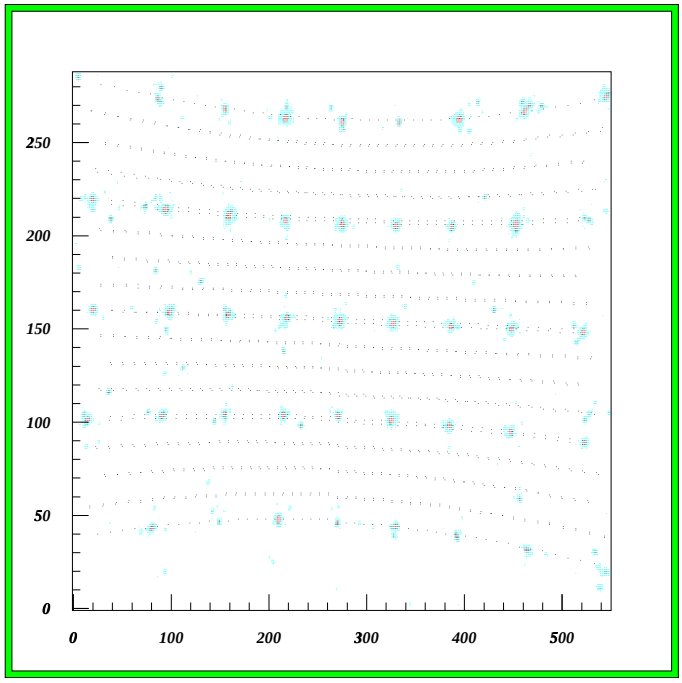

Figure 5.6: Image of a "fiducial event" (see text) as read out by the CCD. The larger blobs correspond to the signal emitted by the fiducial fibers while the dotted lines (added to the image offline) indicate the calculated positions of the strip edges. The units are pixels, with one pixel corresponding in real space to 145 $(horizontal) \times 250$ $(vertical)\mu m^2$. Note that in the vertical direction the distance in real space corresponding to a pixel depends on the horizontal position.

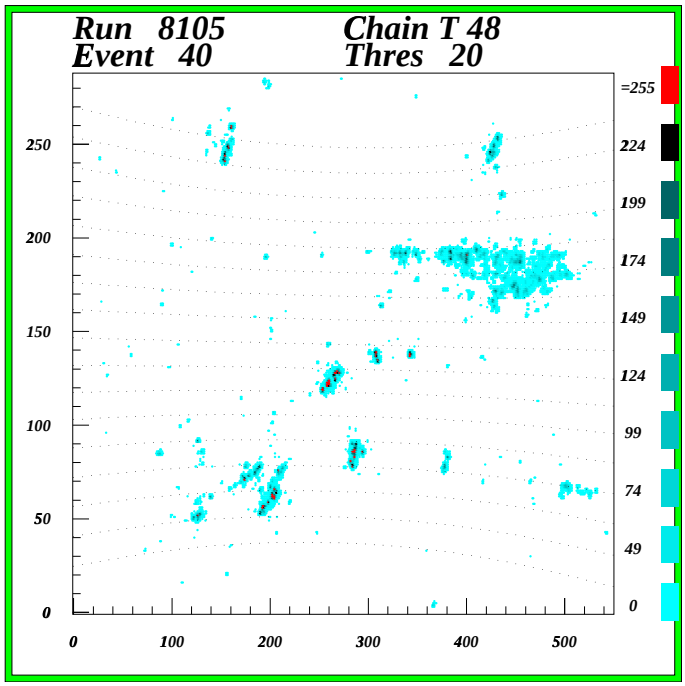

Figure 5.7: CCD image of a neutrino event. Particle track segments can clearly be distinguished as particles have traversed some of the fiber strips (for example two in the top strip). Also visible is a big blob where particles were very close to each other.

where R_{CCD} and R_{in} represent the radial position on the CCD and on the input window respectively, and $R_0 = 5\ cm$ is the radius of the input window. The parameters A (demagnification), B and α (distortion) are fitted by comparing the known positions of the fiducial fibers on the optical window with those measured by the CCD. This fit is performed for every chain and every run[2] separately and has gaussian residuals with $\sigma \approx 110\ \mu m$ in real space.

During 1994 and 1995 datataking a stray field due to an unexpected current asymmetry in the hexagonal magnet gave rise to a time-dependent rotation of the CCD image. This resulted in a different rotation coefficient for fiducial events (recorded in between accelerator extractions) and neutrino events (recorded during the extraction and magnet pulse) which could be corrected offline.

Further details on the tracker hardware and stability can be found in reference [Ann97].

5.3 Event Reconstruction

5.3.1 Track Elements and Hits

The passage of a charged particle through a scintillating fiber leads to the emission of scintillation light, which is guided along the fiber to the read-out, amplified by the opto-electronic chain and results in a signal on the CCD. A typical CCD image of a neutrino event is visible in figure 5.7. In the image, we can see particles have traversed some of the strips: roughly vertical clusters of signal of one strip height correspond to what we will call

[2] One run lasted for typically 90 minutes in 1994, 1995 and 1996 and 250 minutes in 1997.

a "track element". The larger blob visible in the right-up quadrant of the image is due to multiple particles traversing very close together.

A pattern recognition algorithm is used to identify the track elements. Using the known position of the strip edge, it assigns horizontally continuous signal in a strip to one "box". A fit[3] is performed on the signal in the box exploiting the 8-bit information provided by each pixel, and a track element with its center of gravity, width and direction is obtained. If the box is larger than the expected width from one particle it is divided in one or more "sub-boxes" until the signal in each of these is compatible with the passage of a single particle. The algorithm has been developed for neutrino events, but has also been tested with so-called "beam muon" events: in these, beam-associated muons are recorded which are mainly produced by neutrino interactions in the shielding between the decay tunnel and the detector. They result in clean, low-multiplicity signal in the detector, ideal for calibration and low-level software development. After final tuning (on neutrino events), the box width distribution, which is expected to be the most sensitive to the difference between single muons and higher multiplicity neutrino events, is virtually identical for both sets of data. This can be considered as a success since the parameter tuning was based on reconstruction efficiency rather than this width.

To recover the information from the individual fibers for future use, all the "local maxima" (i.e. pulse height maxima) in each track element are located. This is a two step procedure which starts by identifying all local maxima in a wider box to redefine the center of gravity. Each of the found maxima is assigned weight one such that we obtain a "center of local maxima". All local maxima within a fixed distance of this center are then stored in memory and considered as the "hits" (interpreted as single fiber signals) constituting the track element. The reason to redefine the center is that the track element center of gravity computed by the track element fit is just the pulse height-weighted center of all the pixels in the box. Note that from here on, the center of gravity of a track element is defined as the geometrical center of the associated hits, all considered with weight 1.

A side effect of searching for local maxima in a box rather than in a complete cluster of signal is that the maxima just outside of the box will still be recognized as hits but will be "pulled" inside.

Four distributions characterizing track elements and their hits are shown in figure 5.8. The box width obtained from the track element fit is an R.M.S.-like quantity and is nearly identical for beam muons and neutrino events. The hit density is the number of local maxima associated with the track elements; its mean value is in good agreement with expectations from geometry and light yield considerations, but it exhibits a long tail. The distance between each hit and the center of gravity of the corresponding track element is indicative of the real shape of the track elements. In the vertical (or beam) direction most of the signal is contained in a ten pixel or roughly 2.5 mm interval, while in the horizontal or transverse direction eight pixels or approximatively 1.2 mm form the width of a track element. The long tails in the horizontal direction are indicative of signal-associated noise which will be treated later on. The two peaks at zero in the distance distributions correspond to one-hit track elements.

5.3.2 Contributions to Uncertainty on Hit Position Measurement

Assuming a photon is produced in one of the fibers, and assuming we know the position of this fiber in space, then the uncertainty on the position of origin of the photon is determined

[3]This fitting procedure was developed by C. Weinheimer.

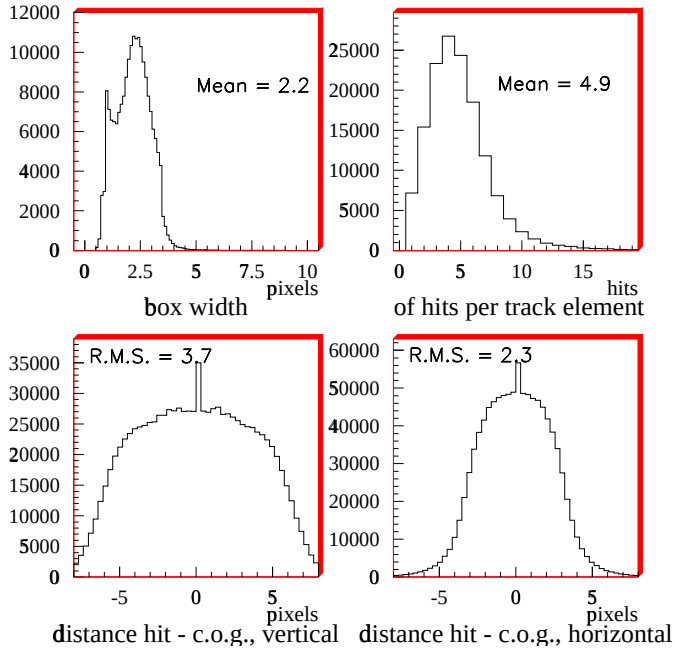

Figure 5.8: Distributions of characteristic track element parameters. The box width (top left), the hit density (top right) and the distance between each hit and the center of the corresponding track element in vertical (beam) and horizontal (transverse) direction respectively. The vertical units are arbitrary.

by the following factors:

- The $500\mu m$ fiber diameter (scattering of the photon when transmitted along the fiber).
- The uncertainty caused by the size of the spot on the CCD camera ($\sigma \approx 120\mu m$).
- The uncertainty from the distortion correction ($\sigma = 110\mu m$).
- The uncertainty due to the "banana effect" ($\sigma = 40\mu m$).
- The uncertainty caused by the displacement of the signal in the chain ($\sigma = 15\mu m$).

The uncertainties due to spot size and displacement were measured using fiducial events.

Since a traversing particle goes through multiple fibers, multiple ribbons and multiple chains, and since all these uncertainties are independent from one ribbon to another, the effect on a full track is much smaller.

5.3.3 Track Reconstruction

Track reconstruction is done individually for each of the two target tracker modules. We start with only the three tracker hyperplanes located behind the second target emulsion stack of the module. As can be seen in figure 5.2, we dispose of 3 planes in each of the non-inclined projections Y and Z, but only two in the inclined projections Y^- and Z^- and one in Y^+ and Z^+. We therefore use the non-inclined projections to find candidates for

two-dimensional projections of tracks and the inclined projections to combine these into full three-dimensional tracks.

For the two-dimensional track reconstruction, we proceed as follows for each of the non-inclined projections: we first combine each track element (using its center of gravity) in the last plane of the module with each track element in the first plane behind the second emulsion stack of the module (i.e. the appropriate projection planes of hyperplanes 2 and 4). We only reject the candidate if the difference between the constructed track slope and the fitted slopes of the track elements used is larger than twice the uncertainty on these fitted slopes. If the track passes this cut, we look in the intermediate plane if a track element is present within 1 mm (in the direction transverse to the beam) of the track impact point in the plane. The same slope requirement is made.

To combine the found two-dimensional candidates into three-dimensional tracks, we try all combinations and check if for each combination in at least 5 of the 6 inclined planes traversed a track element is present within 1 mm from the impact point. If so, we require that all but one of these track elements satisfy the slope criterion also used for two-dimensional tracking.

Three dimensional tracks are now found and they are fitted after the track element positions have been corrected for the consequences of the banana effect and plane rotation or tilting. The last two corrections are measured by the alignment procedure described in section 5.4.

The next step is to extrapolate the found three-dimensional tracks upstream and downstream as far as possible, now requiring only two track elements out of a possible four in each hyperplane and setting the allowed distance from the impact point to 2 mm. The reason for these relaxed cuts is that the particles must have traversed at least one of the target emulsion stacks, each equivalent to 1 radiation length and 0.075 interaction lengths.

Finally, the tracks are refitted based on all the hits associated with the track elements (see section 5.3.1), and after a first fit all the hits further than a distance α from the track are excluded. A final fit yields the track parameters. The reason for this refit and cut are the long tails observed in the distribution shown in figure 5.8. We find hits more than 1 mm away from the track with the distribution of hits beyond 600 μm (20 % of the signal!) dropping off exponentially with distance. Our original Monte-Carlo simulation did not present this feature, which we believe to be due to the lack of extra-mural absorber in the entrance fiber optics window of the first stage of the image intensifier chain. This leads to cross-talk and the subsequent observed signal-associated noise.

The parameter α and the distance from the center of the track element at which hits are kept are two very similar cuts performed with different knowledge. We have therefore determined these parameters simultaneously based on a comparison of predicted track position and angle on the Changeable Sheets and position and angle of the found match. The criterion used combined the sigma of a gaussian fit and the R.M.S. of the distributions to take into account possible tails. We found that the optimal maximal distance between a hit and the center of gravity is four pixels (about 600 μm) and the optimal value for $\alpha = 600\mu m$. This makes the cut at refit to be a "refinement" of the earlier distance cut. As we will see in section 5.4, one of the effects of this refinement is to get rid of the long tail in the hit density (figure 5.8, top right).

We can see how the signal associated noise filter affects simulated muons (figure 5.9) and data beam muons (figure 5.10). While the simulated muons are hardly affected, 20 % of the signal in the data is cut.

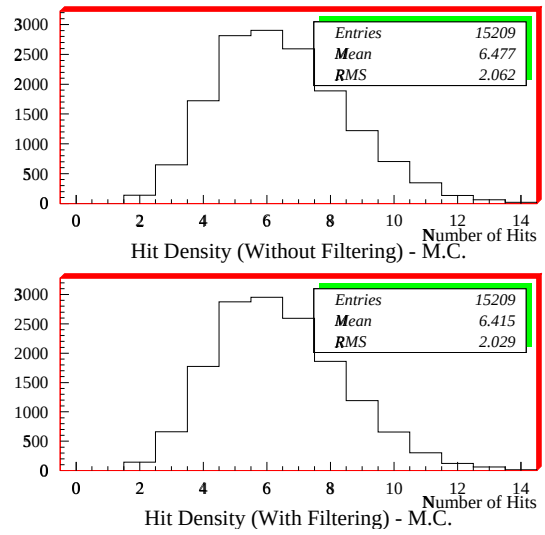

Figure 5.9: Hit density for reconstructed tracks (alignment requirements, see section 5.4) before and after application of the filtering procedure to a sample of muons from a Monte Carlo simulation in which the signal associated noise was not simulated. Only 1% of the hits are rejected, and none of the entries go below the threshold of 2 hits per plane. The average hit density of the Monte Carlo simulation was not tuned to match observation.

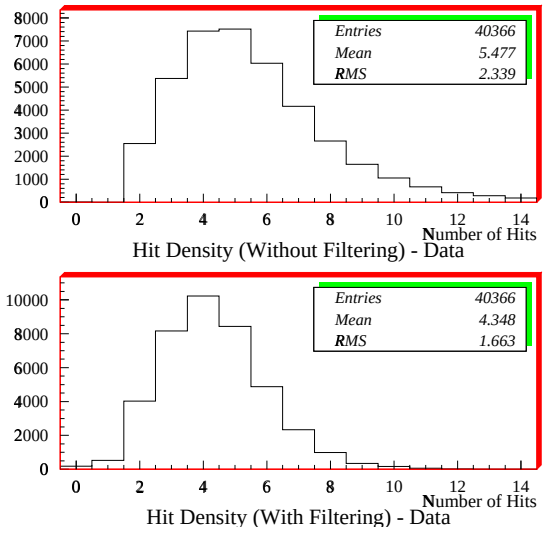

Figure 5.10: Hit density before and after application of the filtering procedure to real data (background beam muons). 20% of the hits are rejected and the long tail has disappeared. Note that although some planes have 0 hits, no tracks are lost.

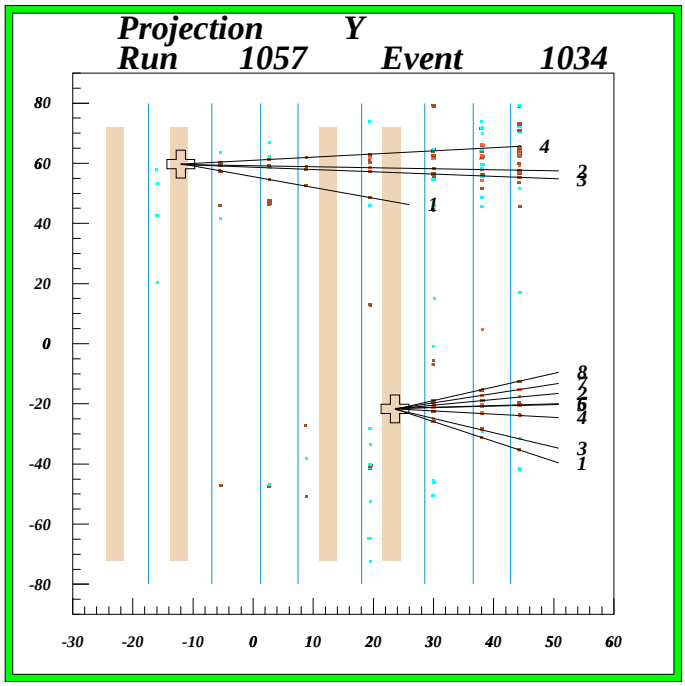

Figure 5.11: Display of an exceptional double event with neutrino interactions in stacks 2 and 4. The dots represent track elements and the dark lines are the reconstructed three-dimensional tracks. Vertex positions are marked by crosses. The axis units are cm.

5.3.4 Event Reconstruction Efficiency

Vertices are identified by combining three-dimensional tracks. The procedure, written by J. Brunner, takes into account detector geometry and provides a special handling of single track or "quasi-elastic" events. If the primary vertex (generally the one furthest upstream) is in or very close[4] to a target emulsion stack, the event is selected for scanning.

Figure 5.11 shows one projection a rather exceptional event. Two simultaneous neutrino interactions can be seen in target emulsion stacks 2 and 4. Both events are fairly clean (the one in stack 2 develops secondary showers in stacks 3 and 4 though) and very well reconstructed. The three-dimensional reconstructed tracks are shown and identified vertices are marked with crosses. The dots represent track elements while the thin vertical lines are eyeguides indicating the tracker plane positions. Only one of the two projections is displayed.

The real reconstruction efficiency is not easy to evaluate since we do not know how many interactions really took place. We therefore rely on simulated events and assume that the probably relatively small difference of efficiency between data and Monte-Carlo cancels out reasonably well when considering the ratios of reconstruction efficiencies of different types of events. In our search for oscillation we are indeed only interested in the relative reconstruction efficiencies between ν_μ-induced and ν_τ-induced charged-current events. The efficiencies to reconstruct an event in the stack in which it was generated are given in table 5.1. Note that this correctly only considers events which would have been recorded; the trigger efficiency will be considered later.

[4]For predictions the target emulsion stacks are considered to be 4 cm thick to account for the uncertainty on the longitudinal position of the vertex. The stacks are about 3.0 cm thick in real life.

Event type	$\epsilon_{Stack\ 1}$	$\epsilon_{Stack\ 2}$	$\epsilon_{Stack\ 3}$	$\epsilon_{Stack\ 4}$	ϵ_{Total}
ν_μ CC	$90.0 \pm 0.4\%$	$94.5 \pm 0.3\%$	$90.3 \pm 0.4\%$	$94.5 \pm 0.3\%$	$92.3 \pm 0.2\%$
ν_τ CC, $\tau^- \to \mu^- + X$	$89.0 \pm 0.6\%$	$94.1 \pm 0.4\%$	$87.6 \pm 0.6\%$	$93.8 \pm 0.4\%$	$91.1 \pm 0.3\%$
ν_τ CC, $\tau^- \to 0\ \mu^- + X$	$76.7 \pm 1.0\%$	$89.5 \pm 0.7\%$	$74.6 \pm 0.9\%$	$90.5 \pm 0.7\%$	$82.9 \pm 0.4\%$
ν_μ NC	$63.9 \pm 1.2\%$	$80.2 \pm 1.0\%$	$62.8 \pm 1.2\%$	$79.1 \pm 1.0\%$	$71.5 \pm 0.6\%$

Table 5.1: Results on event reconstruction efficiency obtained from simulation. The efficiency is defined by $\epsilon = \frac{Number\ of\ Events\ Reconstructed\ in\ Stack\ a}{Number\ of\ Events\ Generated\ in\ Stack\ a\ and\ Recorded}$ and is given for the three types of events needed for the oscillation search and ν_μ-induced neutral current events. The uncertainties are statistical only and only DIS events are considered. The Monte Carlo sample contained events distributed realistically in the target area (not just in the emulsion targets).

Using the obtained efficiencies and the number of reconstructed events we obtain a total number of recorded neutrino interactions compatible with the expectation from the amount of protons on target and the neutrino interaction cross-section. Detailed numbers on this will be given in chapter 6.

5.4 Alignment

5.4.1 Introduction

Between the identification of track elements and hits in the CCD image and the reconstruction of tracks there are two essential steps. The first, discussed in section 5.2.2, concerns the mapping from the CCD image to the optical window and includes the distortion correction. The second we have not discussed yet; it's the mapping from the optical window to positions in the detector and this requires precise knowledge of the fiber positions in real space. Determining these positions with the best possible accuracy is called alignment and is usually a very delicate procedure.

To be able to perform the alignment, a detailed knowledge of the mechanical structure of the detector is essential. This makes a correct determination of the degrees of freedom possible, and is certainly vital when the expected results are not reached. It is not a bad start to assume that all detector elements move with respect to each other, but we will see that this creates other difficulties.

5.4.2 Data Selection

The ideal datasample for alignment is a large sample of well-reconstructed straight tracks. We use beam muon events recorded during special runs and cosmics recorded between accelerator extractions. The cosmic sample is necessary because beam muons come in perpendicular to the detector and therefore cannot be used to determine positions along the beam.

The track reconstruction requirements are stricter to guarantee track quality. Tracks have to span a full module (all 4 hyperplanes) and are only allowed to have one track element missing in any of the 16 planes traversed. Furthermore, all track elements with

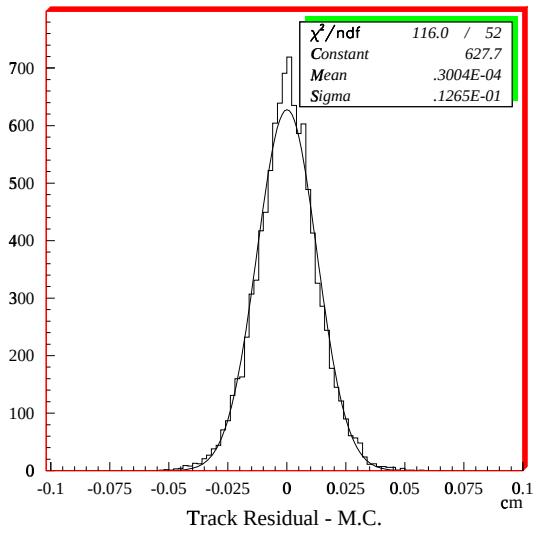

Figure 5.12: Residual distribution for a sample of simulated background beam muons (perfectly aligned detector, no banana effect, no signal associated noise).

another track element closer than 5 mm or only one hit are excluded. However, if a track element has only one hit after the noise filter is applied, it is kept.

The large statistics insure that the uncertainty on the hit position measurement (section 5.3.2) is "washed out" and no systematic biases are introduced. In this sense, it is important to filter the signal associated noise we have discussed in section 5.3.3. Figures 5.9 and 5.10 illustrate the effect of the filter on both simulated and real beam muons.

5.4.3 Residuals and Their Distributions

We now define the "hit residual" as the shortest distance from the hit to the track (with a sign giving the side of the track on which the hit is). We can even define a "track residual", which represents the shortest distance from the track to the center of gravity of the track element's hits. In the following text, residual stands for track residual unless "hit residual" is specifically stated. We can then plot residual distributions for a large number of tracks for various parts of the detector (e.g. single planes, single fiber strips, etc.). The residual distributions measure the quality of the alignment: for a perfectly aligned detector we should observe a gaussian centered on 0 with a width determined by the intrinsic resolution of the detector. This is shown in figure 5.12 for the Chorus Target Trackers. Any deviation of the mean value points to simple misalignment, whereas a deviation from a gaussian shape (shoulders,...) generally indicates misalignments in the substructure of the detector (or detector part). Gaussian shapes with too big width may suggest rotations, readout problems or other effects affecting the complete part considered (note that overlays of various curves can also fake a gaussian). Residual distributions plotted for all imaginable subdetector parts prove to be a very powerful tool to search for misalignments.

Degree of Freedom	Number of Variables	Accuracy Achieved
Transverse Translation of Fiber Strips	640 (!)	$7\mu m$
Transverse Translation of Planes	32	$5\mu m$
Rotation of Planes in the Transverse Plane	32	$2.10^{-6} rad$ ($= 1.5\mu m$ at the edges of the planes)
Translation of Planes in Beam Direction	32	$5\mu m$
Rotation of Planes in the Planes Including the Beam Direction ("Tilting")	64	$2.10^{-5} rad$ ($= 15\mu m$ at the edges of the planes)

Table 5.2: Summary of the accuracies achieved for each degree of freedom.

5.4.4 Alignment Procedure

Based on the residuals we can construct a χ^2-like function:

$$\chi_r^2 = \sum_i \frac{res_i^2(\alpha_j)}{\sigma_i^2} \tag{5.2}$$

where the index i denotes a sum over all hits of all tracks in the sample used and $res(\alpha)$ is the hit residual in function of the alignment variable α_j. σ is the intrinsic detector resolution. The alignment itself is done by minimizing the value of this χ_r^2 in function of the alignment variables for a large sample of straight tracks. For example, if we want to align all planes for possible translations in the direction transverse to the beam, the hit residual for each hit depends on the transverse position of the corresponding plane, which is represented by α_j. In this case j is a number between 1 and 32 (there are 32 planes and therefore 32 variables). Succesfull minimization will then yield the transverse positions of the planes. We have used the Minuit [Min92] software package for minimization. Details on how to handle large numbers of degrees of freedom through separation of variables are given in section 5.4.6.

5.4.5 Degrees of Freedom and Results

In addition to alignment considering all 5 degrees of freedom (3 rotations and 2 translations – translating along the fibers has no effect) of each of the 32 planes, we found that we needed to align all strips individually in the direction transverse to the beam to achieve good precision. This results in an additional 640 degrees of freedom and required a special approach to minimization which is described in section 5.4.6.

We also observed that treating each degree of freedom separately gave the best control: when trying to find the minimum for rotations and translations of one plane simultaneously, the results produced by the minimization program do not necessarily converge when iterating the procedure. A possible interpretation of this is that there are multiple "valleys" with minima, and that depending on the starting point the found minimum is different.

Table 5.2 summarizes the number of variables and accuracies obtained for each degree of freedom. Accuracy was determined by applying the procedure after having performed the alignment. These numbers agree well with the minimization uncertainty computed by the minimization software [Min92]. An example of the resulting residual distribution is shown in figure 5.13. The shape of the curve is approximatively gaussian, it is centered on zero and the difference between its width and the width found for Monte-Carlo events is

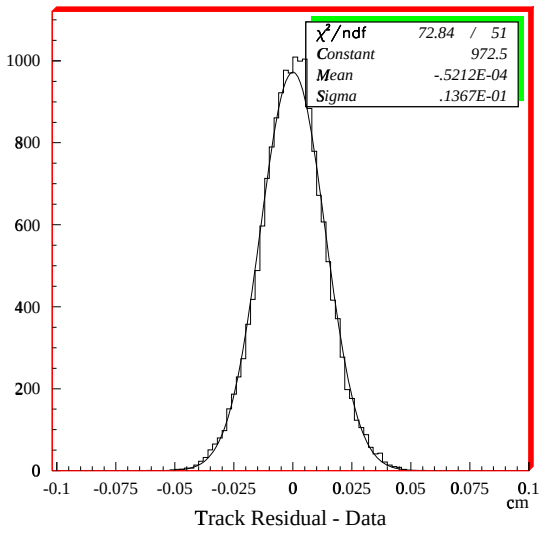

Figure 5.13: Residual distribution (in an arbitrary plane) for a sample of background beam muons after alignment (transverse denotes transverse to the beam).

only $10\mu m$. This corresponds to an additional independent uncertainty (with respect to the intrinsic detector resolution) of $50\mu m$, very close to what we expect from the banana effect (see section 5.3.2).

5.4.6 Separation of Variables

Machine limitations (rounding errors) reduce the number of variables that can be determined simultaneously by a minimization program to about 50. As we said in section 5.4.5, this number is exceeded in the Chorus Target Trackers. A solution to this problem is to use all variables, but to "fix" part of them during each minimization process. A reasonable number of variables are kept "variable" while all others are assigned a fixed value, the minimization program is run, and the found values are fixed. Another set of variables is then "released" etc.. In this way, although the program is still dealing with a too big matrix, the effective calculations are done on a matrix of adequate size. The procedure is iterated for best results.

The only remaining problem is to identify which variables have to be determined simultaneously. We found that as long as the variables are correlated by tracks, the obtained results are absolutely identical within the uncertainties. We tried various combinations: "tower geometry" where the positions of strips in the same area of successive planes is determined simultaneously, or "plane geometry" where the positions of half of the strips of 1 plane (i.e. 40 strips) are determined at the same time. The correlation is very different in the second case, since it is only due to the overlap of the strips caused by the inclination of 8 degrees of one layer w.r.t. the other. Nevertheless, the differences between the results obtained from the 2 minimizations are smaller than the uncertainties. This is another indication of the robustness of the method.

5.4.7 Detector Position Stability over Time

Alignment parameters are determined for each "Changeable Sheet Period". The Changeable Sheets are the interface emulsion sheets located closest to the trackers (see figure 5.1) and were foreseen to be replaced regularly to keep the accumulated background from random particles low. There have been 8 such periods in 1994, 3 in 1995, 2 in 1996 and 1 in 1997[5].

Since each Changeable sheet replacement involves movement in the trackers, the alignment parameters are generally computed once for each of these periods (but twice in 1997). We have therefore studied the stability of the tracker positions over time by comparing the results obtained from data from the full period with results obtained using only data from the beginning or the end of the period.

We found that for the degrees of freedom transverse to the beam, the distribution of the differences between the results is centered on 0, with an $R.M.S. = 10\mu m$ and maximal values at $25\mu m$. In the beam direction the $R.M.S. = 35\mu m$ and maximal values go up to $80\mu m$. This difference can be understood from the mechanical structure of the trackers, which are built to be able to move in the beam direction (for emulsion installation reasons). Since the movements are relatively small and no systematic shift is observed they can reasonably be ignored.

[5]The decrease in changing rate has been decided to reduce the personpower needed for scanning. It assumes that background does not cause significant losses in efficiency.

Chapter 6

Muon Identification in Chorus

6.1 Introduction

Optimizing the muon acceptance in Chorus is of significant importance not only for the identification of the signal $\nu_\tau + N \to \tau^- + X$ with $\tau^- \to \mu^- + \nu_\tau + \overline{\nu_\mu}$, but even more so to keep the background from (mainly) charm production low.

Indeed, the reaction $\overline{\nu_\mu} + N \to \mu^+ + (\textit{negatively charged charmed particle}) + X$ is one of the main backgrounds for all τ^--decay channels if the μ^+ is not identified.

We have combined information from the calorimeter and the spectrometer to maximize the muon acceptance with the priority set on tagging a muon while maintaining a good sample purity. We will see that the results are rather good and that based on a study of non-tagged muons we can conclude the inefficiency is due to physics rather than software. Furthermore, the main contribution to the contamination of the charged-current sample by neutral-current events is due to π and K decays in flight, where a muon was correctly tagged.

6.2 Software Algorithms

Let us start with a short description of each of the algorithms before explaining how they are combined.

6.2.1 Spectrometer Muon Tracking

We of course use the existing spectrometer software. This is a combination of various algorithms in itself, which choses between the results obtained by each of them based on well-defined criteria. The algorithms either use bending in the magnets or range to determine the muon charge and momentum; range is the most precise method [Hey96] but it can only be used for muons up to approximatively 6 GeV and does not give the charge. Note that except for the range algorithm, the other spectrometer tracking methods do not use the scintillators sandwiched in the magnets, such that beam muons arriving within the 500 ns gate of the wire chambers are accepted.

We have therefore added two auxiliary routines that check these scintillators (170 ns gate) and the trigger data to veto beam muons. These are described in section 6.2.6.

6.2.2 "Gap2" Algorithm

This is one of the specially developed algorithms. Originally, it was designed to tag those muons that don't make it past the second magnet of the spectrometer (stopping or exiting), using 3-d track segments identified by low-level spectrometer tracking software. The inclusion of the "one magnet fit" in the more recent spectrometer software package would have made this obsolete, where it not for the additional checks on scintillator activity (beam muon filter) and total activity (to reject showers leaking from the calorimeter) not performed in the standard spectrometer package.

The algorithm has kept most of its functionality in the identification of multiple muon events: the total activity check cited above groups 2-d track segments identified by low-level spectrometer software into single 2-d tracks (usually one track gets multiple 2-d track segments due to various possible combinations in the streamer tubes). Those belonging to already identified 3-d track segments are then subtracted. This recovers a significant amount of dimuon events even though it does not have a real effect on single muon events.

6.2.3 "Gap1" Algorithm

The second of the specific algorithms. It combines the low level 2-d information given by the spectrometer software in the first gap of the spectrometer (between the calorimeter and the first spectrometer magnet) into 2-d tracks in a way similar to that described for the activity check in gap 2 (section 6.2.2). Under the condition there's only one of such 2-d tracks in each projection (to avoid leaking showers or a single pion interacting at the end of the calorimeter), the energy deposition along the extrapolation of the track in the last 4 layers of the calorimeter is checked. It is required to be compatible with a muon (this has been tuned on Monte Carlo).

This recovers approximatively 3 % of muons (ν_μ CC) and the sample is very pure because of the stringent calorimeter requirement (checking only two layers rather than four yields a big contamination of punch-through pions). Figure 6.1 illustrates a muon (it's a Monte Carlo event) which has not been found by any of the other algorithms.

6.2.4 Calorimeter Tracking

The standard calorimeter tracking package [Pir96] is obviously also used. Here tracks are flagged as muons based on either the extrapolation from a muon identified in the spectrometer, or, in the case of a track found in the calorimeter only, based on the energy deposition. Since only two tracking projections exist, three-dimensional combination of the projection candidates is only possible with external help or very good event topologies. To reduce the contamination of the muon sample by non-interacting pions we require that the tracks reach at least the 400 cm point in the Chorus reference frame (see figure 6.1), which corresponds approximatively to the entrance of the last section of the calorimeter.

6.2.5 CLUNET

CLUNET is a neural network type algorithm developed by P. Zucchelli [Zuc94]. It identifies clusters of energy based on the assumption that the particle origin is in the target area. In function of the cluster shape and longitudinal energy deposition distribution it assigns a probability to be a hadron, electron or muon. The track parameters are of course very rough and only two-dimensional information is available.

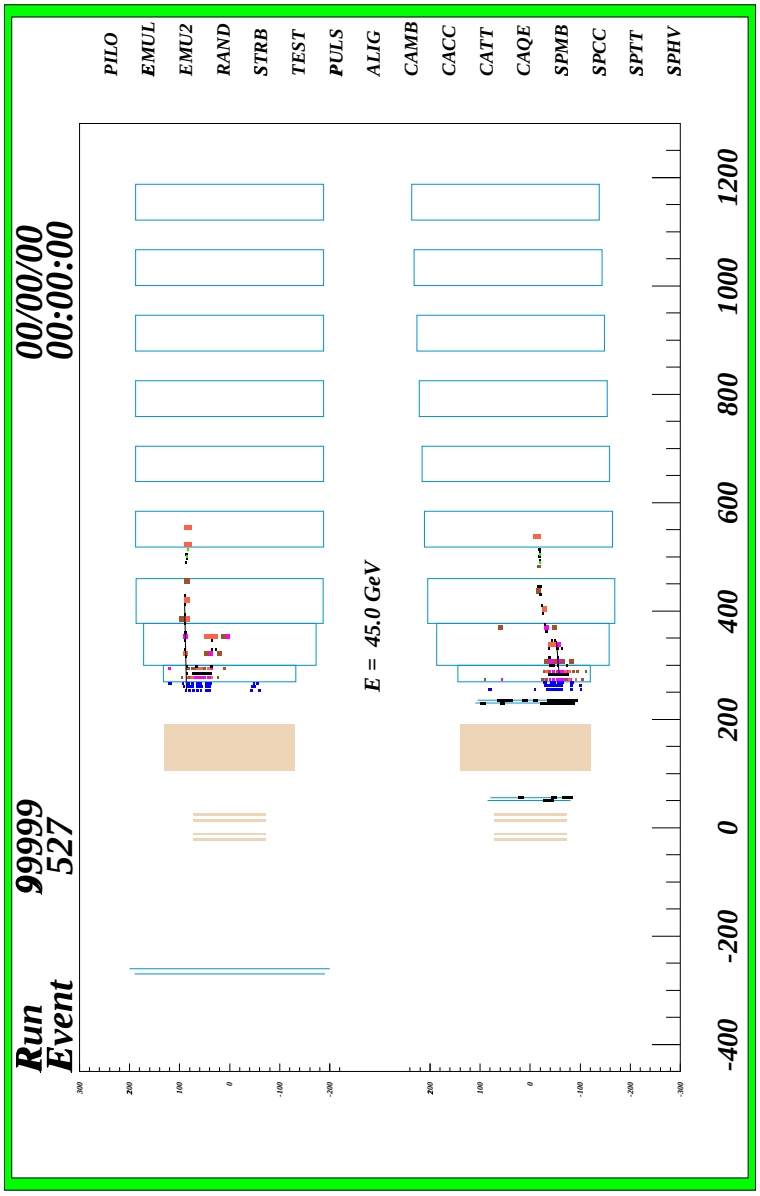

Figure 6.1: A Monte Carlo event with a muon stopping in the first spectrometer magnet. Only the "gap 1" algorithm tagged it.

6.2.6 Auxiliary Routines

Vetomu

Vetomu extrapolates the track to the veto planes, and vetoes the muon if in both veto layers the scintillator strips in the extrapolated track road have detected a signal between 50 and 1000 ns after the event. It is used to check every muon candidate found and appears to be a very useful tool to reject beam muons faking quasi-elastic events in the first target emulsion stack.

Checkscin

For the muons tagged in the spectrometer this routines checks the scintillators in the magnets to veto beam muons (the wire chamber gate is of the order of 500 ns while for the photomultipliers it is only 170 ns). Unfortunately, the scintillators only cover a circular surface inside each magnet so if the muon passes outside of the scintillator strips no veto is set.

6.2.7 Comparison and Combination of Tagged Muons

The tagging algorithms are all used independently and the information available (track parameters, ...) is stored for future use. This means that a high energy, well isolated muon can be tagged up to five times independently. All these "muons" are then compared using the track parameters at the calorimeter-spectrometer interface and the number of effectively different muons is counted.

The cut values to decide whether two "muons" are identical have been determined based on comparison distributions (from real data) which show a clear peak and a rather flat background.

Note that for the muons tagged by CLUNET or CATRAS, a single projection match is required to flag the muon as identical. A flag is then set to indicate the track parameters from this algorithm shouldn't be used for further studies.

6.3 Muon Tagging Efficiencies

6.3.1 Kinematic Considerations

It is quite clear that for low muon energies the muon tagging efficiency is strongly correlated with this energy . In Chorus, muons produced with an energy lower than 2 GeV in one of the emulsion targets have little chance of penetrating deep enough in the calorimeter to be identified. Furthermore, muon angle and momentum are correlated. This is due to the combined effects of Lorentz boost and the nucleon form factor such that low energy muons have a larger probability of being produced at a large angle, thus escaping the detector. This is clearly visible in figure 6.2, where the muon momentum is plotted in function of its production angle with respect to the neutrino beam.

The momentum of the muon produced in a charged-current interaction is related to the scaling variable $y = \frac{\nu}{E}$ where E is the incoming neutrino energy and ν is the difference between the incoming neutrino energy and the outgoing lepton energy. Therefore, y represents the fraction of the incoming neutrino energy which is transfered to the hadronic system.

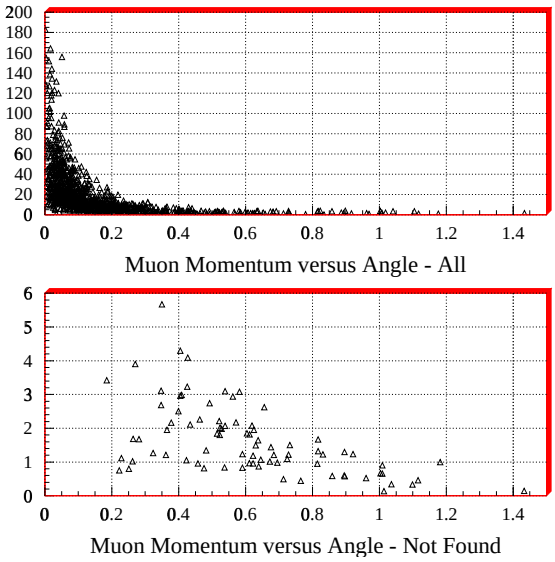

Figure 6.2: Muon momentum (GeV) versus production angle (radians) with respect to the neutrino beam for ν_μ-induced charged-current events. The top figure contains all events and the bottom one only events for which the muon was not found.

We can then examine how the charged-current neutrino interaction cross-section behaves in function of y (see also equation (3.1)):

$$\frac{d\sigma^{\nu-q}}{dy} = \frac{d\sigma^{\overline{\nu}-\overline{q}}}{dy} \propto \frac{G_F^2 s}{4\pi} \tag{6.1}$$

$$\frac{d\sigma^{\nu-\overline{q}}}{dy} = \frac{d\sigma^{\overline{\nu}-q}}{dy} \propto \frac{G_F^2 s}{4\pi}(1-y)^2 \tag{6.2}$$

Here q denotes a quark ($\overline{q}$ an antiquark), G_F is the weak coupling constant and s is the center-of-mass energy. The proportionality factor is due to the fact that the appropriate Cabibbo - Kobayashi - Maskawa angles have to be taken into account. In the approximation of negligible particle masses, the difference can be intuitively understood as follows. In the case of neutrino-quark (or antineutrino-antiquark) scattering, both particles are lefthanded so that in the center-of-mass frame the total angular momentum is zero and all directions of scattering are equally good. On the other hand, in anti-neutrino quark scattering the total angular momentum is equal to one and is directed along the momentum of the ingoing neutrino. Since the angular momentum of the outgoing antilepton-quark system is directed along the antilepton momentum, the antilepton will preferentially go in the antineutrino direction. This is equivalent to saying low y values are prefered since $y = sin^2\frac{1}{2}\theta_{cm}$ [Okun82] where θ_{cm} is the lepton scattering angle in the lepton-quark center-of-mass frame.

Experimentally this means that the muon acceptance is significantly better for $\overline{\nu_\mu}$-induced events since there are relatively less events with a low energy muon compared to ν_μ-induced events. The top histogram in figure 6.3 shows the y distribution for a sample of simulated ν_μ-induced charged-current DIS events with the vertex reconstructed in the correct emulsion stack (full line) and for the events in that same sample for which at least one muon was tagged (dashed line). The middle histogram is the ratio of the two, clearly

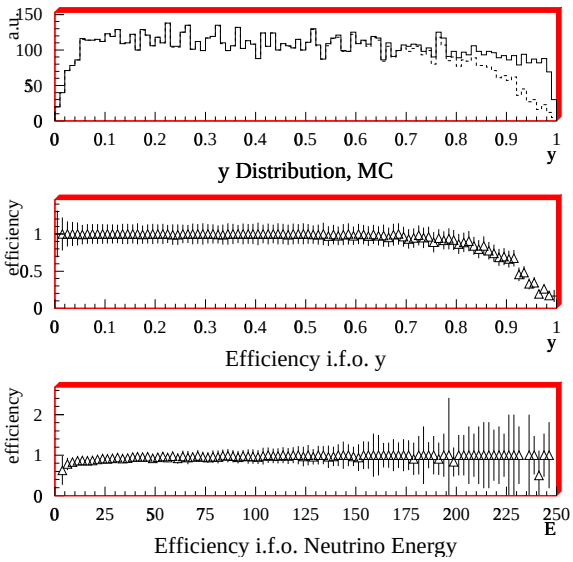

Figure 6.3: Top: y distribution for a sample of simulated ν_μ-induced charged-current DIS events with the vertex reconstructed in the correct emulsion stack (full line) and for the events in that same sample for which at least one muon was tagged (dashed line). Middle: muon tagging efficiency for these same events as a function of y, and bottom: muon tagging efficiency as a function of incoming neutrino energy.

showing the drop in muon tagging efficiency at high values of y, where the muon is relatively low energetic. For completeness, the muon tagging efficiency in function of the incoming neutrino energy is illustrated in the bottom histogram.

It should be noted that the background resulting from production of negatively charged charmed mesons in $\overline{\nu_\mu}$-induced charged-current DIS results from antineutrino scattering on antiquarks and thus does not benefit from a $(1-y)^2$ dependence of the cross-section. The threshold imposed by the charm quark mass does alter the muon energy distribution however such that the muon tagging efficiency is better than for ν_μ-induced charged-current DIS events.

6.3.2 Results

We have run the program on simulated events of various types to check the muon tagging efficiencies. The results given in table 6.1 give for each stack the fraction of events reconstructed in the correct stack for which at least one muon was tagged. Note that the starting samples have neutrino interactions distributed realistically in the target area (not only the target emulsion stacks).

The difference between the muon tagging efficiencies for ν_μ-induced CC events and ν_τ-induced CC events with the tau decaying with a muon is easily explained by the softer muon spectrum of the latter sample. This is shown in the top histogram of figure 6.4. The lower histogram in the same figure displays the energy distribution of the interacting neutrinos: due to the tau threshold, the average total event energy is 62 GeV for ν_τ-induced CC events while it is 49 GeV for ν_μ-induced events.

The larger number of pions present in ν_τ-induced CC events where the τ^- decays without

Event type	$\epsilon^{\geq 1\mu}_{Stack\ 1}$	$\epsilon^{\geq 1\mu}_{Stack\ 2}$	$\epsilon^{\geq 1\mu}_{Stack\ 3}$	$\epsilon^{\geq 1\mu}_{Stack\ 4}$	$\epsilon^{\geq 1\mu}_{Total}$
ν_μ CC	$92.3 \pm 0.5\%$	$91.2 \pm 0.6\%$	$93.7 \pm 0.5\%$	$93.1 \pm 0.5\%$	$92.6 \pm 0.3\%$
ν_τ CC, $\tau^- \to \mu^- + X$	$88.7 \pm 0.6\%$	$87.6 \pm 0.6\%$	$88.2 \pm 0.6\%$	$87.7 \pm 0.6\%$	$88.0 \pm 0.3\%$
ν_τ CC, $\tau^- \to 0\ \mu^- + X$	$9.8 \pm 0.8\%$	$11.1 \pm 0.8\%$	$12.5 \pm 0.9\%$	$13.5 \pm 0.8\%$	$11.8 \pm 0.4\%$
ν_μ NC	$8.0 \pm 0.9\%$	$7.1 \pm 0.7\%$	$9.0 \pm 0.9\%$	$9.3 \pm 0.8\%$	$8.4 \pm 0.4\%$
$\overline{\nu_\mu}$ CC with C, $C \to \mu^- + X$	$99.2 \pm 0.3\%$	$98.9 \pm 0.3\%$	$99.6 \pm 0.2\%$	$99.1 \pm 0.3\%$	$99.2 \pm 0.1\%$

Table 6.1: Efficiency to tag at least one muon for deep inelastic scattering events which have been reconstructed in the right stack. The starting Monte Carlo sample had events distributed realistically in the target area and C denotes a charmed meson or baryon. Note that we didn't apply any selection based on the measured muon charge.

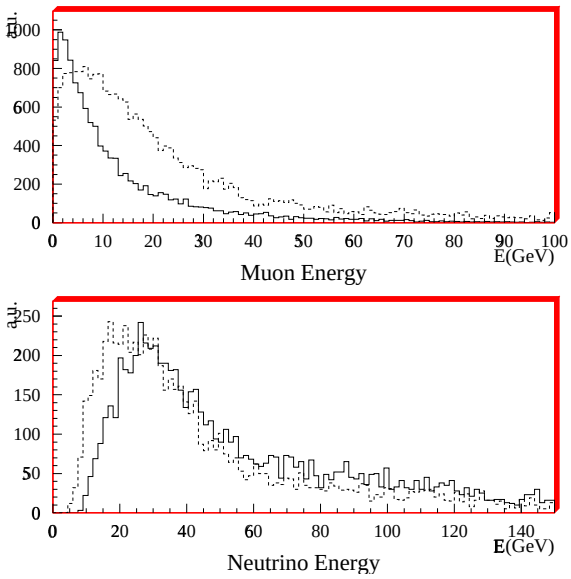

Figure 6.4: Top: Muon energy distribution for muons from tau decay (solid line) and primary muons from ν_μ CC interactions (dashed line). The mean energy is 13.3 GeV for the tau daughters and 21.9 GeV for the primary muons. Bottom: Neutrino energy distribution for ν_τ-induced CC interactions (solid line) and ν_μ-induced interactions (dashed line). The mean energies are 62 and 49 GeV respectively. Note that here we have assumed a large value of Δm^2.

Event type	$\epsilon^{\mu\ to\ scan}_{Stack\ 1}$	$\epsilon^{\mu\ to\ scan}_{Stack\ 2}$	$\epsilon^{\mu\ to\ scan}_{Stack\ 3}$	$\epsilon^{\mu\ to\ scan}_{Stack\ 4}$	$\epsilon^{\mu\ to\ scan}_{Total}$
ν_μ CC	$49.9 \pm 1.0\%$	$52.6 \pm 1.0\%$	$50.0 \pm 1.0\%$	$53.4 \pm 1.0\%$	$51.4 \pm 0.5\%$
ν_τ CC, $\tau^- \to \mu^- + X$	$53.0 \pm 1.0\%$	$55.8 \pm 0.9\%$	$51.4 \pm 1.0\%$	$56.5 \pm 1.0\%$	$54.1 \pm 0.5\%$
ν_τ CC, $\tau^- \to 0\ \mu^- + X$	$0.9 \pm 0.2\%$	$1.2 \pm 0.3\%$	$1.5 \pm 0.3\%$	$1.5 \pm 0.3\%$	$1.3 \pm 0.1\%$
ν_μ NC	$0.3 \pm 0.2\%$	$0.3 \pm 0.2\%$	$0.5 \pm 0.2\%$	$0.8 \pm 0.3\%$	$0.5 \pm 0.1\%$
$\overline{\nu_\mu}$ CC with C, $C \to \mu^- + X$	$4.2 \pm 0.6\%$	$2.7 \pm 0.5\%$	$4.4 \pm 0.7\%$	$3.3 \pm 0.6\%$	$3.6 \pm 0.3\%$

Table 6.2: Fraction of events generated in each stack and reconstructed in the same stack which satisfy the scanning selection criteria for the "muonic events": one negative muon only, linked to the vertex and with momentum measured between 0 and 30 GeV.

a muon is the cause of the larger fraction of misidentified events with respect to ν_μ-induced NC interactions. From the evolution of wrongly identified events we also observe that muons from π or K decays must play a rôle since pions or kaons from events produced further upstream have more chance of interacting in one of the emulsion stacks before going through the "empty" space between the Target Trackers and the calorimeter.

An event-by-event study of 100 ν_μ NC events with an identified muon allowed to determine the main causes of misidentification of NC events: in 26 % of these events a real muon was tagged, 45 % were mistags in the calorimeter (of which half had a muon-like signature) and 11 % were clear mistags from the spectrometer software. The other contributions were small.

Of course, this efficiency is only of partial interest: it measures our ability to identify muons in the detector, but these muons could not necessarily be linked to a vertex track and used to search for the primary vertex or tau decay. Therefore, this efficiency is the one we're looking for when requiring a "muon-veto" to suppress background.

An additional important number is the fraction of events that will be sent to scanning as being candidate tau events and thus have a chance to be found. The criteria are the following: only one muon must be matched to the vertex[1], with a measured momentum between 0 and 30 GeV and negative charge. It must of course also be in the emulsion's fiducial volume (see chapter 7). Table 6.2 gives the fraction of events which satisfy these criteria and have been reconstructed in the right stack (and would have been recorded). The sample of events was generated in the target area with a realistic spatial distribution (i.e. not only in the target emulsions). This represents the fraction of events of each type which have a chance of being found in the emulsion among those which originate in the target emulsion and satisfy the trigger conditions.

We see that the lower reconstruction (see table 5.1) and muon tagging efficiency (see table 6.1) suffered by ν_τ-induced CC events with the tau decaying with a muon are more than compensated by the muon momentum cut imposed. This cut is based on the different muon momentum distributions which can be seen in figure 6.4.

[1] An algorithm to link a tagged muon to a vertex track has been developed by L. Ludovici.

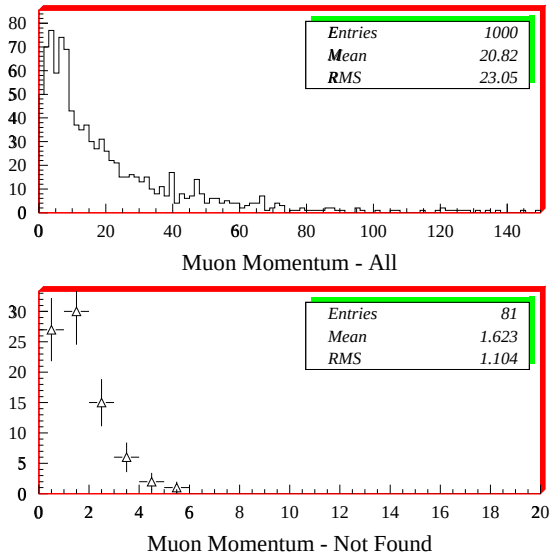

Figure 6.5: True muon momentum (in GeV) for ν_μ CC events: all events (top) and events for which the muon wasn't tagged (bottom).

Furthermore, the contribution from ν_μ-induced neutral-current events is absolutely negligible: to evaluate the contamination of the ν_μ-induced CC interactions sample the values in the table have to be divided by approximatively three due to the different cross-sections. The situation is reversed for the tau decays with/without a muon: the $\tau^- \rightarrow \mu^- \overline{\nu_\mu} \nu_\tau$ branching ratio is just 17.35 % versus 82.65 % for the other decays. Note that in the small sample of misidentified $\tau^- \rightarrow 0\ \mu^- X$ events we dispose of, only 12($\pm$10)% led us to scan a tau daughter anyway.

6.4 Study of Non-Identified ν_μ Events

In order to maximize the muon tagging efficiency, we have studied the events where the muon was not identified in more detail. This study has been performed on 1000 simulated ν_μ-induced charged-current DIS events.

Figure 6.5 shows the muon momentum for all the events in the sample and for those events for which the muon wasn't identified. As expected, the momentum is a fair amount lower for the non-tagged events. The muon angle distributions are also not surprising: the non-identified muons generally have large angle, allowing them to escape the detector. This is shown in figure 6.6. Combining these 2 variables, we see in figure 6.2 that the lower angle muons have higher momentum. This is of course not surprising. Of the 81 events where the muon wasn't tagged (in the total sample of 1000), it appears only one (at approximatively 180 mrad and 3.4 GeV) might suffer from software inefficiency. The low-momentum muons with relatively small angle (200 to 300 mrad !) do not penetrate the calorimeter far enough to be distinguishable as muons.

To be able to quantify the software inefficiency we have made the same study for much higher statistics and we have obtained that 33 events out of 11000 had a muon which was not tagged but should have been, or an 0.3 % inefficiency. We chose to display the low

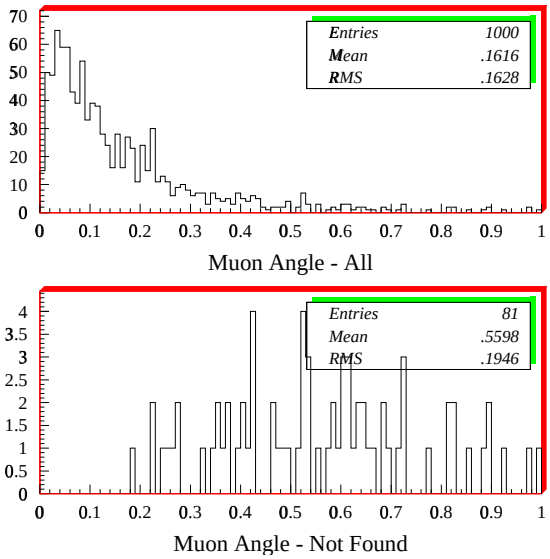

Figure 6.6: True muon angle (in radians) for ν_μ CC Events: all events (top) and events for which the muon wasn't tagged (bottom).

statistics study because visualisation is easier. We conclude that the software efficiency is close to maximal and that physics is at the origin of the small inefficiency in muon tagging.

Chapter 7

Emulsion Simulation and Determination of the Scanning Efficiencies

7.1 Introduction

The correct determination of the emulsion scanning efficiencies is crucial for the evaluation of the global event reconstruction efficiency and therefore the Chorus performance. One may argue that its importance is significantly lessened because the oscillation search result only depends on the ratio of the ν_μ^{CC}[1] to ν_τ^{CC} reconstruction efficiencies and systematics hopefully cancel in the ratio. There is however as yet no proof that this "hopefully" is true such that the best way to ensure its validity is to reproduce the found ν_μ^{CC} efficiency with good accuracy in the simulation and/or understand the possible differences. This accuracy is a measure of the reliability of the simulation which is essential in the evaluation of the ν_τ^{CC} reconstruction efficiency.

The major difficulty in the evaluation of the scanning efficiencies stems from the sheer impossibility to simulate the background accumulated by the emulsions during exposure. We have therefore developed a method that allows us to extract the real (background free) scanning efficiency from the data and compare that with the results obtained using the Monte-Carlo simulation in which event-related emulsion hits are stored.

In parallel we have written a simulation program adding Monte-Carlo grains in a digitized emulsion image to determine and improve the efficiency of the image analysis program. This program is used to analyze offline the digitized three-dimensional image of the vertex area recorded for specific event types.

We have combined the complete scanning flow simulation in one program to correctly reproduce the biases introduced at each step. We have called this program Genima.

7.2 Changeable and Special Sheet Scanning

The Changeable Sheets (CS) are the interface emulsion sheets located closest to the Target Tracker planes (see figure 5.1). Tracks are first scanned for in this sheet and then, if found,

[1] Here ν_μ^{CC} denotes a ν_μ-induced charged current interaction.

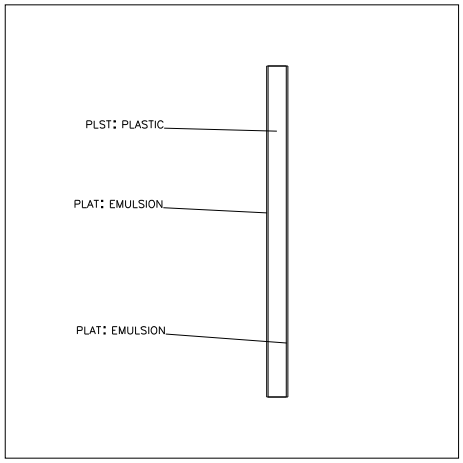

Figure 7.1: Cut of a Changeable or Special Sheet. In this figure, the beam is going from left to right and the horizontal scale has been blown up by a factor 100 with respect to the vertical scale to make the sheet's substructure visible.

the search goes to the Special Sheet (SS) (located just behind the target emulsion stack) exploiting the increase in position accuracy provided by the Changeable Sheet.

Furthermore, the Changeable Sheets can be regularly replaced to keep the background accumulated during exposure low. The frequency of these CS changes has however decreased steadily because first indications from scanning tended to show the background was reasonable and handling of these sheets both during development and scanning is rather tedious.

We shall refer to Changeable Sheet Periods as the interval of time during which one set of sheets were exposed. There are 7 such periods during 1994 datataking (numbered 2 to 8), 3 periods in 1995 (9 to 11), 2 periods in 1996 (21 and 22) and finally one period only in 1997 (i.e. the sheets were not changed during the 1997 run).

7.2.1 Description of the Sheets

Both the Changeable and Special sheets have an 800 μm thick transparent plastic base and two thin emulsion layers of 70 to 100 μm on each side. The reason for these relatively thin emulsion layers is that the development phase causes a distortion in the emulsion which grows worse with emulsion thickness. Due to this distortion, the relative positions of grains after development is different from their original one, degrading the angular precision for track measurements. The sheets all have effective transverse[2] dimensions of 35×70 cm^2, but only a surface of 34×34 cm^2 or 32×32 cm^2 is scanned for each half of each CS and SS respectively. A cut of one of these sheets is shown in figure 7.1.

7.2.2 Scanning Procedure

All the changeable and special sheet scanning is performed by an automatic system called the "Track Selector" [Aok90]. This system has been improved steadily over the last few years reaching at present a scanning speed of 100 events per day and per system. Expectations from future improvements are another gain in speed by a factor 10 to 100. The basic

[2] Again transverse means transverse to the beam direction.

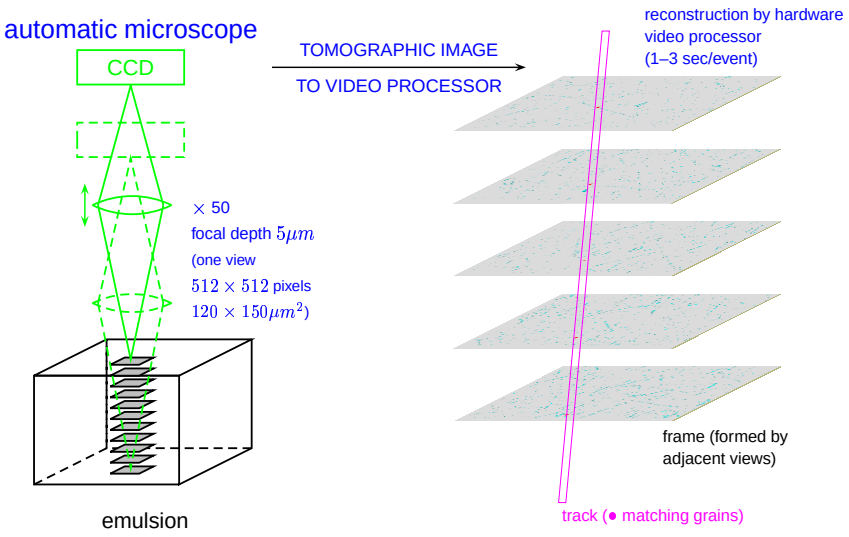

Figure 7.2: Schematic drawing of the Track Selector principle of operation.

principle of the Track Selector is explained in figure 7.2: focusing at 16 different depths spaced by about 7 μm it looks for a superposition of grains following the predicted track angle. If a "pulse height" of at least 12 is reached (i.e. aligned grains are found in at least 12 out of 16 layers) the track is accepted. The pulse height distribution for through-going tracks is shown in figure 7.6.

As experience with CS scanning increased, the selection of tracks for scanning changed such that we can distinguish four different methods:

- **Sample 1** For all the data used for the result presented at the Neutrino 1996 conference in Helsinki a maximum of 3 tracks per event were scanned in the Changeable Sheets. The muon charge and momentum measurement comes from the muon spectrometer only. This sample includes 2288 events recorded in 1994 which were scanned for and found in Nagoya, Japan. No video image analysis (see section 7.3.3) was performed for kink search.

- **Sample 2** In a second sample only muons measured in the muon spectrometer were scanned in the Changeable Sheets and video image analysis was not applied. This sample consists of 8115 events found in Nagoya, Toho and Utsunomiya, Japan.

- **Sample 3** Here also only muons measured in the muon spectrometer were scanned in the Changeable Sheets. However, video image analysis was applied for this sample of 4795 events scanned in Nagoya, Japan.

- **Sample 4** All of the 1995 data as well as a rescan of part of the 1994 data was performed scanning only one track per event. This track has to be either a negative muon with momentum between 0 and 30 GeV/c measured by the muon or hadron spectrometer, or a negative hadron with momentum between 1 and 20 GeV/c measured by the hadron spectrometer. The muonic part of this sample adds up to 16055 events scanned in Nagoya and Toho, Japan, and in Korea.

Another difference between the samples is due to the different approach to "found" tracks. The scanning surface generally used for 1994 data is 9×9 *microscope views*, which

Scanning Level	**Δ position**	**Δ Angle**
Changeable Sheets (94 data)	$< 1080 \times 810\ \mu m^2$	$< 15\ mrad$
Changeable Sheets (95 data + 94 data rescan)	$< 1320 \times 990\ \mu m^2$	$< 15\ mrad$, but stop scan if $< 6\ mrad$
Special Sheets	$< 840 \times 630\ \mu m^2$	$< 15\ mrad$ but stop scan if $< 6\ mrad$
Target Sheets	$15 + 50 * \theta_{X7\ axis}(rad)\ \mu m$	$25 + 50 * \theta_{X7\ axis}(rad)\ mrad$

Table 7.1: Criteria for track candidate acceptance as "found". Whereas for 1994 data the full surface of the Changeable Sheets was scanned, later scanning, spiraling away from the predicted value, stops as soon as a good candidate (maximum 6 mrad angular difference with prediction) is found. The target sheet scanning criteria depend on the angular distance from the X7 axis.

corresponds to a surface of $1080 \times 810\ \mu m^2$, while for 1995 data (and the 1994 data rescan) it is 11×11 *microscope views* or $1320 \times 990\ \mu m^2$. For 1994 data, the whole surface was scanned and all tracks with an angular difference with the predicted track smaller than 15 *mrad* were kept as candidates. However, for the rest of the data scanning starts at the predicted point and goes outward in a spiral. If a candidate with an angular difference smaller than 6 *mrad* is found, the search stops. The acceptance criteria at the different scanning levels are summarized in table 7.1. X7 is a testbeam in the CERN West Area whose muon halo hits the target, leading to a high background track density in the emulsions for a specific area in angular space.

To select the tracks to be scanned using the first method, Osam Sato created 7 track categories still used for comparison today. These 7 categories are explained in table 7.2.

7.2.3 Study of the Changeable Sheet Scanning Efficiency for Data

If we define the background-free scanning efficiency[3] by

$$\epsilon_{bf} = \frac{Number\ of\ times\ the\ right\ track\ is\ found}{Number\ of\ tracks\ scanned\ for} \tag{7.1}$$

and the observed scanning efficiency by

$$\epsilon_o = \frac{Number\ of\ times\ a\ matching\ track\ is\ found}{Number\ of\ tracks\ scanned\ for} \tag{7.2}$$

then it is clear that at first sight for data the background-free scanning efficiency is unknown. The observed efficiency results from a convolution of signal and background, so that an unfolding procedure seems to be necessary to extract the background-free efficiency for the data. The simulation does not have this background.

We have developed a simple method to extract the background-free scanning efficiency from the data without requiring extensive simulations. As we will see, the method is mathematically sound but relies on good control of the scanning method.

[3]Using this definition, the sources of inefficiency come not only from scanning (bad visibility, hardware inefficiency, out of acceptance) but also from fake predictions.

Category	Description
1	Muon identified in the muon spectrometer, tracked in the hadron spectrometer and the target trackers and with a spatial angle w.r.t. the TT axis $\theta_{TT\ axis} < 0.2\ rad.$
2	Muon identified in the muon spectrometer, tracked in the hadron spectrometer and the target trackers and with a spatial angle w.r.t. the TT axis $0.2 < \theta_{TT\ axis} < 0.4\ rad.$
3	Track measured in the muon spectrometer or in the hadron spectrometer, tracked in the target trackers and with a spatial angle w.r.t. the TT axis $\theta_{TT\ axis} < 0.2\ rad.$
4	Track measured in the muon spectrometer or in the hadron spectrometer, tracked in the target trackers and with a spatial angle w.r.t. the TT axis $0.2 < \theta_{TT\ axis} < 0.4\ rad.$
5	Track measured in the target trackers only and with a spatial angle w.r.t. the TT axis $\theta_{TT\ axis} < 0.2\ rad.$
6	Track measured in the target trackers only and with a spatial angle w.r.t. the TT axis $0.2 < \theta_{TT\ axis} < 0.2\ rad.$
7	Track belonging to any of the categories 1 to 6 but badly isolated in the TT, bad χ^2_{fit} in the TT, $\theta_{TT\ axis} > 0.4\ rad$ or spatial angle w.r.t. X7 $\theta_{X7\ axis} < 0.08\ rad$

Table 7.2: Track categories defined by Osam Sato for scanning selection. Muons with full reconstruction are prefered (categories 1 and 2), followed by tracks reconstructed in only one of the spectrometers (categories 3 and 4) and finally tracks reconstructed in the Target Trackers only (categories 5 and 6). The distinction made between tracks with an angle w.r.t. the TT axis smaller or larger than 200 *mrad* is due to the decrease in scanning efficiency with angle. Note that the TT axis is used rather than the beam axis (which slopes up at 42 mrad w.r.t. the TT axis) because the sheets are perpendicular to the former. Category 7 then contains all tracks with either bad isolation in the Target Trackers (i.e. another nearby track), bad value of the χ^2_{fit} of the TT fit, large angle or a small angle w.r.t. to the X7 angle.

Conditions

We require the following conditions to be satisfied:

- The random background can be assumed to be on average evenly distributed for all the scanned tracks and is independent of the background-free scanning result. This is certainly true for a single Changeable/Special/Target Sheet, but may not hold from sheet to sheet and is definitely wrong for different periods or years. We will therefore have to separate the data to make sure the condition holds. Note however that for track impact point predictions made with the same software the obtained efficiency should be stable.
- The background-free scanning efficiency can have only two results: found or not found. This is true insofar tracks from a same event do not get too close to each other (i.e. closer than the half-sides of the Changeable Sheet scanning surface) and is closely related to the "isolation" criterion for scanning. Only about 0.2 % of the tracks do not satisfy this condition, so we can safely neglect this contribution.
- The scanning surface is the same for all tracks: the method relies on the number of candidates per event and will be biased if this is not true. At CERN, scanning proceeds in this way. The systematic error induced by stopping at the first candidate can be evaluated using future data. First tests indicate it could be as high as 5 %.
- The maximal number of candidates for a single prediction is finite. This is always true.

An important consequence of the first and third conditions is that the number of events (or tracks rather) that migrate from 0 candidates to n candidates due to the background is equal to the number of tracks that migrate from 1 to $n+1$ candidates. This relies on the even distribution of background and the scanning of all views. Its validity is guaranteed in the limit of infinite statistics only, so in real life it induces a quantifiable uncertainty.

The Method

The idea is simple: the background-free result can be only zero (not found) or one (found), while in the data the number of good candidates in a given surface can be much larger due to background. Let us look at the distribution of number of candidates shown in figure 7.3.

Call $N'(i)$ the number of entries in bin i, which is the number of tracks for which i candidates were found. Then let us call $N(i)$ the number of entries we would observe in each bin for the background-free scanning efficiency. Under our second assumption $N(i) = 0$ for $i > 1$.

We proceed to call $X(i \to j)$ the number of events that have migrated from one bin to another due to the background. Here i is necessarily 0 or 1 due to our second assumption, $j > 0$ and $j > i$.

Since $X(0 \to j) = 0$ for some arbitrarily large j (last assumption), we get

$$\begin{aligned} X(1 \to j) = X(0 \to (j-1)) &= N'(j) \\ X(1 \to (j-1)) = X(0 \to (j-2)) &= N'(j-1) - N'(j) \\ &\dots \\ X(1 \to 2) = X(0 \to 1) &= N'(2) - N'(3) + N'(4) - \dots \end{aligned} \tag{7.3}$$

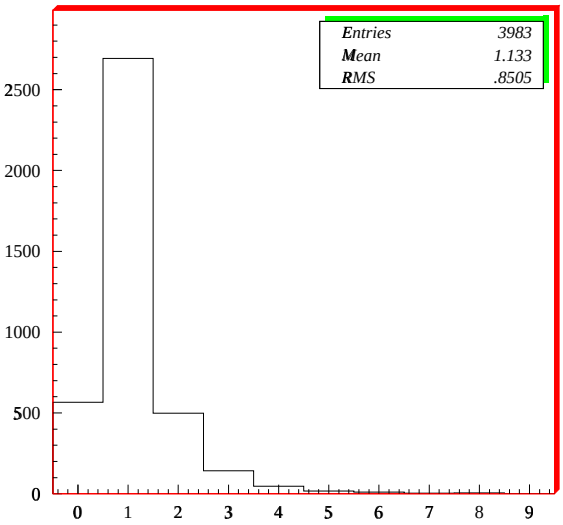

Figure 7.3: Number of good candidates found per predicted track for category 1 and 2 tracks of CS scanning of period 11 of 1995 data for stack 4 at Nagoya.

But by construction

$$N(0) = N'(0) + \sum_k X(0 \to k) \tag{7.4}$$

which, using (7.3), is equivalent to

$$N(0) = \sum_{l=0}^{j/2} N'(2l) \tag{7.5}$$

Therefore the background-free scanning efficiency is

$$\epsilon_{bf} = \frac{N_{tot} - N(0)}{N_{tot}} = \frac{N_{tot} - \sum_{l=0}^{j/2} N'(2l)}{N_{tot}} \tag{7.6}$$

Uncertainties

The statistical uncertainty on the contents of each bin quantifies the error on

$$X(1 \to n) = X(0 \to (n-1)), \tag{7.7}$$

leading to an additional statistical uncertainty equal to the quadratic sum of the individual statistical uncertainties of the even bins.

Additional systematics can be induced by the scanning method, such that the safest thing to do seems to be to treat samples individually, by stack and CS period.

Efficiencies for Tracks of Categories 1 and 2				
Period and Stack	ϵ_o^{all}	ϵ_{bf}^{all}	$\epsilon_o^{max\ 121\ views}$	$\epsilon_{bf}^{max\ 121\ views}$
Period 10				
Stack 5	$86.9 \pm 0.8\%$	$76.7 \pm 1.2 \pm 1.0\%$	$83.0 \pm 2.6 \pm 0.8\%$	$74.2 \pm 2.3 \pm 1.4 \pm 1.1\%$
Stack 6	$85.1 \pm 0.6\%$	$76.2 \pm 0.8 \pm 0.7\%$	$81.6 \pm 2.2 \pm 0.7\%$	$73.8 \pm 2.0 \pm 0.9 \pm 0.8\%$
Stack 7	$86.3 \pm 0.6\%$	$77.5 \pm 0.9 \pm 0.8\%$	$83.7 \pm 2.1 \pm 0.8\%$	$75.6 \pm 1.9 \pm 1.0 \pm 0.8\%$
Stack 8	$85.1 \pm 0.7\%$	$76.7 \pm 1.0 \pm 0.9\%$	$83.4 \pm 1.2 \pm 0.8\%$	$75.7 \pm 1.1 \pm 1.0 \pm 0.9\%$
Period 11				
Stack 5	$86.3 \pm 0.7\%$	$70.8 \pm 1.0 \pm 0.8\%$	$81.8 \pm 2.8 \pm 0.8\%$	$68.5 \pm 2.3 \pm 1.1 \pm 0.9\%$
Stack 6	$84.7 \pm 0.4\%$	$71.6 \pm 0.6 \pm 0.5\%$	$84.7 \pm 0.0 \pm 0.4\%$	$71.6 \pm 0.0 \pm 0.6 \pm 0.5\%$
Stack 7	$85.7 \pm 0.5\%$	$72.6 \pm 0.7 \pm 0.6\%$	$85.7 \pm 0.0 \pm 0.5\%$	$72.6 \pm 0.0 \pm 0.7 \pm 0.6\%$
Stack 8	$83.6 \pm 0.5\%$	$70.9 \pm 0.8 \pm 0.7\%$	$83.6 \pm 0.0 \pm 0.5\%$	$70.9 \pm 0.0 \pm 0.8 \pm 0.7\%$
Total				$72.4 \pm 0.8 \pm 0.3 \pm 0.3\%$

Table 7.3: Observed and background-free Changeable Sheet scanning efficiencies for tracks of category 1 and 2 for each stack and two different periods. For period 10 a fraction of tracks was scanned in a surface of up to 169 views while for period 11 this was only done in stack 5. We have determined the results for 121 views only as explained in the text to allow comparison. Note that depending on the stack on average 10 to 15 % more views (and surface) have been scanned for period 10. The uncertainties are given in the following order: systematic due to recalculation of the result for 121 views (only for the third and fourth column), additional statistical due to the background-free scanning efficiency extraction (columns 2 and 4), and standard statistical. Uncertainties due to instability of emulsion properties, background, ... from one sheet to the other of the same stack and period are not given.

Application to Data

The aim of this study is to compare data and Monte-Carlo to evaluate and understand possible systematic errors caused by the imperfection of the Chorus simulation. We have therefore applied the unfolding method to two different datasamples themselves divided in various categories. Unfortunately the datasamples do not satisfy all the conditions so that an additional uncertainty degrades the obtained results.

The datasamples selected correspond to scanning of Changeable Sheets exposed during periods 10 (June 14th to July 26th 1995) and 11 (July 26th to October 11th 1995) which had significantly different exposure times leading us to expect a different background density. Part[4] of the tracks scanned in these samples have been scanned with up to 13×13 *microscope views* or $1560 \times 1170\ \mu m^2$. To be able to compare we have recalculated the results in two ways: first using only the tracks which have been scanned with the standard maximum 11×11 *microscope views*, then by setting all tracks for which more than 121 views were scanned to "not found". The first method overestimates the efficiency since it does not take into account tracks which were not found after 121 views, while the second underestimates the efficiency since scanning is allowed to proceed even if a candidate with angular match in the window $6\ mrad < \Delta\theta < 15\ mrad$ has been found.

[4]To be precise, this affects a fraction of tracks of all stacks in period 10 but only stack 1 in period 11.

Efficiencies for Tracks of Categories 3 and 4				
Period and Stack	ϵ_o^{all}	ϵ_{bf}^{all}	$\epsilon_o^{max\ 121\ views}$	$\epsilon_{bf}^{max\ 121\ views}$
Period 10				
Stack 5	$75.3 \pm 1.7\%$	$68.0 \pm 2.2 \pm 1.8\%$	$71.6 \pm 2.5 \pm 0.8\%$	$65.9 \pm 2.3 \pm 1.4 \pm 1.1\%$
Stack 6	$74.8 \pm 1.1\%$	$69.2 \pm 1.4 \pm 1.1\%$	$71.4 \pm 2.0 \pm 0.7\%$	$66.9 \pm 1.9 \pm 0.9 \pm 0.8\%$
Stack 7	$75.0 \pm 1.2\%$	$72.5 \pm 1.5 \pm 1.3\%$	$72.3 \pm 2.2 \pm 0.8\%$	$66.2 \pm 2.1 \pm 1.0 \pm 0.8\%$
Stack 8	$75.4 \pm 1.3\%$	$69.2 \pm 1.7 \pm 1.4\%$	$72.9 \pm 1.5 \pm 0.8\%$	$67.4 \pm 1.4 \pm 1.0 \pm 0.9\%$
Period 11				
Stack 5	$77.2 \pm 1.3\%$	$67.9 \pm 1.7 \pm 1.4\%$	$74.0 \pm 1.7 \pm 0.8\%$	$65.6 \pm 1.4 \pm 1.1 \pm 0.9\%$
Stack 6	$76.1 \pm 0.8\%$	$66.1 \pm 1.0 \pm 0.8\%$	$76.1 \pm 0.0 \pm 0.8\%$	$66.1 \pm 0.0 \pm 1.0 \pm 0.8\%$
Stack 7	$72.3 \pm 0.9\%$	$64.4 \pm 1.2 \pm 0.9\%$	$72.3 \pm 0.0 \pm 0.9\%$	$64.4 \pm 0.0 \pm 1.2 \pm 0.9\%$
Stack 8	$73.2 \pm 0.9\%$	$64.4 \pm 1.3 \pm 0.9\%$	$73.2 \pm 0.0 \pm 0.9\%$	$64.4 \pm 0.0 \pm 1.3 \pm 0.9\%$
Total				$65.6 \pm 0.7 \pm 0.5 \pm 0.4\%$

Table 7.4: Observed and background-free scanning efficiencies for tracks of categories 3 and 4. The same comments as those given for table 7.3 apply.

We have then taken the average of the two and assigned a systematic uncertainty equal to one quarter of the difference between the two results.

These tracks have all been scanned with the microscope spiraling outward from the prediction point and stopping as soon as a good candidate (angular difference < 6 *mrad*) was found, which introduces a bias towards overestimating the background-free scanning efficiency (since other matching candidates are not found). A small test performed with the scanning apparatus at CERN on a 1995 Changeable Sheet shows [Van97b] this effect could be as high as 5 %. Of course the magnitude of the bias depends on the background density.

The results obtained for tracks of categories 1 and 2 are given in table 7.3. We see that although the observed scanning efficiencies are in very good agreement between the two periods, the background-free scanning efficiency is systematically lower for period 11, indicating a larger contribution of random background to the observed efficiency. This is not entirely unexpected as period 11 is nearly twice as long as period 10. It should be noted that on average 10 to 15 % more views were scanned for period 10 which fits the observation of a slightly higher background-free scanning efficiency.

Surprisingly enough, we do not see any target stack dependence of the efficiency, which means that either the effect of the different tracking and acceptance situation of each stack is negligible, or it is counterbalanced by some other effect. The results from simulation should give an answer to this question.

Table 7.4 gives the results for tracks of categories 3 and 4. The same comments apply here too and we only have to add that the average number of views scanned is 8 % higher than for category 1 and 2 tracks.

On the other hand for tracks of category 7 a clear stack dependence is visible as is clear from table 7.5. Here also, the average surface scanned has increased by 7 % with respect to category 3 and 4 tracks.

Efficiencies for Tracks of Category 7				
Period and Stack	ϵ_o^{all}	ϵ_{bf}^{all}	$\epsilon_o^{max\ 121\ views}$	$\epsilon_{bf}^{max\ 121\ views}$
Period 10				
Stack 5	$79.5 \pm 1.5\%$	$60.7 \pm 2.3 \pm 1.8\%$	$75.9 \pm 2.3 \pm 1.6\%$	$58.6 \pm 1.8 \pm 2.4 \pm 1.8\%$
Stack 6	$68.3 \pm 1.1\%$	$54.5 \pm 1.5 \pm 1.1\%$	$64.7 \pm 2.2 \pm 1.1\%$	$53.1 \pm 1.8 \pm 1.6 \pm 1.1\%$
Stack 7	$55.1 \pm 0.9\%$	$44.9 \pm 1.4 \pm 0.9\%$	$47.3 \pm 3.0 \pm 0.9\%$	$38.3 \pm 2.4 \pm 1.5 \pm 0.9\%$
Stack 8	$53.6 \pm 0.9\%$	$45.9 \pm 1.3 \pm 0.9\%$	$52.3 \pm 1.0 \pm 0.9\%$	$45.0 \pm 0.8 \pm 1.3 \pm 0.8\%$
Period 11				
Stack 5	$81.1 \pm 1.1\%$	$61.5 \pm 1.8 \pm 1.4\%$	$75.3 \pm 3.4 \pm 1.4\%$	$57.5 \pm 2.6 \pm 2.0 \pm 1.4\%$
Stack 6	$73.6 \pm 0.8\%$	$54.4 \pm 1.2 \pm 0.9\%$	$73.6 \pm 0.0 \pm 0.8\%$	$54.4 \pm 0.0 \pm 1.2 \pm 0.9\%$
Stack 7	$63.1 \pm 0.7\%$	$48.5 \pm 1.0 \pm 0.7\%$	$63.1 \pm 0.0 \pm 0.7\%$	$48.5 \pm 0.0 \pm 1.0 \pm 0.7\%$
Stack 8	$59.6 \pm 0.6\%$	$46.1 \pm 0.9 \pm 0.6\%$	$59.6 \pm 0.0 \pm 0.6\%$	$46.1 \pm 0.0 \pm 0.9 \pm 0.6\%$
Total				$48.1 \pm 0.7 \pm 0.5 \pm 0.4\%$

Table 7.5: Observed and background-free scanning efficiencies for tracks of category 7. The same comments as those given for table 7.3 apply.

7.2.4 Study of the Changeable Sheet Scanning Efficiency for Simulated Events

In the simulated Chorus data emulsion "hits" are stored at every change of volume (i.e. 4 points per sheet: entrance point, entrance in the plastic base, exit from the plastic base and exit point - see figure 7.1) such that we can emulate the scanning procedure by looking for a track segment in the sheet satisfying the scanning criteria.

We have set the following criteria to accept a track as "found":

- At least 4 hits have to have been stored: less than 4 hits can only be obtained if the particle disappeared due to interaction, very low energy or exit at the edge. These segments would either not be found or not reconstructed (for the low energy particles).
- The microscope efficiency is parametrized using the function

$$\epsilon_{NTS} = 0.997 - 0.07\ \theta^2_{TT\ axis} \tag{7.8}$$

Note that background is not simulated, so comparison with data has to be made with the background-free scanning efficiency extracted in section 7.2.3.

For tracks of categories 1 and 2, the only channels with a significant contribution to the sample are ν_μ-induced deep inelastic and quasi-elastic charged-current interactions. To compute the correct number for later comparison with data we use

$$\epsilon^{121\ views}_{Genima-All} = \tag{7.9}$$
$$\frac{\left(\frac{category\ 1\ and\ 2\ tracks}{reconstructed\ events}\right)_{DIS} \epsilon^{121\ views}_{Genima-DIS} + \left(\frac{category\ 1\ and\ 2\ tracks}{reconstructed\ events}\right)_{QE} \epsilon^{121\ views}_{Genima-QE} \left\langle \frac{\sigma_{QE}}{\sigma_{DIS}} \right\rangle}{\left(\frac{category\ 1\ and\ 2\ tracks}{reconstructed\ events}\right)_{DIS} + \left(\frac{category\ 1\ and\ 2\ tracks}{reconstructed\ events}\right)_{QE} \left\langle \frac{\sigma_{QE}}{\sigma_{DIS}} \right\rangle}$$

where σ_{QE} and σ_{DIS} represent the quasi-elastic and deep inelastic ν_μ charged-current interaction cross sections respectively. Following S. Ricciardi's recommendation [Ric97] we

Stack	$\epsilon^{121\ views}_{Genima-DIS}$	$\epsilon^{121\ views}_{Genima-QE}$	$\epsilon^{121\ views}_{Genima-All}$
1	$88.4 \pm 0.8\%$	$87.1 \pm 1.8\%$	$88.3 \pm 0.9\%$
2	$84.1 \pm 0.8\%$	$81.5 \pm 1.9\%$	$83.8 \pm 0.9\%$
3	$77.4 \pm 1.0\%$	$79.8 \pm 2.0\%$	$77.7 \pm 1.1\%$
4	$71.8 \pm 1.0\%$	$79.0 \pm 2.1\%$	$72.5 \pm 1.1\%$
Total	$80.2 \pm 0.5\%$	$81.7 \pm 1.0\%$	$80.4 \pm 0.6\%$

Table 7.6: Changeable Sheet scanning efficiencies for tracks of category 1 and 2 as obtained by Genima for simulated deep inelastic scattering (DIS) and quasi-elastic (QE) events.

take for the flux-weighted cross section ratio

$$\left\langle \frac{\sigma_{QE}}{\sigma_{DIS}} \right\rangle = 0.085 \tag{7.10}$$

The results obtained for tracks of categories 1 and 2 are given in table 7.6. The results exhibit a clear stack dependence which is more pronounced in the DIS than in the QE sample. This is really not very surprising since we expect events to "migrate" downstream because of reconstruction inefficiencies and not upstream. The steady increase in material upstream of each of the stacks then naturally explains the gradually lower efficiency since a larger fraction of the events did not occur in the stack. Excluding events that do not originate in any of the target emulsion stacks, we find 94.4, 91.8, 86.9, and 80.4 % scanning efficiency for category 1 and 2 tracks from deep inelastic scattering (DIS) events, but even if we only consider events originating in stack 4 this efficiency is just 80.5 %, such that a different explanation has to be found for the dominant cause of efficiency dropoff versus stack number.

Further investigation shows that the efficiency for stack 4 drops off much more at high $y_{Björken}$ than the efficiency in stack 1 (figure 7.4). Another plausible explanation for the dropoff then comes to mind: as the energy transfer to the nucleon (and y) increases, the particle multiplicity at the interaction vertex and in the trackers increases, making precise reconstruction more difficult. The presence of material "filters" a lot of lower energy particles produced thus providing a cleaner reconstruction environment downstream. Of course, the longer distance between the last tracker planes and the primary vertex also allows tracks to be separated better leading to easier reconstruction.

Simulation results for the CS scanning of tracks of categories 3 and 4 are given in table 7.7. For these tracks 3 channels contribute significantly: deep inelastic charged- and neutral current and quasi-elastic charged current scattering. The results have been combined using a formula analogous to equation 7.9. We see again a clear stack dependence but the difference between stack 1 and 2 (and 3 and 4) has disappeared. This is more than likely due to multiple scattering in the even stacks, deteriorating the prediction precision for the odd stacks. The fact that hadrons from neutral current events have lower efficiency for these stacks confirms this diagnostic.

Finally, results for category 7 tracks are given in table 7.8. The stack dependence is similar to the one observed for category 3 and 4 tracks.

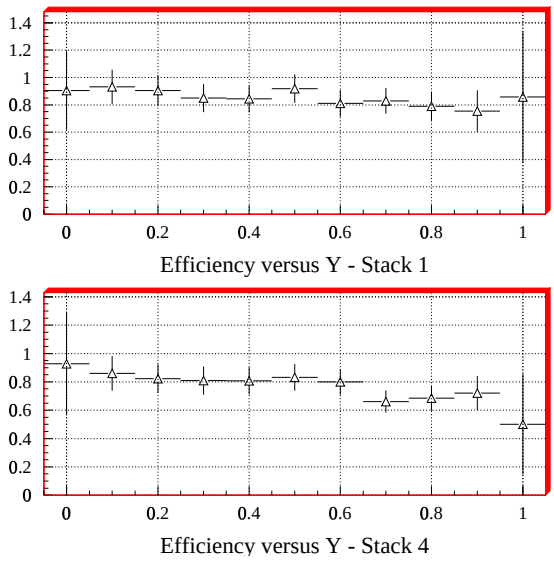

Figure 7.4: CS scanning efficiency for simulated deep inelastic ν_μ-induced charged-current events with a reconstructed muon as a function of $y = (E_\nu - E_\mu)/E_\nu$. Here E_ν and E_μ denote the neutrino and muon energies respectively.

Stack	$\epsilon^{121\ views}_{Genima-CC\ DIS}$	$\epsilon^{121\ views}_{Genima-NC\ DIS}$	$\epsilon^{121\ views}_{Genima-QE}$	$\epsilon^{121\ views}_{Genima-All}$
1	$75.8 \pm 1.6\%$	$65.6 \pm 2.6\%$	$86.8 \pm 5.5\%$	$72.9 \pm 1.9\%$
2	$75.8 \pm 1.5\%$	$67.8 \pm 2.2\%$	$86.4 \pm 5.2\%$	$73.3 \pm 1.9\%$
3	$61.5 \pm 1.6\%$	$52.0 \pm 2.1\%$	$82.4 \pm 6.5\%$	$58.1 \pm 1.8\%$
4	$58.4 \pm 1.7\%$	$55.8 \pm 1.9\%$	$65.9 \pm 7.0\%$	$57.4 \pm 1.9\%$
Total	$67.0 \pm 0.8\%$	$58.9 \pm 1.1\%$	$80.0 \pm 3.1\%$	$64.2 \pm 1.0\%$

Table 7.7: Changeable Sheet scanning efficiencies for tracks of category 3 and 4 as obtained by Genima for simulated deep inelastic scattering (DIS) charged- and neutral current and quasi-elastic (QE) events.

Stack	$\epsilon^{121\ views}_{Genima-CC\ DIS}$	$\epsilon^{121\ views}_{Genima-NC\ DIS}$	$\epsilon^{121\ views}_{Genima-QE}$	$\epsilon^{121\ views}_{Genima-All}$
1	$73.9 \pm 1.6\%$	$72.3 \pm 4.5\%$	$80.3 \pm 3.2\%$	$74.3 \pm 2.0\%$
2	$74.0 \pm 1.6\%$	$65.2 \pm 4.1\%$	$80.0 \pm 3.2\%$	$73.4 \pm 2.1\%$
3	$60.7 \pm 1.7\%$	$44.2 \pm 4.1\%$	$82.0 \pm 3.3\%$	$59.8 \pm 2.1\%$
4	$63.3 \pm 1.7\%$	$42.6 \pm 3.4\%$	$80.5 \pm 3.2\%$	$60.6 \pm 2.1\%$
Total	$67.8 \pm 0.8\%$	$53.0 \pm 2.0\%$	$80.4 \pm 1.6\%$	$66.7 \pm 1.0\%$

Table 7.8: Changeable Sheet scanning efficiencies for tracks of category 7 as obtained by Genima for simulated deep inelastic scattering (DIS) charged- (CC) and neutral (NC) current and quasi-elastic (QE) charged-current events.

7.2.5 Comments on the Discrepancy Between Data and Monte-Carlo Scanning Efficiencies

The purpose of this work is not to rewrite the Chorus detector simulation. However, this study can try to give indications as to the origin of the discrepancy between the results obtained for data and simulation.

As can be seen from table 7.3 to 7.8, the points of disagreement between data and Monte Carlo are:

- For categories 1 and 2, the stacks dependence of the Monte Carlo results is not observed in the data. The efficiency agrees for stack 4 but Monte-Carlo is more and more optimistic as we go upstream.

- For categories 3 and 4, the difference between the two modules is not seen in the data and the averages seem to roughly match.

- Category 7 presents a stack dependence in the data as well as Monte-Carlo. The Monte-Carlo efficiencies are however significantly high.

Another striking disagreement between data and simulation is the fraction of tracks predicted in each stack. For tracks of category 1 and 2 in simulated events we find 23.0 %, 26.2 %, 24.3 % and 26.5 % of the tracks predicted in stacks 1 to 4 respectively, while in the data we see 27.4 %, 26.2 %, 25.1 % and 21.3 % respectively. For categories 3 and 4 the Monte Carlo predicts 19.2 %, 23.6 %, 27.1 % and 30.1 % while data has 24.3 %, 27.8 %, 24.7 % and 23.2 %. The statistical error on each of these numbers is of the order of 1 % for data categories 1 and 2, 1.5 % for data categories 3 and 4 and 2 % for the Monte Carlo.

A possible explanation of all these results is that the long time window of the trackers (15 μs gate and "slow" phosphor), which is not considered by the Chorus detector simulation, leads to the detection of a lot of noise. The noise causes the upstream migration of events, populating the upstream stacks with predictions for events which either have their origin somewhere downstream (tracker planes for example), or are due to a "cosmic muon" satisfying the trigger conditions. This could explain the distributions of predictions in the various stacks as well as the low efficiency found in the data for the upstream stacks since the denominator of the efficiency calculation is then higher.

7.2.6 Special Sheet Scanning Efficiency

Unfortunately the 1995 Special Sheets (these sheets are located inside each target emulsion module's vacuum packing and cannot be changed during the exposure) suffered from emulsion thickness problems. A lot of the sheets have too thin emulsion layers (30 μm) leading to the apparition of many fake candidates which do not correspond to background tracks but just random associations (the minimal required track length has to be reduced). Our background-free scanning efficiency extraction method can therefore not be used.

But once a track has been found in the Changeable Sheets, there are only two reasons why it would not be found in the Special Sheets. Either the particle has undergone an interaction or decay between the two sheets, and this should be simulated with good accuracy, or the track is not visible due to emulsion quality problems or the microscope efficiency. As for the Changeable Sheets, we also simulate the microscope efficiency so we can assume our results are fairly reliable.

Event Type	Stack 1	Stack 2	Stack 3	Stack 4	All
ν_μ^{CC-DIS}	31.7 %	34.2 %	30.7 %	28.6 %	$31.3 \pm 0.3\%$
ν_μ^{CC-QE}	41.2 %	44.5 %	41.8 %	39.1 %	$41.6 \pm 0.8\%$
ν_μ^{NC-DIS}	11.2 %	16.5 %	15.9 %	21.0 %	$16.2 \pm 2.2\%$
$\nu_\tau^{CC-DIS}, \tau^- \to \mu^- \ldots$	30.9 %	32.6 %	30.0 %	28.5 %	$30.5 \pm 0.3\%$
$\nu_\tau^{CC-QE}, \tau^- \to \mu^- \ldots$	37.0 %	41.6 %	38.0 %	37.1 %	$38.4 \pm 0.5\%$
$\nu_\tau^{CC-DIS}, \tau^- \to 0\mu^- \ldots$	17.8 %	28.6 %	21.8 %	30.7 %	$24.8 \pm 0.3\%$
$\nu_\tau^{CC-QE}, \tau^- \to 0\mu^- \ldots$	11.8 %	17.7 %	14.0 %	24.0 %	$17.0 \pm 0.5\%$

Table 7.9: Fraction of generated events that are found up to the Special Sheet for the different event types. These results take into account the scanning selection cuts (momentum, X7), fiducial volume cuts and the scanning efficiency. The statistical uncertainty is given for the global (all stacks) result.

Furthermore, losses due to emulsion quality would concern a fraction of events, such that these cancel out perfectly[5] when taking the ratio of SS scanning efficiencies for different channels.

Overall the Special Sheet scanning efficiency is 89 % for ν_μ-induced deep inelastic charged-current interactions for example (with only a small dependence on track type and none on stack number) while the observed efficiency is 93.7 % in the 1995 data.

7.2.7 Changeable and Special Sheet Combined Results

The event finding efficiency up to the Special Sheet for the different event types is given in table 7.9. This efficiency includes all selection cuts (charge, momentum, ...) and is defined by the number of found events divided by the number of generated events in each emulsion stack.

7.3 Target Emulsion Scanning

7.3.1 Description of the Target Plates

The target emulsion has been optimized to offer as much active material (i.e. emulsion) as possible and minimize the dead volumes (i.e. emulsion support base). This led Chorus to choose a 100 μm thick transparent base coated with two layers of 350 μm of emulsion, thickness which is essentially limited by visibility requirements for the microscopes.

36 plates are superposed in a "tower" to form a full target thickness of about 2.9 cm, or 3.0 cm if we count the Special Sheet which is contained in the same vacuum packing. The transverse size of the plates is again 35×70 cm^2, but only a surface of 32×32 cm^2 is scanned (as for the SS) in each half plate.

The major disadvantage of the thick emulsion layers resides in their distortion during development. While the emulsion closest to the base remains in place, shifts can occur with increasing magnitude as the distance from the base increases, such that an originally straight track takes on a different shape. These effects are strongest near the edges, but can generally be well parametrized with a parabolic fit further inside. Fits generally assume that

[5] This only applies of course for tracks which leave similar signal in the emulsion, but since the tracks sent to scanning are by definition minimum ionizing this is true for our application.

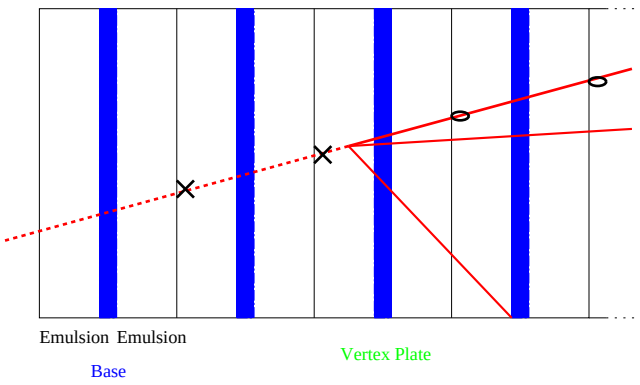

Figure 7.5: Vertex Plate search: the scan-back track is followed upstream by scanning the upstream 100 μm of each target emulsion plate. When the track is not found in two consecutive plates (crosses) the first of those two is called the Vertex Plate (VP).

the track slope has not been affected close to the surface of the emulsion (points furthest from the base) and the points very close to the base are in the original position.

7.3.2 Vertex Plate Determination

Of course we want to use the Track Selector (automatic microscope) to identify the plate with the primary (or secondary) vertex. Unfortunately, it is a hardware device which is explicitely built to scan a 100 μm emulsion layer at the emulsion surface. Therefore we don't follow the scan-back track upstream continuously (since this would require semi-automatic scanning), but sample the upstream 100 μm of each successive target emulsion plate until the track does not appear in 2 consecutive plates. This method is shown schematically in figure 7.5. The track impact point prediction in each plate is made using the angle measured in the Special Sheet and the impact point found in the previous plate. The scanning tolerances are given in table 7.1.

By defining that the Vertex Plate found is correct if it either contains the primary and/or secondary vertex or is upstream from the secondary vertex (for tau decays), we can evaluate the "Vertex Plate Efficiency" for different event types. In addition to the track selector efficiency (equation 7.8) and the requirement to have at least 4 hits, there is a random 2 % probability to lose the track due to visibility and other emulsion effects and the track penetration in the scanned 100 μm has to be taken into account. This is done by reproducing the pulse height distribution measured by the Track Selector for through-going tracks (figure 7.6), scaled by a factor

$$Scale factor = \frac{Distance\ spanned\ by\ track\ in\ 100\ \mu m}{100\ \mu m} \tag{7.11}$$

A track is accepted if it has a pulse height greater than or equal to 12.

The results obtained for the different types of events are summarized in table 7.10 for all stacks. The higher efficiency observed for ν_τ-induced events is easily explained by the possible presence of two vertex plates (the plate with the primary vertex is not necessarily the plate with the secondary vertex).

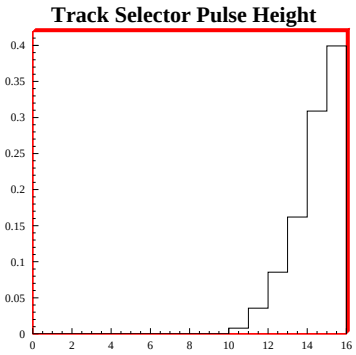

Figure 7.6: Pulse Height measured by the Track Selector for through-going tracks.

Event Type	Stack 1	Stack 2	Stack 3	Stack 4	All
ν_μ^{CC-DIS}	88.9 %	88.7 %	88.9 %	88.7 %	88.8 %
ν_μ^{CC-QE}	89.3 %	86.6 %	88.4 %	87.7 %	88.0 %
ν_μ^{NC-DIS}	84.6 %	81.4 %	82.6 %	78.2 %	81.0 %
$\nu_\tau^{CC-DIS}, \tau^- \to \mu^- \ldots$	92.8 %	92.0 %	91.7 %	90.4 %	91.7 %
$\nu_\tau^{CC-QE}, \tau^- \to \mu^- \ldots$	92.1 %	92.7 %	91.5 %	92.0 %	92.1 %
$\nu_\tau^{CC-DIS}, \tau^- \to 0\mu^- \ldots$	88.0 %	85.3 %	87.7 %	83.2 %	85.6 %
$\nu_\tau^{CC-QE}, \tau^- \to 0\mu^- \ldots$	91.6 %	82.3 %	88.7 %	84.8 %	86.1 %

Table 7.10: Fraction of events found in the Special Sheet for which the correct vertex plate (as defined in the text) was found.

7.3.3 Kink Search

Since we are not following the track continuously but only sampling it every 800 μm, various topologies are possible which all require specific kink search methods. These methods are still being developed such that in the real data we have many samples treated with slightly different methods. We will describe each of the methods here as well as the simulation status.

Note that to be accepted as a tau candidate, the track flight length always has to be larger than 20 μm and the decay kink angle larger than 10 milliradians.

Short Decays

Once the Vertex Plate has been found, we search for the other tracks composing the vertex reconstructed using the trackers (if such tracks exist). The search window is defined by the tracks angles reconstructed by the trackers and the assumption that the vertex is in the Vertex Plate. The method is explained schematically in figure 7.7. From each combination of two additional track segments found in the plate just downstream the V.P. we reconstruct a primary vertex position. We then compute the impact parameter of the scan-back track with respect to each computed vertex and keep the smallest found value. In the case we only find one additional track, the distance of closest approach between this track and the scan-back track is taken as impact parameter value. If the impact parameter exceeds the

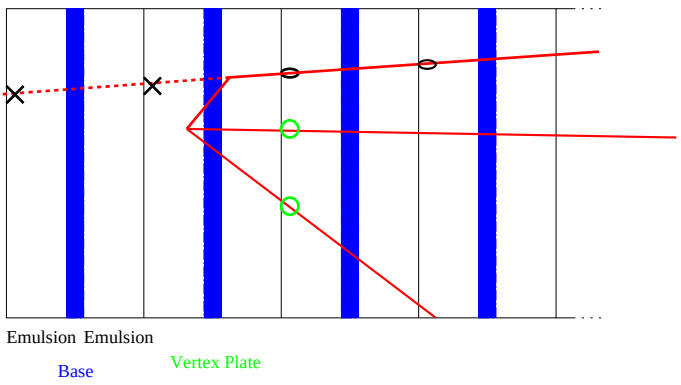

Figure 7.7: Schematic drawing of short decay search using the impact parameter technique.

cut

$$I.P. > 2. + 0.006 \times (computed\ vertex\ depth)\ \mu m \tag{7.12}$$

the event is sent to manual scan to confirm or refute the presence of a decay kink.

As can be seen from figure 7.8, the cut has been defined to reject most of the data events and keep the manual scanning load at an affordable level. The presence of an impact parameter for events without decay kinks is very well reproduced in the simulation after inclusion of a 5 mrad smearing of the angular measurements in the target emulsion.

The recent improvement of the angular accuracy for target emulsion track measurement will lead to a small change in strategy for this method. Indeed, in the future it will be sufficient that the impact parameter w.r.t. to any vertex constructed from a combination of two tracks exceeds the cut, while now if any of these values is below the cut the event is discarded.

Long, Small Angle Decays

Another possible configuration is shown in figure 7.9. Here the decay kink is in a plate downstream from the primary vertex plate but the kink angle is still small enough to identify the primary vertex plate as VP. To test the long, small angle hypothesis the scan-back track angle is compared with the angle measured in the Special Sheet, and if the transverse momentum corresponding to this angular difference exceeds 250 MeV/c the track is manually followed dowstream for 5 plates in search of a decay kink. Again, the transverse momentum distribution observed is well reproduced in the simulation after imposing a 5 mrad resolution to the target emulsion angular measurement. The Monte-Carlo distributions for ν_μ^{CC} and tau decays are shown in figure 7.10

Long, Large Angle Decays

Of course, if the kink angle is large enough the vertex plate is the plate with the tau decay. Since this plate does not contain the primary vertex, we will not find any additional tracks predicted by the trackers such that the impact parameter method is excluded. This is shown schematically in figure 7.11. Note that all events for which no additional tracks could be found either due to mediocre reconstruction or physics (quasi-elastic events) enter this class too.

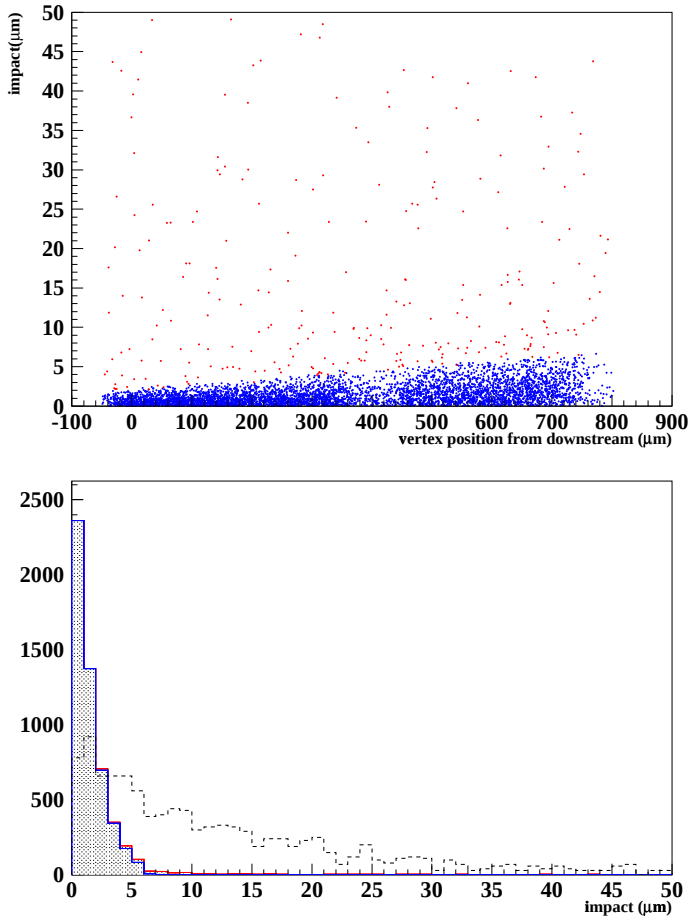

Figure 7.8: Top: Impact parameter versus computed vertex depth for data events. This distribution is fairly well reproduced in the simulation after inclusion of a 5 mrad angular measurement uncertainty. Bottom: Impact parameter for data (shaded) and $\nu_\tau^{CC}, \tau^- \rightarrow \mu^- \overline{\nu_\mu} \nu_\tau$ events (dashed).

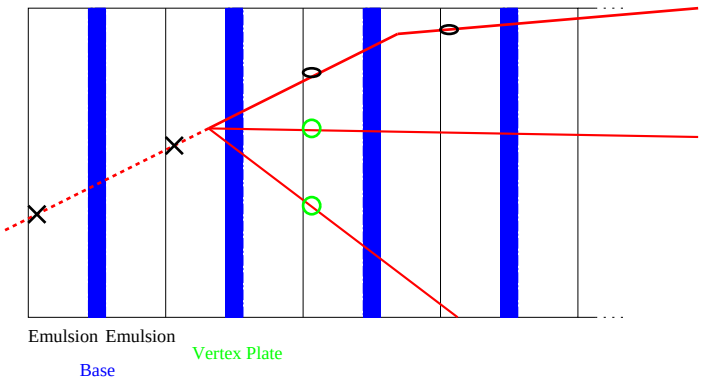

Figure 7.9: Schematic drawing of long decay search using the transverse momentum technique.

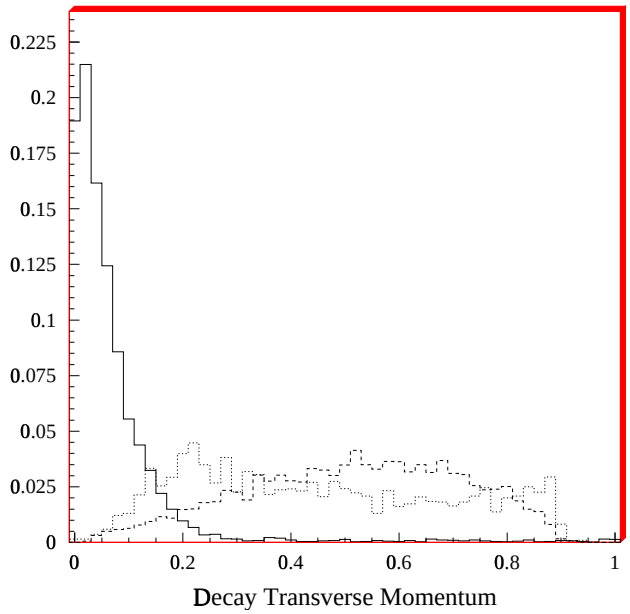

Figure 7.10: Transverse momentum distributions (in MeV) obtained from comparison of the target and Special Sheet track angles for simulated ν_μ^{CC} events (solid line), ν_τ^{CC} events with muonic tau decay (dashed line) and ν_τ^{CC} events with non-muonic tau decay (dotted line).

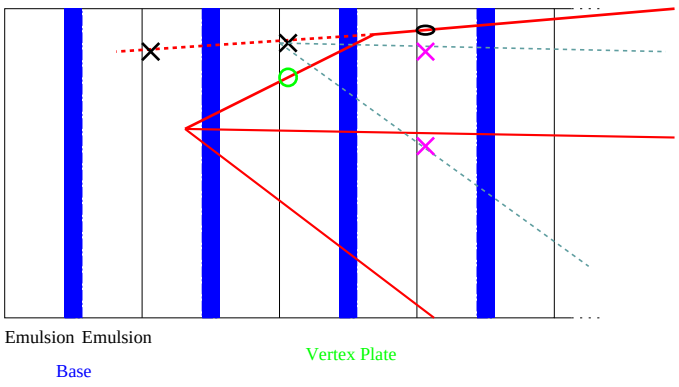

Figure 7.11: Schematic drawing of long decay search using the Parent Track Search technique.

Event Type	P.T.S. Only	P.T.S., I.P. and p^T
$\nu_\tau^{CC-DIS}, \tau^- \to \mu^- \ldots$	$29.8 \pm 0.7\%$	$43.2 \pm 0.7\%$
$\nu_\tau^{CC-QE}, \tau^- \to \mu^- \ldots$	$27.4 \pm 0.7\%$	$30.6 \pm 0.8\%$
$\nu_\tau^{CC-DIS}, \tau^- \to 0\mu^- \ldots$	$8.2 \pm 0.5\%$	$14.8 \pm 0.6\%$
$\nu_\tau^{CC-QE}, \tau^- \to 0\mu^- \ldots$	$14.1 \pm 1.3\%$	$18.3 \pm 1.5\%$

Table 7.11: Kink finding efficiencies for the different tau decay channels using only the Parent Track Search method, or P.T.S., impact parameter (I.P.) and transverse momentum (p^T). This number includes the efficiency for the scan-back track to be the tau daughter.

Two different methods have been applied to this class of events: the video image approach and the Parent Track Search.

The Parent Track Search consists in looking for a potential parent track in the upstream surface of the vertex plate. If a track is found which has a closest distance of approach to the scan-back track of less than $15\mu m$, and if the closest approach point satisfies

$$-1140\ \mu m < zvertex < 300\ \mu m \quad if \quad 0.02\ rad < \Delta\theta < 0.075\ rad \tag{7.13}$$

$$-940\ \mu m < zvertex < 100\ \mu m \quad if \quad 0.075\ rad < \Delta\theta \tag{7.14}$$

then the event is sent to manual check. Here $zvertex$ is the position of closest approach of the two tracks with respect to the upstream surface of the plate downstream of the vertex plate, and $\Delta\theta$ is the angular difference between the two tracks.

The video image approach consists in digitizing a three dimensional volume covering the full depth of the vertex plate and centered on the impact point of the scan-back track in the support base of this plate. The Track Selector is used to make the digitization, recording images at 48 depths on each side of the base. These images are therefore spaced by about 7 μm in beam direction, with a focal depth of about $6\mu m$. The transverse size of each image is approximatively $150 \times 130\mu m$. This video image is then analyzed offline by an "image analysis" program.

So far, this approach has only been used for a limited sample of 1994 data, but the scanning group at CERN plans to use a similar approach for all its target scanning. We have therefore developed a simulation program which adds grains corresponding to simulated tracks into a video image taken at a random place in the emulsion (an "empty image", containing only background). This program will be used to determine and improve the image analysis program efficiency in the future. It is described in the next section.

Before that, table 7.11 summarizes the kink finding efficiencies using only the Parent Track Search approach (as for 1995 data so far), and the combination of P.T.S., impact parameter and transverse momentum. The results are significantly lower for the non-muonic decay channels partly because these values include the requirement that the scan-back track be a tau daughter. This is nearly always true for the muonic tau decays but much less of course for the other decays.

7.4 Video Image Simulation

The simulation of video images is essential to the development and determination of the efficiency of the image analysis programs which will be used intensively in the future at CERN. We have developed a simulation program which adds grains from simulated tracks

in "empty images" recorded at a random place in the emulsion such that they contain only background.

7.4.1 Program flow

The program flow is illustrated in figure 7.12. Details for each step are given in section 7.4.3, but the figure shows the relations between the various steps. It also shows which parts of the program are written in Fortran and which parts are written in C++.

Two input streams are optional: images can be simulated without knowledge of scanning predictions (but biases are difficult to evaluate - see section 7.4.3), or CS, SS, target scanning and kink finding efficiencies can be evaluated without producing video images (this is what has been done in sections 7.2 and 7.3).

7.4.2 Empty Images

A "video image" is a digitization of an emulsion volume using the Track Selector hardware: for each side of the target emulsion plate, "photographs" are made with the microscope focused at 48 different depths of the emulsion layer (which means one photograph approximatively every 7 μm in real space since one undeveloped emulsion layer is about 350 μm). The microscope has a focal depth of about 3 μm, or 6 μm in real space (since development shrinks the emulsion by a factor close to 2), such that essentially the whole emulsion volume is digitized. The total of 96 views covers a volume of about 150 (horizontal) x 130 (vertical) x 790 (along the beam) μm^3. From now on, the term "layer" will be used for a single "photograph": one image has 96 layers, 48 on each of the two "sides" of the base.

Empty images are video images which have been recorded at some arbitrary place in the target emulsion. They only contain random background and no neutrino vertex.

7.4.3 Simulation Steps

The Changeable, Special and Target Sheet scanning simulation has already been detailed (sections 7.2 and 7.3), so we will focus here on the remaining steps.

Extraction of Simulation Parameters

A simple version of the image analysis program is used to perform elementary clustering and tracking on the empty image to extract the following parameters:

- The grain density: in fact, in the video image the grain density does not have the usual meaning (number of grains per 100 μm). This is of course due to the intrinsic nature of the image where grains can overlap in one layer and be seen as 1 cluster only. The best way to tackle the problem seemed to be to count the "layer density" (LD), which is defined by

$$LD = < \frac{Number\ of\ layers\ in\ which\ a\ cluster\ is\ present}{Number\ of\ layers\ spanned\ by\ the\ track} >_{all\ tracks\ in\ 1\ side} \tag{7.15}$$

  Experimentally, the layer density value varies between 75 and 95 % and is usually identical to within a few percent for the 2 sides of one images, indicating this is really a property of the emulsion and the image recording conditions. For the simulated

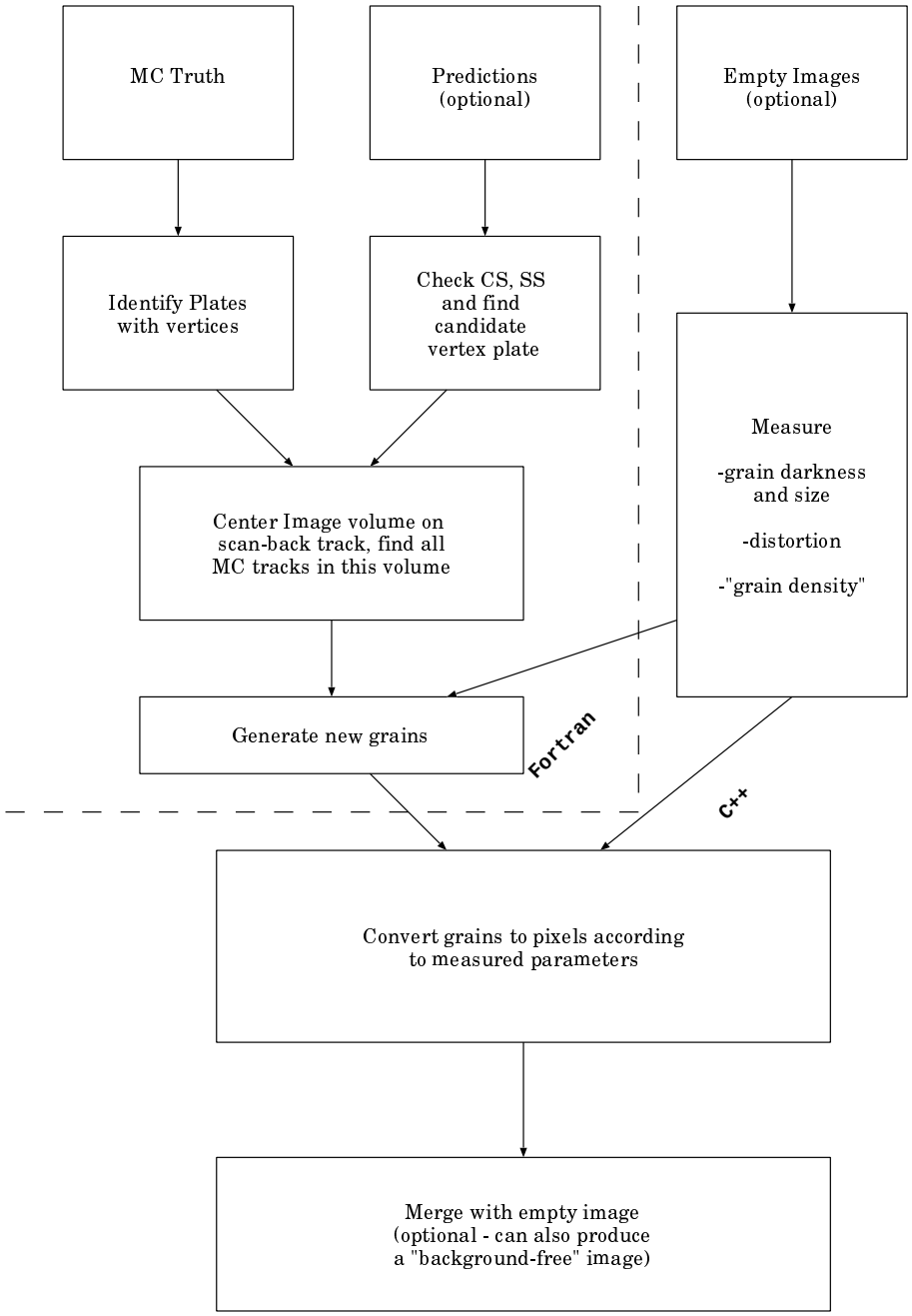

Figure 7.12: Program flow: the steps are described in more detail in section 7.4.3. Items on the left/up side of the dashed line are in Fortran77, items on the right/down side are in C++.

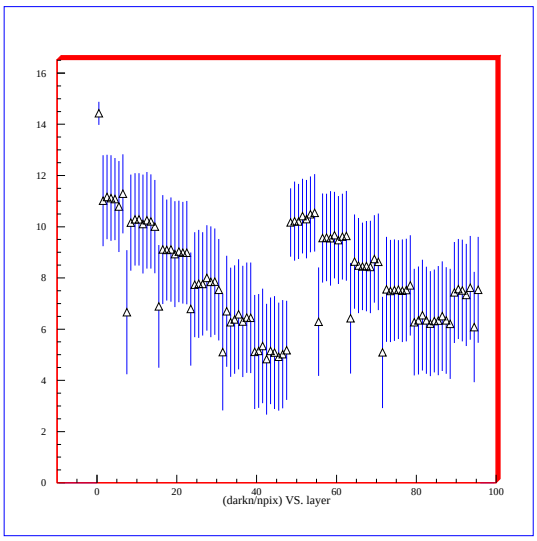

Figure 7.13: Average pixel pulse height in grains in function of layer number. Layer 1 is upstream w.r.t. the neutrino beam.

tracks, the layer density determines the fraction of layers in which simulated clusters will be added. These are chosen at random according to a flat distribution.

- Grain size and "darkness": in the image grains (or superpositions of grains) appear as clusters of pixels. For all the grains in the tracks, the number of pixels per cluster and their pulse height ("darkness") distribution is measured. Whereas the number of pixels per cluster is nearly independent of the depth (as you would expect: grains have the same size in all layers), the pulse height is more of a measure of contrast and varies significantly with depth as can be seen in figure 7.13.

  Both the grain size (i.e. the number of pixels) and the darkness for each pixel are generated according to the measured distributions, with the darkness depending on the layer.

- The distortion due to emulsion development can be measured if enough background tracks are found. This is generally the case and unless the image is located close to the physical edge of the emulsion a parabolic fit to the (originally straight) tracks fits fairly well. In this way, the distortion can also be applied to the simulated tracks. This feature, although foreseen, is not implemented yet.

Image Centering

The image is centered according to the procedure followed in Nagoya: the expected position of the scan-back track at each side of the base is computed, and these positions are used as center to take the image. This means the microscope stage doesn't move transversely while taking the image of one side, but it moves before taking the other side (the amount of movement is determined by the angle of the scan-back track).

With the center known, the image volume is determined by the scanning area of $156 \times 129 \mu m^2$ and the full depth of the target plate. In the Monte-Carlo this is always 790 μm, while in real data the plate thickness is known to vary by $\approx 30 \mu m$ from plate to plate [Dil95]. But this should not have any ill effects.

Once the image volume is fully delimited, all MC tracks going through the volume are identified and kept in memory.

Grain Generation and Conversion to Pixels

Using the layer density measured in the empty image, we decide for each track segment contained in the image volume which layers will have a grain (or rather a cluster). In fact, the program decides which layers will be omitted ("not simulated") since this requires less random numbers.

After all the "simulation grains" are determined, they are converted to clusters of pixels layer-by-layer according to the measured parameters. For each grain, a number of pixels is drawn according to the measured distribution and for each pixel a darkness or pulse height is drawn using the same procedure. For the pulse-height the distribution used is layer-dependent to reproduce the real image. The pixels are arranged at the position of the grain putting the darkest pixel in the center (the grain coordinate) and the lighter pixels outward, thus creating a "pulse-height hill".

Merger with "Empty Image"

Finally, the new pixels are added to the existing image and the simulated video image is finished.

A useful option allows to produce the image with only simulated pixels, suppressing the existing background. These images make event visualisation much easier for untrained eyes (meaning eyes not trained for scanning) and should be a major help for development of image analysis programs since they provide a "background free" tracking environment.

7.4.4 Examples

Using the existing Chorus image display program [Coc97], we can look at the produced images. As an illustration, figures 7.14 and 7.15 are two images of the same event, without and with background respectively. The tracks displayed are the ones found by the simple image analysis program. Note that the centering method used was different when these images were produced.

7.5 Conclusions

We have seen that the agreement between Changeable Sheet scanning efficiencies in the simulation and in the data is not perfect. However, the stack dependence seems to point towards the presence of events in the data which are not simulated as the main source of this discrepancy. The recent observation in the data of an excess of events with low hadronic activity but the correct muon momentum spectrum could be explained by the same problem if the main contribution comes from erroneously interpreted beam muons.

This explanation could be checked by introducing the consequences of the long tracker time gate in the Chorus detector simulation. If it is correct, then the simulation of the events that have been generated in the emulsion appears to be fairly reliable, as indicated by the agreement for stack 4. We can then trust the rest of the simulation with quite some confidence and rely on the obtained results for the vertex and kink finding efficiencies.

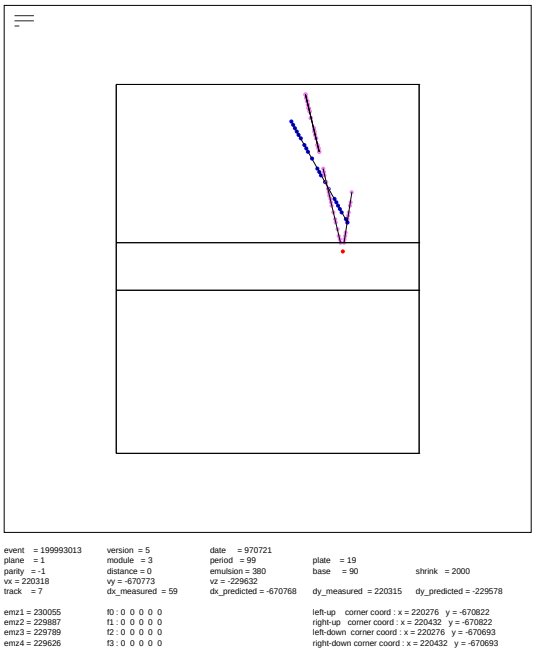

Figure 7.14: Simulated video image without background. Only found tracks are displayed.

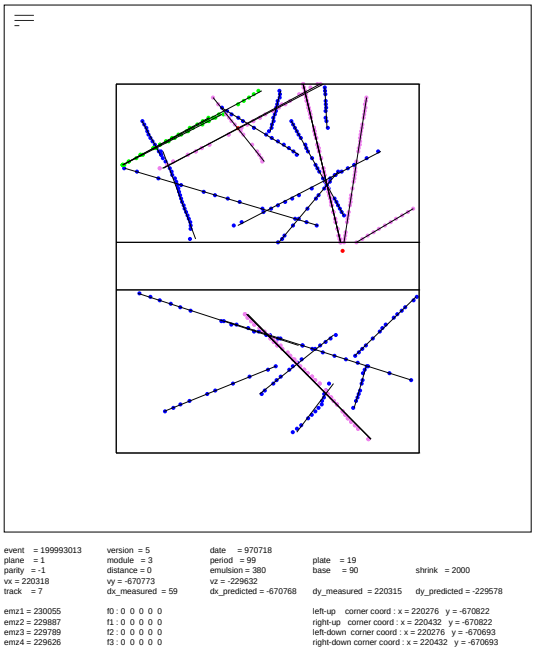

Figure 7.15: Simulated video image with background. This is the same event as the one displayed in figure 7.14.

Last but not least, the video image simulation is at a quite advanced stage and is ready to be used to develop the video image analysis program which will be used for the target emulsion scanning at CERN.

Chapter 8

A New Limit On $\nu_\mu \rightarrow \nu_\tau$ Oscillations

Using the sample of events now scanned by Chorus, combined with the efficiencies determined in the previous chapter, we can in principle set a new limit on $\nu_\mu \rightarrow \nu_\tau$ oscillations.

However, the 1994 datasample requires very special attention since many different scanning strategies were applied to various subsamples. We will apply the efficiencies determined by our Japanese colleagues for the 1994 dataset, where the steady evolution and tuning of the various approaches while scanning requires very detailed knowledge of the methods used for each sample (and even subsample).

For the 1995 dataset a single track selection algorithm was applied and only the Parent Track Search method has been used for kink search so far, but our results for the impact parameter and transverse momentum methods are valid and can be applied as soon as this stage of the scanning will have been performed.

8.1 Required Efficiencies

If the oscillation probability is small, then the number of observed ν_μ-induced events is

$$N_{\nu_\mu} = \int \Phi_\mu \sigma_\mu A_\mu dE \tag{8.1}$$

where Φ_μ is the muon neutrino flux shown in figure 4.1, σ_μ is the ν_μ interaction cross-section (charged and neutral current) and A_μ is the global Chorus efficiency to find the vertex of a event which originated in the emulsion, taking into account acceptance, cuts and reconstruction and scanning efficiencies. The integral runs over the complete neutrino spectrum.

The observed number of ν_τ-induced charged current events will be

$$N_{\nu_\tau}^{CC} = BR(\tau \rightarrow x) \int \int \Phi_\mu P \sigma_\tau^{CC} A_\tau \epsilon_{kink} dE dL \tag{8.2}$$

and here BR is the branching ratio for the considered tau decay mode, P is the oscillation probability, σ_τ^{CC} is the tau neutrino charged-current interaction cross-section and ϵ_{kink} is the kink finding efficiency. To find this value we should not only integrate over the ν_τ spectrum but also over the ν_τ flightlength (L) since the oscillation probability also depends on the latter.

In a two-family model and for large Δm^2, the ratio $N^{CC}_{\nu_\tau}/N_{\nu_\mu}$ reduces to

$$\frac{N^{CC}_{\nu_\tau}}{N_{\nu_\mu}} = \frac{1}{2} sin^2 2\theta_{\mu\tau} \frac{BR(\tau \to x) \int\int \Phi_\mu \sigma^{CC}_\tau A_\tau \epsilon_{kink} dE dL}{\int \Phi_\mu \sigma_\mu A_\mu dE} \tag{8.3}$$

because the oscillation probability becomes independent of energy and flightlength. This is equivalent to

$$\frac{N^{CC}_{\nu_\tau}}{N_{\nu_\mu}} = \frac{1}{2} sin^2 2\theta_{\mu\tau} \frac{BR(\tau \to x) \left\langle \sigma^{CC}_\tau \right\rangle \left\langle A_\tau \right\rangle \left\langle \epsilon_{kink} \right\rangle}{\left\langle \sigma_\mu \right\rangle \left\langle A_\mu \right\rangle} \tag{8.4}$$

which can be used to compute the limit for large Δm^2. To do this, $N^{CC}_{\nu_\tau}$ only has to be replaced by the upper limit on the number of signal events for Poisson processes for the chosen confidence level [PDG96]. Background and the consequences of uncertainties of course have to be taken into account.

The Δm^2 dependence of the result can then be derived using the method described by J. Brunner [Bru97b]

$$sin^2 2\theta_{\mu\tau} = \frac{1}{2} sin^2 2\theta^{\infty}_{\mu\tau} \frac{\int\int \Phi_\mu \sigma^{CC}_\tau A_\tau \epsilon_{kink} dE dL}{\int\int \Phi_\mu \sigma^{CC}_\tau A_\tau \epsilon_{kink} sin^2 \left(1.27\ L/E\ \Delta m^2\right) dE dL} \tag{8.5}$$

where $sin^2 2\theta_{\mu\tau}$ is the limit at the corresponding value of Δm^2 and $sin^2 2\theta^{\infty}_{\mu\tau}$ is the value found for large Δm^2 using equation 8.4.

This means that we only have to evaluate $sin^2 2\theta^{\infty}_{\mu\tau}$ and the energy dependence of $A_\tau \epsilon_{kink}$.

To elegantly combine the results from the muon- and muon-less samples and easily visualize the contribution of each to the limit, we can evaluate the number of "equivalent charged-current events" for the scanned neutral current events. Let us decompose equation 8.4. The contribution from the muon sample is

$$N^{CC}_{\nu_\tau}(muon) = \frac{1}{2} sin^2 2\theta_{\mu\tau} \frac{BR(\tau \to \mu^- \overline{\nu_\mu} \nu_\tau) \left\langle \sigma^{CC}_\tau \right\rangle \left\langle A^{muon}_\tau \right\rangle \left\langle \epsilon^{muon}_{kink} \right\rangle}{\left\langle \sigma^{CC}_\mu \right\rangle \left\langle A^{muon}_\mu \right\rangle} N^{muon}_{\nu_\mu} \tag{8.6}$$

where the superscripts *muon* indicate this concerns the events with an identified muon[1]. The contribution from the muon-less sample is:

$$N^{CC}_{\nu_\tau}(muon-less) = \frac{1}{2} sin^2 2\theta_{\mu\tau} \frac{BR(\tau \to 0\ \mu^-) \left\langle \sigma^{CC}_\tau \right\rangle \left\langle A^{muon-less}_\tau \right\rangle \left\langle \epsilon^{muon-less}_{kink} \right\rangle}{\left\langle \sigma^{muon-less}_\mu \right\rangle \left\langle A^{muon-less}_\mu \right\rangle} N^{muon-less}_{\nu_\mu} \tag{8.7}$$

Such that we can write

$$N^{muon-equiv}_{\nu_\mu} = N^{muon-less}_{\nu_\mu} \frac{\left\langle \sigma^{CC}_\mu \right\rangle \left\langle A^{muon}_\mu \right\rangle}{\left\langle \sigma^{NC}_\mu \right\rangle \left\langle A^{NC}_\mu \right\rangle + \left\langle \sigma^{CC}_\mu \right\rangle \left\langle A^{CC-misid}_\mu \right\rangle} \tag{8.8}$$

[1] Here we haven taken the charged-current interaction cross-section since the contribution from neutral current events to this sample is negligible.

which can be rewritten

$$N^{equiv}_{\nu_\mu - muon} = N_{\nu_\mu - muon - less} \frac{\langle \sigma^{CC}_\mu \rangle}{\langle \sigma^{NC}_\mu \rangle} \frac{\langle A^{muon}_\mu \rangle}{\langle A^{NC}_\mu \rangle + \frac{\langle \sigma^{CC}_\mu \rangle}{\langle \sigma^{NC}_\mu \rangle} \left\langle A^{CC-misid}_\mu \right\rangle} \tag{8.9}$$

The ratio of neutral to charged current neutrino-nucleon cross-sections has been measured to be 0.31 [Arr94], while the ratio of acceptances of course depends on the scanning strategy.

For the 1995 data scanning strategy we have found the following values:

$$\langle A^{muon}_\mu \rangle = 0.285 \tag{8.10}$$

$$\left\langle A^{CC-misid}_\mu \right\rangle = 0.034 \tag{8.11}$$

$$\langle A^{NC}_\mu \rangle = 0.130 \tag{8.12}$$

Such that the scaling factor found is 3.84.

It is interesting to note that this allows us to directly test the reliability of the simulation for the ratio of the complete reconstruction efficiencies for hadrons and muons. Indeed, if the simulation is precise multiplying the number of found muon-less events by this factor should yield the number of found muon events. For the 1995 data scanned in Nagoya the scaling factor found is 4.17, a discrepancy of 8 %. This also means we overestimate our hadron location efficiency more than we overestimate our muon location efficiency, which should not come as a surprise.

To determine the limit on oscillations we will scale the number of events according to the scanned fraction, relying on the data rather than the simulation. Note that at present a change in this scaling factor by 0.5 only changes the obtained limit by 0.1×10^{-3}.

8.2 Background

Chorus was designed to be a nearly background free experiment, but let us check if that is still correct.

M. Canu [Can97] has investigated the background from production of negatively charged charmed mesons by muon antineutrino interactions. If the primary lepton is not identified such events can perfectly fake the tau signal since they present a similar topology and the daughter particle has the correct charge. His study only applies to the muonic tau decay channel, but the situation should be very similar for the hadronic decays. He found that the expected background rate is 15×10^{-8} observed events per recorded $N^{CC}_{\nu_\mu}$, which is even slightly lower than the estimation made for the Chorus proposal (26×10^{-8}).

Since this value agrees so well with the original estimate, it seems reasonable to accept the proposal values for backgrounds from charmed meson decays as a good upper limit. This implies that the total background for the muonic tau decay channel is below 50×10^{-8} observed events per recorded $N^{CC}_{\nu_\mu}$, which we will see is negligible for the present sample of scanned events and is still below 1 for the full Chorus datasample.

For the hadronic tau decays an additional large source of background stems from elastic scattering of negative pions without observable recoil of the "target" nucleus. If these pions are produced in interactions in which we do not observe any leptons the signal is very similar to a tau decay. Obviously our requirement to have at least 250 MeV transverse momentum at the decay significantly suppresses this background. The real rate is however

not well known leading to extimations between 0 and 3×10^{-6} events per recorded $N_{\nu_\mu}^{CC}$. However, Chorus is in an optimal position to measure this background itself, either by scanning negative pions from events in which a negative muon has been clearly identified or by counting the number of interactions of this type which are observed after a very long flightlength compared to the expected tau flightlength. Should this background be significant, then cuts can be tightened (increase transverse momentum requirement, exploit azimuthal angles, ...) to eliminate it. At the present stage of scanning this background is still below 1 event.

8.3 Systematics on $\frac{\langle \epsilon_{kink} \rangle \langle \sigma_\tau \rangle \langle A_\tau \rangle}{\langle \sigma_\mu \rangle \langle A_\mu \rangle}$

We have evaluated the systematic uncertainty on the ratio of efficiencies and cross sections due to the following possible causes:

- Uncertainty in the momentum measurement in one of the spectrometers. To evaluate the corresponding uncertainty we have varied the measured particle momenta by $\pm 1\sigma$, with σ the momentum resolution of the used spectrometer.
- Effect of the microscope pulse height cut (see section 7.2.2). It is not absolutely obvious here what one standard deviation is. We have varied the pulse height cut by one count each way (see section 7.3.2) to determine the consequences.
- Uncertainty in the impact parameter measurement (section 7.3.3). Here the error on the impact parameter measurement is given by the impact parameter measured for ν_μ^{CC} events (figure 7.8). We found that simply propagating the angular uncertainty on the track measurement in the downstream plates reproduced this error rather well. We have then simply varied the impact parameter value measured by $\pm$ this error to derive the systematic uncertainty on the final result.
- Uncertainty due to the simulation reliability (section 7.2.5). We have conservatively set this uncertainty at 5 %, although we have good reason to believe it cancels out better than this (see section 7.5).
- Uncertainty due to Monte-Carlo Statistics (which we have just required to be small compared to the others).
- Uncertainty on the cross-section ratio $\langle \sigma_\tau^{CC} \rangle \,/\, \langle \sigma_\mu^{CC} \rangle$.

The results are shown in table 8.1.

Following the procedure developed in [Cou92], the upper limit on the number of signal events at 90 % C.L. for a background-free experiment goes up from 2.30 to 2.37 and 2.43 for a 16 % and 22 % systematic uncertainty respectively.

8.4 The Chorus Datasample

Chorus started the exposure of 800 kg of emulsion to the neutrino beam in April 1994. These first 4 stacks were developed at the end of 1995 and replaced by 4 new stacks for exposure in 1996 and 1997. The last events were recorded in November 1997. Figure 8.1 illustrates the steady improvement in accelerator performance during those 4 years, reaching its top performance in 1997 even though a serious accident forced a 2 1/2 month shutdown.

	$\tau^- \to$ "μ^-" + ...	$\tau^- \to$ "0 μ^-" + ...
$\sigma(p)$	$+3.3\%$ -6.1%	$+4.5\%$ -6.3%
Microscope Pulse Height	$+6.4\%$ -10.4%	$+4.5\%$ -9.0%
$\sigma(I.P.)$	$+8.7\%$ -5.7%	$+18.8\%$ -9.9%
MC Reliability	$\pm 5.0\%$	$\pm 5.0\%$
MC Statistics	$\pm 1.0\%$	$\pm 2.3\%$
$\langle\sigma_\tau\rangle \,/\, \langle\sigma_\mu\rangle$	$\pm 7\%$	$\pm 7\%$
Total	$+14.2\%$ -15.9%	$+21.8\%$ -17.3%

Table 8.1: Systematic uncertainties on the ratio of efficiencies and cross-sections due to various cuts for the tau decays where a muon could be identified in the detector (first column) or not (second column).

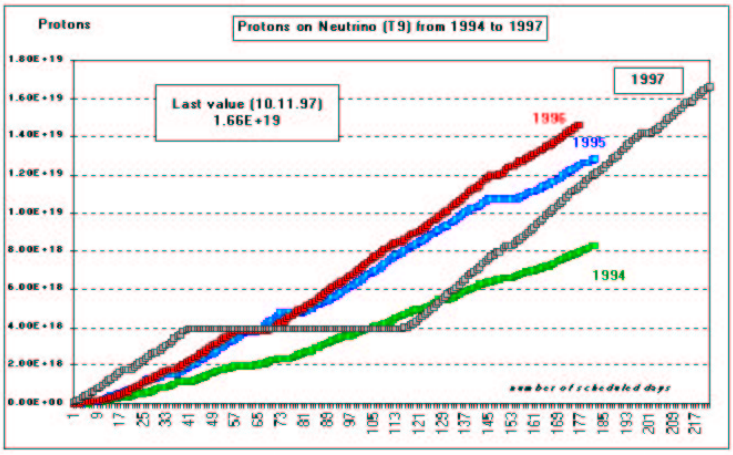

Figure 8.1: Integrated number of protons on the T9 neutrino production target for the 4 years of datataking. The steep slope for 1997 is partially due to an increase of the maximum allowed proton intensity per accelerator extraction. This resulted from improved calculation of the target resistance.

	Run I		Run II		
	1994	1995	1996	1997	Total
P.o.t./10^{19}	0.81	1.20	1.38	1.66	5.05
Chorus Efficiency	0.77	0.88	0.94	0.94	
Deadtime	0.10	0.10	0.13	0.12	
Estimated $N_{\nu_\mu}^{CC}$ Recorded	120 k	200 k	240 k	290 k	850 k
Reconstructed with 1 μ	90 k	148 k	*	*	640 k*
Reconstructed with 0 μ	55 k	77 k	*	*	330 k*

Table 8.2: Accelerator and detector performance during the 4 year emulsion exposure. Run I and II correspond to the two different sets of 800 kg of target emulsion.

Table 8.2 gives the accelerator and detector performance during the four years of emulsion exposure. We see that the Chorus datataking efficiency (defined by the fraction of protons on target for which Chorus was taking data) has increased steadily to reach a plateau at 94 % in 1996. The detector deadtime has been kept at reasonable values by the introduction of an additional trigger plane between 1994 and 1995 and excellent work from the accelerator group on the proton spill shape. The estimated number of $N_{\nu_\mu}^{CC}$ recorded has been derived from the CHARM II observed rate of $N_{\nu_\mu}^{CC}$ per proton on target. Since the 1996 and 1997 data have not been fully processed yet, only estimates (*) can be given for the total number of events with 1 or no muons reconstructed.

8.5 Present Scanning Status

By December 1997 the following fraction of events had been scanned:

- **90 %** of the 1994 muon data (17646 vertices found)
- **64 %** of the 1994 muon-less data (3083 vertices found)
- **43 %** of the 1995 muon data (14586 vertices found)
- **43 %** of the 1995 muon-less data (3466 vertices found)

Unfortunately, only 66 % of the 1995 muon-less data can be used for the oscillation search due to an alignment problem in the hadron spectrometer.

8.6 Values

Table 8.3 gives the values used for the calculation of the limit at large Δm^2. The number of equivalent charged-current events $N_{\nu_\mu - CC}^{equiv}$ has been computed using the method described in section 8.1. For 1994 data we rely on calculations made earlier by various members of the Chorus Collaboration while we use the numbers obtained by the methods described in this work for the 1995 data. The branching ratios are taken from reference [PDG96], where we took for the 1994 muon-less data only the single charged hadron tau decays (corresponding to the analysis performed by O. Sato), while for the 1995 muon-less data we took all the single-prong non-muonic decays. The reason for this is that our simulation included all non-muonic decays, or 82.65 %. We have then conservatively excluded **all** multiprong decays since we cannot confirm that the negative charge of the parent would be identified.

	1994 with muon	1995 with muon	1994 muon-less	1995 muon-less
Vertex Plate Identified	17646 events	14586 events	3083 events	2288 events
$N^{equiv}_{\nu_\mu - CC}$	17646 events	14586 events	12548 events	9627 events
$B.R.$	0.1735	0.1735	0.4978	0.6774
$\langle \sigma_\tau / \sigma_\mu \rangle$	0.53	0.53	0.53	0.53
$\langle A_\tau / A_\mu \rangle$	1.05	1.076	0.43	0.746
$\langle \epsilon_{kink} \rangle$	0.54	0.282	0.23	0.085
"N^{max}_τ"	920 events	407 events	327 events	219 events

Table 8.3: Values needed for the calculation of the limit at large Δm^2. The values for 1994 data have been taken from previous studies while for 1995 data they come from this work. More details are given in the text.

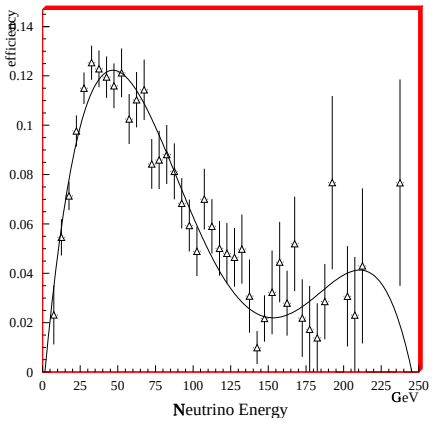

Figure 8.2: Tau detection efficiency as a function of neutrino energy. The fit function is given in the text.

The significantly lower value of $\langle A_\tau / A_\mu \rangle$ for the 1994 muon-less sample (as compared to the 1995 sample) stems from the inclusion of the requirement that the scan-back track be a tau daughter. This requirement is accounted for in $\langle \epsilon_{kink} \rangle$ in the 1995 muon-less sample. This is in our opinion the right way to proceed since even if the scan-back track is not a tau daughter the event can still be found. In the future kink search will also proceed through "follow-down": when the vertex is found all tracks at the vertex are followed downstream for 5 plates to search for a decay signature. With this method, obviously, including the requirement that the scan-back track be a tau daughter in the ratio $\langle A_\tau / A_\mu \rangle$ does not make sense.

N^{max}_τ is the product of all these numbers and represents the number of tau events we would observe for maximal mixing. It indicates the relative contribution of each of the datasamples.

We still have to compute the upper limit on signal events, which is affected by the systematic uncertainties. Weighing the results found in section 8.3 with the equivalent number of charged current events given in table 8.3 we obtain 2.387.

The energy dependence of the tau detection efficiency $\langle A_\tau \rangle \langle \epsilon_{kink} \rangle$ is shown in figure 8.2. The energy dependences of the different channels are weighted according to the corresponding N^{max}_τ values. The fitted function is given by

$$\epsilon_\tau(E_\nu) = -0.1032\ 10^{-1} + 0.6794\ 10^{-2}\ E_\nu - 0.1110\ 10^{-3}\ E_\nu^2 \\ +0.6169\ 10^{-6}\ E_\nu^3 - 0.1127\ 10^{-8}\ E_\nu^4 \quad (8.13)$$

with a fit $\chi^2 = 41.86$ for 37 degrees of freedom.

Note that the "bump" at the end of the spectrum does not seem to be physical but rather due to the low statistics in that region. As a test we have separated the fit in two intervals, one up to 150 GeV and one beyond, imposing a single value at 150 GeV and no bump. The resulting exclusion curve cannot be discerned by eye from the one produced using the simple polynomial fit.

8.7 New Limit On $\nu_\mu \to \nu_\tau$ Oscillations

Since no candidates were found, we can combine all the values to obtain a new limit at 90 % C.L. and for large Δm^2:

$$sin^2 2\theta_{\mu\tau} < 2\ \ \frac{2.387}{1873} = 2.5 \times 10^{-3} \quad (8.14)$$

The variation of the limit as a function of Δm^2 is shown in figure 8.3. It results in a limit $\Delta m^2 > 1.44\ eV^2$ for maximal mixing ($sin^2 2\theta_{\mu\tau} = 1$).

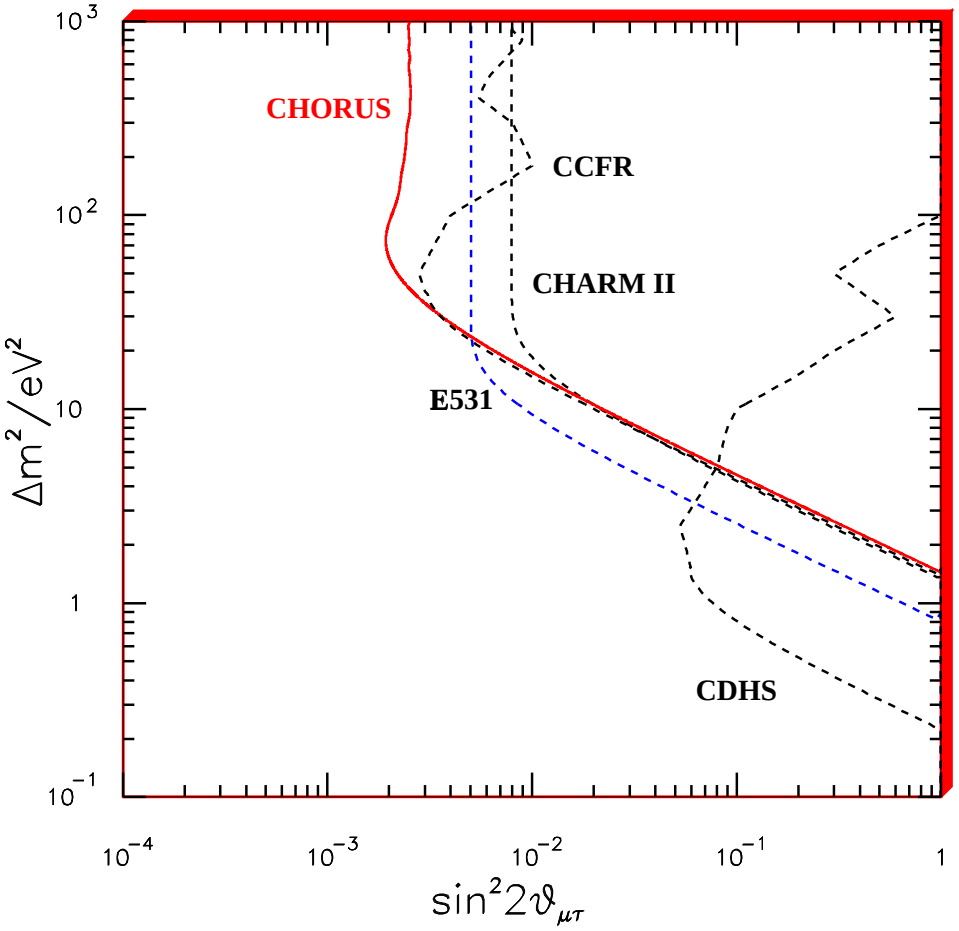

Figure 8.3: New $\nu_\mu \rightarrow \nu_\tau$ oscillation exclusion plot.

Chapter 9

Conclusions

In the first part of this work we have demonstrated that a lot of the available experimental data suggests neutrinos could have some properties different from those in the Standard Model. Furthermore, most theoretical models indeed prefer massive neutrinos.

One beautiful potential property of massive neutrinos is that they could oscillate from one flavor to another. The only conditions for this are that the mass eigenstates do not coincide with the weak eigenstates and that the masses are not degenerate.

Chorus is one of the experiments looking for confirmation of neutrino oscillation by detecting the appearance of tau neutrinos in a dominantly muon neutrino beam. To be able to explicitely reconstruct the tau production and decay topology in potential tau neutrino-induced charged-current interactions, Chorus chose a nuclear emulsion target. A scintillating fiber tracker is used to predict the event position in the emulsion with good accuracy (and thus minimize emulsion scanning time), and two spectrometers and a calorimeter allow a good measurement of the event kinematics (reducing the background to less than one event).

We have extensively described and evaluated those parts of the reconstruction and simulation software to which we have made significant contributions: the Target Tracker alignment and event reconstruction procedures, the muon tagging algorithms and the emulsion scanning simulation.

The latter naturally leads to the evaluation of the scanning efficiencies, which combined with the global reconstruction efficiencies result in the determination of the actual Chorus tau detection efficiency. Applied to the present sample of fully reconstructed events (including scanning) we have obtained a new limit on muon- to tau neutrino oscillations of $sin^2 2\theta_{\mu\tau} < 2.5 \times 10^{-3}$ at 90 % C.L. and for large Δm^2.

For the future the members of the Chorus collaboration are working hard on improving the reconstruction and scanning efficiencies, with the emphasis on the further development of automatic emulsion scanning. The final aim is to reach a sensitivity such that when all the data will have been analyzed Chorus will either obtain a limit $sin^2 2\theta_{\mu\tau} < 2 \times 10^{-4}$ at 90 % C.L. and for large Δm^2 or find evidence for tau neutrino appearance in the beam.

Bibliography

[Abd94] SAGE Collaboration, J.N. Abdurashitov et al.,*Phys. Lett.* B **328**, 234 (1994).

[Abd96a] SAGE Collaboration, J.N. Abdurashitov et al.,*Phys. Rev. Lett.* **77**, 4708 (1996).

[Abd96b] SAGE Collaboration, J.N. Abdurashitov et al., Proc. of the *7th International Workshop on Neutrino Telescopes*, Venice, Feb 27 - Mar 1 1996.

[Abe97] SLD Collaboration, K. Abe et al.,*Phys. Rev. Lett.* **79**, 804 (1997).

[Ake95] OPAL Collaboration, R. Akers et al.,*Z. Phys.* C **65**, 183 (1995).

[Alb92] ARGUS Collaboration, H. Albrecht et al.,*Z. Phys.* C **56**, 339 (1992).

[All97] SOUDAN 2 Collaboration, W.W.M. Allison et al.,*Phys. Lett.* B **391**, 491 (1997).

[Alt94] G. Altarelli, Proc. of the *6th International Symposium on Neutrino Telescopes*, Venice, Italy, 22-24 Feb 1994 and references therein.

[Amb96] SPY Collaboration, G. Ambrosini et al, CERN-SPSLC/**96-01** (1996).

[Ann97] P. Annis et al, submitted to *Nucl. Instrum. Methods* , (1997).

[Ans95] GALLEX Collaboration, P. Anselmann et al.,*Phys. Lett.* B **342**, 440 (1995).

[Aok90] S. Aoki et al., *Nucl. Instrum. Methods* B **51**, 446 (1990).

[Apo97] CHOOZ Collaboration, M. Apollonio et al., hep-ex/9711002 (1997).

[Arm95] Karmen Collaboration, B. Armbruster et al., *Phys. Lett.* B **348**, 19 (1995).

[Arm97] N. Armenise et al., CERN-SPSC/97-21.

[Arr94] CCFR Collaboration, C.G. Arroyo et al.,*Phys. Rev. Lett.* **72**, 3452 (1994).

[Ass96] K. Assamagan et al., *Phys. Rev.* D **53**, 6067 (1996).

[Ast90] NOMAD Collaboration, P. Astier et al., CERN-SPSC/91-21 (1990); CERN-SPSLC/91-48 (1991); CERN-SPSLC/91-53 (1991).

[Ath96] LSND Collaboration, C. Athanassopoulos et al.,*Phys. Rev.* C **54**, 2685 (1996).

[Ath97] LSND Collaboration, C. Athanassopoulos et al.,*Nucl. Instrum. Methods* A **388**, 149 (1997).

[Ath98] LSND Collaboration, C. Athanassopoulos et al.,submitted to *Phys. Rev.* C , (1998).

[Aya97] TOSCA Collaboration, A. Ayan et al., CERN-SPSC/97-5 (1997).

[Bac78] DELCO Collaboration, W. Bacino et al.,*Phys. Rev. Lett.* **41**, 13 (1978).

[Bac79] DELCO Collaboration, . Bacino et al.,*Phys. Rev. Lett.* **42**, 749 (1979).

[Bah89] J.N. Bahcall, *Neutrino Astrophysics*, Cambridge University Press, Cambridge (1989).

[Bah92] J.N. Bahcall and M. Pinsonneault, *Rev. Mod. Phys.* **64**, 885 (1992).

[Bah95] J.N. Bahcall and M. Pinsonneault, *Rev. Mod. Phys.* **67**, 781 (1995).

[Bah97] Unsolved Problems in Astrophysics, proceedings of the conference Some Unsolved Problems in Astrophysics, Institute for Advanced Study, Princeton, April 27-29, 1995, eds. John N. Bahcall and Jeremiah P. Ostriker (Princeton: Princeton University Press, 1997), p. 195.

[Bar89] G. Barbiellini et al., in "Z Physics at Lep 1", CERN Report CERN 89-08 (1989), eds G. Altarelli, R. Kleiss and C. Verzegnassi, Vol. 1, p. 129.

[Bar97] ALEPH Collaboration, R. Barate et al.,CERN-PPE/97-138 (1997).

[Bec92] IMB Collaboration, R. Becker-Szendy et al.,*Phys. Rev.* D **46**, 3720 (1992).

[Bel95] A.I. Belesev et al.,*Phys. Lett.* B **350**, 263 (1995).

[Ber89] FREJUS Collaboration, C. Berger et al.,*Phys. Lett.* B **227**, 489 (1989).

[Ber95] F. Bergsma et al.,*Nucl. Instrum. Methods* A **357**, 243 (1995).

[Bru97a] J. Brunner, private communication.

[Bru97b] J. Brunner, Chorus Internal Note 97017 (1997).

[Bus95a] ALEPH Collaboration, D. Buskulic et al.,*Phys. Lett.* B **346**, 379 (1995);
ARGUS Collaboration, H. Albrecht et al.,*Phys. Lett.* B **349**, 576 (1995);
ARGUS Collaboration, H. Albrecht et al.,*Phys. Lett.* B **341**, 441 (1995);
L3 Collaboration, M. Acciarri et al.,*Phys. Lett.* B **377**, 313 (1996);
SLD Collaboration, K. Abe et al.,*Phys. Rev. Lett.* **78**, 4691 (1997).

[Bus95b] ALEPH Collaboration, D. Buskulic et al.,*Phys. Lett.* B **349**, 585 (1995).

[Cab63] N. Cabibbo, *Phys. Rev. Lett.* **10**, 531 (1963).

[Cab78] N. Cabibbo, *Phys. Lett.* B **72**, 333 (1978).

[Can97] M. Canu, Chorus Internal Note 97025 (1997).

[Cav84] BUGEY 1 Collaboration, J.F. Cavaignac et al.,*Phys. Lett.* B **148**, 387 (1984).

[Che84] T.-P. Cheng and L.-F. Li, *Gauge Theory of Elementary Particle Physics*, Clarendon Press, Oxford (1984).

[Chu97] BOONE Collaboration, E. Church et al, LA-UR-97-2120 (1997).

[Cle96] B. T. Cleveland et al., Proc. of the *7th International Workshop on Neutrino Telescopes*, Venice, Feb 27 - Mar 1 1996.

[Coc97] A. Cocco, "ced", email to Chorus Collaboration, March 4th, 1997.

[Cos95] COSMOS Collaboration, 1995 Update Report on Fermilab E803/COSMOS.

[Cou92] R.D. Cousins and V.L. Highland, *Nucl. Instrum. Methods* A **320**, 331 (1992).

[Cow56] C. L. Cowan, Jr., F. Reines, F. B. Harrison, H. W. Kruse, A. D. McGuire, *Science* **124**, 103 (1956).

[Cu96] A. Cummings and W.C. Haxton, *Phys. Rev. Lett.* **77**, 4286 (1996).

[Dan62] G. Danby, J-M. Gaillard, K. Goulianos, L. M. Lederman, N. Mistry, M. Schwartz and J. Steinberger, *Phys. Rev. Lett.* **9**, 36 (1962).

[Dar94] A. Dar and G. Shaviv, *astro-ph/9401043*, unpublished (1994).

[Dar96] A. Dar and G. Shaviv,*Astrophys.J.* **468**, 933 (1996).

[Dar97] A. Dar, *Lectures given at the 1997 ITEP Winter School on Particle Physics*, St. Petersburg, 24 Feb-2 Mar 1997.

[Dau95] FREJUS Collaboration, K. Daum et al., *Z. Phys.* C **66**, 417 (1995).

[Dec95] BUGEY-3 Collaboration, Y. Declais et al.,*Nucl. Phys.* B **434**, 503 (1995).

[deJ93] CHORUS Collaboration, M. de Jong et al.,CERN-PPE/93-131 (1993).

[DiC96] E. Di Capua et al.,*Nucl. Instrum. Methods* A **378**, 221 (1996).

[Dil95] S. Di Liberto, Chorus Collaboration Meeting, May 1995.

[Eit97] Karmen Collaboration, K. Eitel et al., Proc. of the *32nd Rencontres de Moriond, Electroweak Interactions and Unified Theories*, Les Arcs, March 15-22 1997.

[Ell96] J. Ellis, Proc. of the *17th International Conference on Neutrino Physics and Astrophysics (Neutrino 96)*, Helsinki, Finland, 13-20 June 1996; J.Ellis, *Lectures presented at the Les Houches Summer School on "Cosmology and Large Scale Structure"*, Les Houches, France, 1993.

[Esk97] CHORUS Collaboration, E. Eskut et al.,submitted to *Nucl. Instrum. Methods* , (1997).

[Fei58] G. Feinberg, *Phys. Rev.* **110**, 1482 (1958).

[Fet90] W. Fetscher, *Phys. Rev.* D **42**, 1544 (1990).

[Fuk94] KAMIOKANDE Collaboration, Y. Fukuda et al., *Phys. Lett.* B **335**, 237 (1994).

[Fuk96a] KAMIOKANDE Collaboration, Y. Fukuda et al., *Phys. Rev. Lett.* **77**, 1683 (1996).

[Fuk96b] KAMIOKANDE Collaboration, Y. Fukuda et al., *Phys. Lett.* B **388**, 397 (1996).

[Gai90] T.K. Gaisser, *Cosmic Rays and Particle Physics*, Cambridge University Press, Cambridge (1990).

[Gai96a] T.K. Gaisser et al.,*Phys. Rev.* D **54**, 5578 (1996).

[Gai96b] T.K. Gaisser, Proc. of the *17th International Conference on Neutrino Physics and Astrophysics (Neutrino 96)*, Helsinki, Finland, 13-20 June 1996;

[Gel79] M. Gell-Mann, P. Ramond and R. Slansky, in Supergravity, ed. by D. Freedman et al., North Holland (1979).

[Gel95] G. Gelmini and E. Roulet, *Rept. Prog. Phys.* **58**, 1207 (1995).

[Gia96] BOREXINO Collaboration, M. G. Giammarchi et al., Proc. of the *7th International Workshop on Neutrino Telescopes*, Venice, Feb 27 - Mar 1 1996.

[Giu91] C. Giunti, C.W. Kim and U. W. Lee,*Phys. Rev.* D **44**, 3635 (1991).

[Giu97] C. Giunti, C.W. Kim and M. Monteno, hep-ph/9709439 (1997);
M. Narayan and G. Rajasekaran, *Phys. Rev.* D **56**, 437 (1997);
O. Yasuda, hep-ph/9706546 (1997).

[Gra96] PALO VERDE Collaboration, G. Gratta et al., Proc. of the *17th International Conference on Neutrino Physics and Astrophysics (Neutrino 96)*, Helsinki, Finland, 13-20 June 1996.

[Gun97] M. Günther et al, *Phys. Rev.* D **55**, 54 (1997).

[Hal84] F. Halzen and A.D. Martin, *Quarks and Leptons: An Introductory Course in Modern Particle Physics*, Wiley, New York (1984).

[Ham96] GALLEX Collaboration, W. Hampel et al.,*Phys. Lett.* B **388**, 384 (1996).

[Hat93] N. Hata and P. Langacker, *Phys. Rev.* D **48**, 2937 (1993).

[Hat94] N. Hata and P. Langacker, *Phys. Rev.* D **50**, 632 (1994).

[Hat95] N. Hata and P. Langacker, *Phys. Rev.* D **52**, 420 (1995).

[Hat97] N. Hata and P. Langacker, *Phys. Rev.* D **56**, 6107 (1997).

[Hey96] G. Heyboer, Chorus Internal Note (1996).

[Him96] SNO Collaboration, A. Hime et al., Proc. of the *7th International Workshop on Neutrino Telescopes*, Venice, Feb 27 - Mar 1 1996.

[Kay81] B. Kayser, *Phys. Rev.* D **24**, 110 (1981);
J. Rich, *Phys. Rev.* D **48**, 4318 (1991).

[Kay89] B. Kayser with F. Gibrat-Debu and F. Perrier, *The Physics of Massive Neutrinos*, World Scientific, Singapore (1989) and references therein.

[Kob73] M. Kobayashi and T. Maskawa, *Progr. Theor. Phys.* **49**, 652 (1973).

[Kuo87] T.K. Kuo and J. Pantaleone, *Phys. Rev.* D **35**, 3433 (198 7).

[LEP96] The LEP Collaborations ALEPH, DELPHI, L3, Opal, The LEP Electroweak Working Group and the SLD Heavy Flavour Group, CERN-PPE/**96-183**, 1996.

[Lip95] P. Lipari et al.,*Phys. Rev. Lett.* **74**, 4384 (1995).

[Loh95] W. Lohmann and J. Raab, DESY **95-188**, 1995.

[Lok55] S. Lokanathan and J. Steinberger, *Phys. Rev.* **98**, 240 (1955).

[Lun94] B. Lundberg et al., Fermilab Proposal P872 (1994).

[Maj37] E. Majorana, *Nuovo Cimento* **14**, 171 (1937).

[McF97] CCFR Collaboration, K. McFarland et al., submitted to *Phys. Rev. Lett.* , (1997).

[Mic50] L. Michel describes leptonic muon decays by writing the most general, local, derivative-free and lepton-number-conserving four fermion point interaction Hamiltonian. After some algebra a number of parameters are obtained whose values are determined by the structure of the interaction vertex. L. Michel, *Proc. Phys. Soc. London* **A63**, 514 (1950).

[Mik85] S.P. Mikheev and A. Yu. Smirnov, *Sov. J. Nucl. Phys.* **42**, 913 (1985).

[Min92] MINUIT - Function Minimization and Error Analysis,(CERN Program Library Long Writeup D506), Application Software Group, Computing and Networks Division, CERN, Geneva, Switzerland.

[Mur85] K. Mursula and F. Scheck, *Nucl. Phys.* B **254**, 189 (1985).

[Nak91] T. Nakano et al, in *Proc. of IEEE 1991 Nuclear Science Symp.*, Santa Fe (1991).

[Nak93] T. Nakano et al, in *Proc. of Scintillating Fiber Symposium 1993*, University of Notre Dame (1993).

[Nak97] M. Nakahata, Proc. of the *International Europhysics Conference on High Energy Physics*, Jerusalem, August 19-26 1997.

[Okun82] L. B. Okun, *Leptons and Quarks*, North-Holland Physics Publishing, Amsterdam (1982).

[Ott95] E. W. Otten, *Nucl. Phys.* B **38**, 26 (1995).

[PDG96] Particle Data Group, R.M. Barnett et al., *Phys. Rev.* D **54**, 1 (1996).

[Perl75] M. L. Perl et al.,*Phys. Rev. Lett.* **35**, 1489 (1975);
M. L. Perl et al.,*Phys. Lett.* B **63**, 466 (1976).

[Pir96] G. Piredda and P. Righini, Chorus Internal Note (1996).

[Pol94] N. Polonsky, *Phd. Thesis*, University of Pennsylvania (UPR-0641-T), 1994.

[Pon57] B. Pontecorvo, *J.E.T.P.* **33**, 429 (1957);
B. Pontecorvo, *J.E.T.P.* **34**, 172 (1958).

[Raby94] S. Raby, in *Trieste HEP Cosmology 1994*, 126 (1994).

[Rei53] F. Reines and C. L. Cowan, Jr., *Phys. Rev.* **92**, 830 (1953).

[Ric97] S. Ricciardi, Chorus Internal Note 97001 (1997).

[Ross84] G. G. Ross, *Grand Unified Theories*, pp. 240 and following, Benjamin-Cummings, Menlo Park (1984).

[Rya94] O.G. Ryazhskaya, *J.E.T.P. Lett.* **60**, 617 (1994).

[Sal95] D. Saltzberg, *Phys. Lett.* B **355**, 499 (1995).

[Sel97] CCFR Collaboration, W.G. Seligman et al,submitted to *Phys. Rev. Lett.* , (1997).

[Sta94] A. Stahl, *Phys. Lett.* B **324**, 121 (1994).

[Ste93] CHOOZ Collaboration, R. I. Steinberg et al., Proc. of the *4th International Workshop on Neutrino Telescopes*, Venice, Mar 2-5 1993.

[Tak97] SUPER-KAMIOKANDE Collaboration, Y. Takeuchi et al., Proc. of the *32nd Rencontres de Moriond, Electroweak Interactions and Unified Theories*, Les Arcs, March 15-22 1997.

[Tal87] BUGEY 1 Collaboration, M. Talby et al. in *Proc. XXIInd Rencontre de Moriond, The Standard Model, the Supernova 1987A*, page 393, edited by J. Tran Tan Vanh, édition Frontières (1988).

[Tot97] Y. Totsuka, Proc. of the *XVIII International Symposium on Lepton-Photon Interactions*, Hamburg, July 28 - August 1 1997.

[Ush86] E531 Collaboration, N. Ushida et al., *Phys. Rev. Lett.* **57**, 2897 (1986).

[Van97a] B. Van de Vyver, *Nucl. Instrum. Methods* A **385**, 91 (1997);
M.C. Gonzalez-Garcia and J.J. Gomez-Cadenas, *Phys. Rev.* D5512971997.

[Van97b] B. Van de Vyver, private communication.

[Vil94] CHARM II Collaboration, P.Vilain et al.,*Phys. Lett.* B **335**, 246 (1994).

[Win91] K. Winter, *Neutrino Physics*, Cambridge University Press, Cambridge (1991).

[Wol78] L. Wolfenstein, *Phys. Rev.* D **17**, 2369 (1978).

[Yan80] T. Yanagida, *Prog. Theor. Phys.* **64**, 1103 (1980).

[Zuc94] P. Zucchelli, Ph.d. Thesis, Università Degli Studi Di Ferrara, (1994).

List of Figures